THEORETICAL MODELS FOR MICROWAVE REMOTE SENSING OF FORESTS AND VEGETATION

by

CHIH-CHIEN HSU

B.S., National Chiao Tung University, Taiwan
June 1987

M.S., MASSACHUSETTS INSTITUTE OF TECHNOLOGY
May 1992

Submitted to the Department of Electrical Engineering and Computer Science
in Partial Fulfillment of the Requirements for the Degree of

DOCTOR OF PHILOSOPHY

at the

MASSACHUSETTS INSTITUTE OF TECHNOLOGY

May 1996

Signature of Author _____
Department of Electrical Engineering and Computer Science
May, 1996

Certified by _____
Jin A. Kong
Thesis Supervisor

Accepted by _____
Frederic R. Morgenthaler
Chairman, Department Committee on Graduate Students

THEORETICAL MODELS FOR MICROWAVE REMOTE SENSING OF FORESTS AND VEGETATION

by

CHIH-CHIEN HSU

Submitted to the Department of Electrical Engineering and Computer Science
in May, 1996 in Partial Fulfillment of the Requirements for the
Degree of Doctor of Philosophy

ABSTRACT

This thesis presents the development and validation of theoretical models for electromagnetic wave propagation, scattering and emission from the plants and forest and their applications to the microwave remote sending of vegetation covered earth terrain.

A radiative transfer model with clustered vegetation structure is developed and used to simulate the polarimetric radar backscatter signatures of pine forest. The specific clustered structure of forest is incorporated in the calculation of the phase and extinction matrices. The theoretical model is applied to interpret the measured UHF, L-, C-, and X-bands radar data at the Landes pine forest in Southern France during the AIRSAR and SIR-C/XSAR missions. The experiments were conducted by Centre d'Etude Spatiale BIOsphere (CESBIO), the National Aeronautics and Space Administration (NASA) and Jet Propulsion Laboratory (JPL). The collected ground truth is used as the input parameters to the developed model. The effect of the tree clustering structure and the coherent wave interactions due to the fine structure of the leaves are shown to have impacts on the polarimetric signatures of forest. It is found that the cross-polarized return at lower frequencies and the correlation coefficient of HH and VV polarizations are sensitive to the total forest biomass.

Millimeter wave scattering from an isolated tree is studied by using a tree model consisted of a crown as the random medium with random distribution of leaves and twigs, and trunk and large branches as deterministic scattering objects. The trunk is modeled as a circular cylinder with random rough surface where Kirchhoff's approximation is used to obtain the radar return from the surface of the trunk. Transmission loss factors, which is caused by absorption and scattering, are included when computing the contribution from interior branches and trunks. The scattering from crown is calculated with the radiative transfer theory. The theoretical predictions are compared with the measured range profile of coniferous and deciduous trees. The measurements were made by Army Research Laboratory (ARL) using a 94 GHz

FMCW radar. A good agreement between the model simulation and data is demonstrated. The sensitivity of tree size, leaf angle distribution and density distribution to the range profile of tree is investigated.

A theoretical model is developed to calculate the mean attenuation, the amplitude and the phase fluctuations of electromagnetic waves propagating through foliage. The attenuation of the average received field is obtained from the sum of the absorption loss and the scattering loss. The amplitude fluctuation of electromagnetic wave is calculated from the bistatic scattering coefficients using the radiative transfer theory. The phase fluctuation is obtained from the amplitude fluctuation assuming the phase of the fluctuation field is uniformly distributed from $-\pi$ to π. The theoretical results are compared with experimental data at UHF, L-, and C-bands which were collected by MIT Lincoln Laboratory during the 1990 Foliage Penetration Experiment. In the experiment, transmitters were placed inside the forest and an airborne receiver was used to measure the one-way propagation. This theoretical model is used to illustrate the polarization and angular dependencies of attenuation and phase fluctuations. It is found that the attenuation increases with the frequency and the depression angle. The vertical polarized field at UHF band is attenuated more than that of horizontal polarization due to the large attenuation by the trunks. The phase fluctuation is found to increase with the attenuation for all frequencies.

A passive remote sensing model based on radiative transfer theory with both continuous random medium model and discrete scatterers model is developed to study the polarimetric thermal emission from the vegetation canopy. The polarimetric brightness temperature is obtained either directly from the solution of radiative transfer equation with source term included or calculated with Kirchhoff's law from the bistatic scattering coefficients. The theoretical model is used to interpret the emissions measured by Istituto di Ricerca sulle Onde Elettromagnetiche (IROE) of Italy over an alfalfa field at different growth stages at 10 GHz. Theoretical studies on the polarimetric emission from non-azimuthally symmetrical media with tilted scatterers has been investigated. It is found that the third Stokes parameter is sensitive to the azimuthal asymmetry of the medium.

Thesis Supervisor: Jin Au Kong
Title: Professor of Electrical Engineering

Acknowledgments

First I would like to express my sincere thank to Professor Jin Au Kong, my graduate advisor and thesis supervisor, for his guidance and support for these years. His enthusiastic encouragement and instruction is deeply appreciated.

I am also very thankful to the members of my thesis committee, Professor David Staelin, Dr. Kung-Hau Ding, Dr. Thuy Le Toan for their many suggestions to improve this thesis.

To Dr. Eric Yang and Dr. Robert Shin for their supervision of the research projects and many helpful discussions about the direction of the research.

Many Thanks to Dr. Thuy Le Toan, Dr. Andre Beaudoin, and Dr. Jean-Claude Souyris, for their forest experiments and many discussions and suggestions about the development of theoretical model. Thanks to Dr. Serpil Ayasli, Dr. Jack Fleischman and Dr. Michael Toups for their FOPEN experiment. To Dr. Simonetta Paloscia and Dr. Paolo Pampaloni for their alfalfa experiment. To Mr. Chuck Kohler and his colleagues at Army Research Laboratory for their MMW scattering experiments.

Many current and former members of our research group helped me in many ways to survive at M.I.T. Our secretary Kit-Wah Lai always provided timely suggestion and help. To Lifang Wang for her friendship in many years and with Dr. Joel Johnson for our brush with the passive experiment. To Dr. Son Nghiem for the opportunity to do experiment at $-35°F$. To Dr. Check Lee for his support for me as a Lincoln RA and many candid discussions. To Dr. Hsiu Chi Han and Dr. Simon Yueh for their help in my earlier years here. I would like also to acknowledge

the people who provide me with friendship, they are Jerry Akerson, Dr. Robert Atkins, Dr. William Au, Dr. Lars Bomholt, Pierre Coutu, Hong Tat Ewe, Fabio del Frate, Dr. Qizheng Gu, Tza-Jing Gung, Yoshihisa Hara, Gregory Huang, Dr. Minoru Ishikawa, Dr. Cheung-Wei Lam, Dr. Laurence Lee, Dr. Kevin Li, Harold Lim, Angel Martinez, Dr. John Oates, Francesca Scire Scappuzzo, Dr. Jean-Claude Souyris, Dr. Liguo Sun, Dr. Ali Tassoudji, Nayon Tomsio, Dr. Murat Veysoglu, Dr. Jake Xia, Kent Yan, Dr. Masanori Yamaguchi, Chen-Pang Yeang, Dr. Yi Yuan, Yan Zhang.

I would like to thank my uncle Tsan H. Lin and his family for their hospitality. Special thanks to my uncle for his encouragement and many helpful discussions.

To my parents and my younger sister and brother for their love and care. Their faith in me make everything possible. I will always remember how my elder relatives back in Taiwan are proud of me although some of them can not wait to this moment.

Last but not least, I wish to thank my wife, Mei-ling, for her love and unwavering support.

To my parents, I dedicate this work.

To my parents

Table of Contents

List of Figures

Figures in Chapter 2

Figures in Chapter 3

Figures in Chapter 4

Figures in Chapter 5

List of Tables

Tables in Chapter 2

Tables in Chapter 3

Tables in Chapter 4

Tables in Chapter 5

Chapter 1.

Introduction

1.1 BACKGROUND

The characteristics of earth terrain and their electromagnetic response are of great interest to the radar community as well as remote sensing scientists. For researchers interested in the radar signature of targets, the understanding of radar scattering from earth terrain as "clutter" would aid to better target detection and the false alarm problems associated with it. For the remote sensing community, it is essential to relate and invert the terrain parameters such as vegetation biomass and soil moisture to the scattering and/or emission properties.

Remote sensing usually can be divided into two areas: passive and active. In passive remote sensing, a radiometer is used to measure the thermal emission from media which radiate electromagnetic energy at a finite physical temperature. The brightness temperature, which is the temperature the black body has to reach in order to radiate the same amount of energy, is used to characterize the thermal emission from the terrain. For a medium at a constant physical temperature and without the background sky radiation, the brightness temperature is the emissivity multiplied with the physical temperature. In active remote sensing, a radar system

consisting of transmitter and receiver is utilized. A bistatic radar has transmitter and receiver located at different locations, whereas a monostatic radar has them placed at the same location. The transmitter sends out a signal to the target and the scattered signal in the specific direction is measured by the receiver. The target is characterized by the radar cross-section which has the dimension of area and is dependent on the frequency, polarization and the angles of illumination and observation of the radar. For the case of distributed targets, such as earth terrain, the scattering coefficient used is the radar cross section normalized to the illuminated area on the ground.

With its abilities to penetrate clouds and rain to some extent and to provide day and night coverages, remote sensing instruments at the microwave frequencies have been applied in the area of radar monitoring. The advance of satellite and radar technology has made the satellite or air-borne remote sensing the most efficient way to monitor the global earth ecosystem and resources. Parameters of interest from the large scale terrain can be obtained to monitor the environmental changes caused by seasonal variations or natural and man-kind activities.

Compared with optical and infrared sensors, the use of space-borne active microwave sensor for the continuous monitoring of earth is relatively little until recent years. Starting from Seasat in 1978 with the aim to image the ocean [Giberson, 1991], spaceborne imaging radar missions such as SIR-A and SIR-B with radar operated at L-band (1.25GHz) has been successfully launched [Jordan 1980, Cimino, 1986]. Even just equipped with single polarization (horizontal polarization) antenna , these instruments are proven to be capable of multiple tasks such as land cover classification, ocean monitoring, soil moisture monitoring and sub-surface detection [Elachi, et al., 1986]. With the success of these missions, microwave satellites such as European Remote Sensing Satellite (ERS-1, ERS-2), Japanese Earth Resource Satellite-1 (JERS-1)

[Nemoto et al., 1991] have been designed and launched. Recently, Spaceborne Imaging Radar-C and X-band Synthetic Aperture Radar (SIR-C/XSAR) has completed two successful mission in 1994 [Stofan, et al., 1995]. The SIR-C/XSAR includes three frequencies (L-, C-, and X-band) with fully polarimetric data available at L- and C-band. At X-band, VV polarized return is measured. The Synthetic Aperture Radar (SAR) systems together with passive radiometers at microwave frequency are all included in the broad plan of the Earth Observing System (EOS) proposed by National Aeronautics and Space Administration [NASA, 1986].

With the increasing polarimetric capability of radar systems and their potential applications, the research on the polarimetric microwave remote sensing has generated lots of interests in recent years. The additional information provided by the polarimetric measurements has been shown to be useful in the identification and classification of terrain types. Also, from the modeling point of view, these additional informations can reduce the ambiguity in the input parameters when trying to interpret the experimental results and could be helpful in developing more realistic models. It has been shown in both active [Borgeaud et al., 1987, 1989; Evans et al., 1988; Kong, 1990; Lim et al., 1989; van Zyl et al., 1987; Zebker et al., 1987] and passive [Tsang, 1990; Veysoglu et al., 1990] studies that the polarimetry can provide significant information in the characterization and identification of terrain types.

Because of the complicated nature of the earth medium and the large scale of efforts needed to conduct the experiment, it is necessary to have accurate physically based theoretical models to assist the preparation of the experiment, to draw physical conclusion from the experiment, and to invert the interested parameters from remote sensing data with the validated models. Abundant researches have been carried out with the development of theoretical modeling development [Tsang et al., 1985] and

controlled experiments [Ulaby et al., 1981]. Progress has been made through the better understanding of the scattering processes and with the better characterization of the earth terrain media in the electromagnetic point of view.

In the study of the electromagnetic interaction with earth terrain, the scattering effect caused by inhomogeneities of medium plays an important role in the overall scattering response. Two theories which have been used extensively to study the wave propagation and scattering are the wave theory and the radiative transfer theory. The wave theory starts from Maxwell's equations and with the use of dyadic Green's function for the layered medium, incorporates the scattering and absorption characteristics of medium. In principle, all the scattering mechanisms, such as multiple scattering, diffraction, and reflection, are all included. However, the equations are generally complicated and approximations have to be made before numerical solutions can be obtained. On the other hand, the radiative transfer theory begins with the radiative transfer equations which describe the propagation of specific intensity within the medium under consideration. The development of this theory is quite heuristic and lack of rigor. However, this approach has the advantage that it is simple and rather easy to include multiple scattering effects to some extent. Also, it has been shown that the radiative transfer theory can also be derived from the wave theory by following the Bethe-Salpeter equation under the ladder approximation [Tsang and Kong, 1979].

As to the scattering effect, the two major approaches used are the continuous random medium model and the discrete scatterer model. For the continuous random medium approach [Fisher, 1977; Fung and Fung, 1977; Fung and Ulaby, 1978; Stogryn, 1974; Tsang and Kong, 1979; Zuniga and Kong, 1980], the medium under consideration is described by a correlation function with variances and correlation

lengths to represent the permittivity fluctuations. The effective permittivity is evaluated to account for the attenuation and phase delay of wave propagation inside the medium. Discrete scatterer model, on the other hand, describes the inhomogeneous medium as a collection of discrete scatterers of different sizes and shapes. The Foldy's approximation has been used for sparse medium [Foldy, 1945; Lang, 1981] and the quasicrystalline approximation for dense medium [Lax, 1951; Tsang and Kong, 1982,1983]. When the media have some specific structure such as the branching structure of vegetation [Yueh, et al., 1992] or sticky grains of snow [Ding, et al., 1994], additional care is needed to account for their respective structure factors. Consequently, the polarimetric backscattering coefficients are calculated to interpret the backscattering from various geophysical media.

However, due to the fact that calibrated polarimetric measurements together with detailed ground truth are relatively less available, most theoretical models only concern about the received power without considering the correlation among different polarized fields. Also, although numerous controlled experiments have been carried out and significant efforts were made in the theoretical modeling, much fewer works have been performed in the retrieval of geophysical parameters such as biomass of forest with the validated models. Since the multi-frequency polarimetric data have become available with the advance of radar technology, to take the advantage of the increasing dimensions of remote sensing data, it is important to consider the underlining processes of electromagnetic interaction with earth terrain at various frequencies and polarizations to increase the applications of the theoretical remote sensing models. Furthermore, the polarimetric backscattering data exhibit a strong dependence on the parameters of the earth's media. In the case of vegetation canopy, the backscattering coefficients depend on the density and height of the canopy, the moisture of

the vegetation and ground, the roughness of the ground, and the size and orientation of the trunks, branches and leaves. It is essential to consider the relationships among these parameters and scattering coefficients for different polarization states in order to retrieve the parameters of interest with better immunity from the fluctuation of other parameters.

The main concern of this research is to develop theoretical models for active and passive polarimetric remote sensing of forest and vegetation in order to utilize the available multi-frequency and polarimetric data available. The emphasis is on the ability of these theoretical models to simulate the polarimetric scattering and emission data to better understand the underlying physical processes. Calibrated data with measured ground truth will be used to validate these theoretical models and the validated models will be used to assess the applications of remote sensing data. For the theoretical development, the radiative transfer theory is applied with its extinction matrix and phase matrix modified depending on the characteristic of the medium. These theoretical models are applied to study the electromagnetic wave interactions with forest, vegetation or isolated trees. Attenuation and phase fluctuation caused by the foliage is also investigated in conjunction of statistical clutter model.

1.2 DESCRIPTION OF THESIS

A variety of theoretical models have been used for the electromagnetic modeling of the earth terrain such as snow, ice, and vegetation canopy [Tsang et al.,1985]. Among these models, the radiative transfer (RT) theory has been widely used to calculate radar backscattering coefficients from layered geophysical media and to interpret the experimental measurements due to its simplicity. In the RT theory, the radiative transfer equations, which govern the electromagnetic energy propagation through scattering media, are solved with appropriate boundary conditions. Various models have been developed based on this theory [Han et al., 1991; Shin and Kong, 1989; Tsang et al., 1984]. The key issue in the development of RT theory is the calculation of extinction matrix and phase matrix.

In this thesis, theoretical models are developed to calculate the scattering, attenuation, and emission of electromagnetic wave interaction with the earth terrain. To apply these theoretical models for the remote sensing purpose, several experimental measurements are used to compare with the theoretical simulation. In order to interpret the multi-frequency, polarimetric data, structure effect of the medium such as relative correlation and preferred orientation of scatterers are taken into consideration.

In Chapter 2, the radiative transfer (RT) theory for clustered vegetation structures is developed and used to interpret polarimetric radar backscattering measurement data from pine forest. The RT theory has been widely used to calculate radar backscattering coefficients from layered geophysical media and to interpret the measurement data. However, the conventional RT theory ignores the relative phase in-

formation associated with particles, which may play an important role in the overall scattering behavior for structured scatterers. To take into account the clustered structures in the radiative transfer theory, the scattering function of each cluster is calculated by considering the coherent scattered fields from each component with the clustered branches. The resulting phase matrix and extinction matrix is then used in the radiative transfer equations to calculate the polarimetric backscattering coefficients from the layered random medium embedded with vegetative clusters. A multi-scale structure model of pine forest, which includes trunks, primary and secondary branches, will be used to interpret and simulate the polarimetric radar response at P-band (0.44 GHz), L-band (1.25 GHz), C-band (5.3 GHz), and X-band (9.6 GHz).

The effect of tree branches and leaves structures on the scattering signature at multiple frequencies is investigated. Different scales of tree structures response differently at different frequencies. The fine structure of leaves will be important at higher frequencies such as C-band and X-band. On the other hand, it is necessary to consider the clustering effect at lower frequencies. This phenomenon will be demonstrated with the SIR-C/XSAR data collected over the Landes pine forest. The detailed ground truth was collected by CESBIO (Centre d'Etude Spatiale BIOsphere) in France.

In Chapter 3, Milli-meter wave scattering from isolated tree is investigated. Vegetation, as a large collection of scattering objects with different sizes and compositions, has very complicated electromagnetic scattering characteristics. It is important not only to the radar community as one of the "clutter" source, but also to the remote sensing community, whose major objective is to locate and identify different species and growing status of vegetation. With the advance of millimeter wave radar technology, considerable amounts of measurements have been made in recent years over

vegetation-covered terrain. Empirical models have been developed to provide parametric representation and hence classification of collected data. However, there have been comparatively few works on the physical models for the electromagnetic scattering characteristics of vegetation, especially in those with enough details to support high-resolution radar image analysis and synthesis.

Usually, the physical terrain is characterized in terms of layered random medium with either the continuous permittivity fluctuation or the random distributed discrete scatterers. In the three-dimensional milli-meter wave radar simulation, it is sometimes necessary to consider isolated trees and shrubs as part of the background. In this case, we may have to add additional parameters, such as the size of the canopy, when using the layered random medium model. Alternatively, a discrete random scatterer model is applied. This model provides means of summing the contributions from individual scatterers, including the multiple scattering effect, and allows us to work on a tree-by-tree basis. In this case, the tree trunk can be treated as a deterministic scatterer much like targets, whereas for branches and leaves we shall apply the random scatterer model to calculate their radar returns.

In this study, a tree is considered as a combination of trunk and crown, from which the scattering power for each part is calculated separately. Trunks are modelled as circular cylinders with random rough surface and the Kirchhoff's approximation is used to calculate the radar return power, with the attenuation caused by crown properly taken into account. Crown is modeled as a collection of randomly oriented discrete scatterers. Backscattering coefficient of the tree crown is calculated using the radiative transfer theory. Branches and coniferous leaves are modeled as circular cylinders of different sizes. Deciduous leaves are modelled as elliptical disks. The dimensions of these elements are obtained from measurements of physical samples

of tree. Finite cylinder approximation and physical optics approximation are used for the calculation of scattering from cylinders and disks, respectively. Theoretical predictions for radar range profile of deciduous trees are compared with the measurement data taken at Prado Regional Park, CA, and in Bend, Oregon by the Army Research Laboratory using a 94 GHz FMCW radar.

The attenuation and the phase and amplitude fluctuations of electromagnetic wave caused by foliage and their impacts on the synthetic aperture radar (SAR) image have is investigated in Chapter 4. MIT Lincoln Laboratory conducted a Foliage Penetration (FOPEN) experiment [Ayasli et al., 1991] to investigate the feasibility of detecting stationary targets located inside the forest. Based on the experimental data, the attenuation and the phase fluctuation caused by different polarizations, frequencies as well as the effect of depression angles and synthetic aperture length were analyzed [Toups, 1992]. In the experiment, transmitters were placed inside the forest and an airborne receiver was used to measure the one-way propagation. The one-way attenuation and phase fluctuation caused by the foliage are obtained by comparing the radiated field from a point source under the foliage to the radiated field from a point source in free space.

To simulate the electromagnetic response of a source under a layer of random medium, Chu et al. proposed a wave theory approach with continuous random medium model [Chu et al., 1992]. The mean attenuation as well as the variance of the phase fluctuations are obtained. However, small fluctuations are assumed in order to solve the problem analytically. Since the measured attenuation caused by foliage shows significant fluctuations, it is necessary to include the effect of large fluctuations in the theoretical models. The approach applied here is to relate the fluctuations in the field to the bistatic scattering coefficients from the scattered medium due to the

fact that the scattered intensities in all other directions besides the forward direction are incoherent in nature. As to the calculation of bistatic scattering coefficients, both wave theory and RT theory with either continuous random medium or discrete scatterer medium models can be utilized.

In this study, the attenuation and phase fluctuations of electromagnetic waves propagating through the foliage is investigated with the development of a radiative transfer model in conjunction with the statistical clutter model. The attenuation of average received field is obtained from the sum of absorption loss and scattering loss. The amplitude fluctuation of electromagnetic wave is calculated from the bistatic scattering coefficients using the radiative transfer theory. The phase fluctuation is obtained from the amplitude fluctuation assuming the phase of the fluctuation field is uniformly distributed from $-\pi$ to π. The average received power is obtained from the sum of the power of average field and the power of fluctuation field. The attenuation is then obtained by comparing the radiated power from a source under the foliage to the received power from a source in free space. Theoretical results are compared with experimental data collected by MIT Lincoln Laboratory during the 1990 Foliage Penetration Experiment. This theoretical model is also used to illustrate the polarization and angular dependencies of attenuation and phase fluctuations and to investigate how well an object obscured by the foliage can be imaged with synthetic aperture radar.

In Chapter 5, the polarimetric emission from the volume scattering is studied. It is commonly known that all four Stokes parameters emission from non azimuthally symmetrical medium is generally non-zero. However, usually the earth medium is assumed to have azimuthal symmetry property. It was first suggested by Tsang [1991] that all four Stokes parameters emission from a azimuthally non-symmetric medium

would be significantly different from zero. Emission from periodic soil surface has been studied experimentally [Nghiem, et al., 1991] and theoretically [Veysoglu, et al., 1991]. The numerical results indicated that the plowed field would have the third Stokes parameter (U) as high as $40K$. There are also studies looking into the application to the ocean surface. Several studies with periodic water surfaces [Johnson, et al., 1994, Yueh, et al., 1994] prompt an experiment of emission from ocean surface. [Yueh, et al., 1995] It's been shown that the third stokes parameter from ocean surface reveal wind direction caused by the azimuthal asymmetry. Although some of works have been done regarding the applications of polarimetric emission from surface such as the detection of ocean wind direction, very few studies investigated the effect of azimuthal non-symmetry on volume scattering and its impact on parameters retrieval.

A vegetation medium is modeled as a layer of random medium with either continuous permittivity fluctuation or random distributed discrete scatterers on top of a flat or rough ground. The ground half space would be tilted at certain angle and/or the vegetation would be also tilted in certain direction. For the calculation of the emissivity from random medium, fluctuation-dissipation theory can be used to obtain the emission vector. Alternatively, the Kirchhoff's law which relates passive emission to the active scattering coefficients is used. For the calculation of bi-static scattering coefficients, vector radiative transfer theory (RT) is applied. Both direct calculation of emission from the RT equations and the derivation of emissivity using Kirchhoff's law will be compared. In addition, experimental data collected over alfalfa field at various growth stage at 10 GHz are used to validate the theoretical model. The experiment is conducted by IROE in Italy. Ground truth such as the height of vegetation, the water content of vegetation and soil, and the leaf area index (LAI) or fractional volume of

vegetation have been collected for the experiments. The theoretical model is used to investigate the polarimetric emission from azimuthally asymmetrical medium.

And finally, the chapter 6 summarizes the work and concludes this thesis.

Chapter 2.

Polarimetric Active Remote Sensing of Forest

ABSTRACT – A radiative transfer model for clustered vegetation structures is developed and used to interpret polarimetric radar backscattering measurement data from forests. To incorporate the clustered structures with the radiative transfer theory, the scattering function of each cluster is calculated by taking into account the coherent wave interaction of the scattered field from each component. Subsequently, the resulting phase matrix is used in the radiative transfer equations to calculate the polarimetric backscattering coefficients from layered random media embedded with vegetation clusters. A multi-scale structure model of a forest, which includes the trunks, the primary and secondary branches and the leaves, is used to predict the polarimetric radar response at multiple frequencies. The theoretical model is used to interpret the measured data at the Landes pine forest during the SIR-C/XSAR missions. The Clustering effect of the tree structure and the coherent effect due to the fine structure of the leaves are shown to have impacts on the polarimetric signatures of forest.

2.1 INTRODUCTION

In recent years, the application of radar polarimetry for active remote sensing of the earth terrain has inspired extensive interests. [Evans, et al., 1988] A variety of theoretical models have been used for electromagnetic modeling of the earth terrain such as snow, ice, and vegetation canopy [Tsang et al.,1985]. The radiative transfer (RT) theory has been widely used to calculate radar backscattering coefficients from layered geophysical media and to interpret the experimental measurements. In the RT theory, the radiative transfer equations, which govern the electromagnetic energy propagation through scattering media, is used with appropriate boundary conditions. Various models have been developed based on this theory [Han et al., 1991; Shin and Kong, 1989; Tsang et al., 1984]. The important aspect is that the calculation of the elements in the RT equations needs to take the scatterer structure into account. For instance, when the fractional volume of the medium is high, the scatterer positions are no longer independent to each other, and the pair distribution function of the scatterer is needed to be considered [Tsang and Kong, 1993]. On the other hand, when the fractional volume of the medium is small such as in the case of vegetated terrain, the scatterers may also have certain structure depending on the species of particles. However, the conventional RT theory ignores the relative phase information associated with the scattering by scatterers. Since tree have apparent structure despite its low fractional volume, the tree structure may play an important role in the overall scattering behavior [Yueh et al., 1992]. In a forest, the canopy consists of different length scales — the trunk, the primary branches, the secondary branches, and the leaves. The elements of each scale are connected to the elements of other scales in a manner which can be statistically described by the unique architecture pertaining to each tree species group.

In this chapter, a four-layer RT model is constructed for the modeling of a pine

forest. The four layers include a crown layer, a trunk layer, an understory layer, and a grass layer over the ground surface. The trunks, branches and coniferous leaves are modeled as circular cylinders while elliptical disks are used to model the deciduous leaves. The surface height and correlation function of the bottom rough surface are described by the Gaussian processes. The scattering properties of structured pine trees is taken into account in this model by incorporating the branching model [Yueh et al., 1992] into the phase matrix of the RT equation. Part of this work has been published in cooperation with researchers of the Centre d'Etude Spatiale BIOsphere (CESBIO) [Beaudoin, et al., 1994, Hsu et al., 1994a]. Section 2.2 summarizes the basics of radiative transfer theory. In Section 2.3, the phase matrix and extinction matrix based on the branching model is formulated. Section 2.4 presents the comparison of theoretical calculations with the experimental data. Finally, discussion and conclusion is given in Section 2.5.

2.2 RADIATIVE TRANSFER MODEL OF FOREST

A forest canopy is modeled as a multi-layered random medium depicted in Figure 1(a). The scattering regions n are layers of thickness h_n, n=1,2,3, within each region the discrete scatterers are embedded in a homogeneous background. The interface between region 4 and region t can be either a planar surface or a random rough surface with or without slope. The random rough surface is described by a Gaussian random process in height and correlation.

The vector radiative transfer equation for the specific intensity in each scattering region is of the form

$$\cos\theta \frac{d\bar{I}(\theta,\phi,z)}{dz} = -\bar{\bar{\kappa}}_e(\theta,\phi,z)\cdot\bar{I}(\theta,\phi,z) + \int_{4\pi} d\Omega' \bar{\bar{P}}(\theta,\phi;\theta',\phi')\cdot\bar{I}(\theta',\phi',z) \tag{1}$$

where the Stokes vector $\bar{I}$ contains information regarding the field intensity and the phase relation of the two orthogonal polarizations and is defined as

$$\bar{I} = \begin{pmatrix} I_h \\ I_v \\ U \\ V \end{pmatrix} = \frac{1}{\eta}\begin{pmatrix} \langle|E_h|^2\rangle \\ \langle|E_v|^2\rangle \\ 2\,\mathrm{Re}\langle E_v E_h^*\rangle \\ 2\,\mathrm{Im}\langle E_v E_h^*\rangle \end{pmatrix} \tag{2}$$

In (2), the subscripts h and v represent the horizontal and vertical polarizations, respectively. The bracket $\langle\ \rangle$ denotes ensemble average over the size and orientation distributions of scatterers and $\eta = \sqrt{\mu_0/\epsilon_0}$ is the free-space impedance.

The extinction matrix $\bar{\bar{\kappa}}_e$ represents the attenuation caused by both the scattering and absorption, and can be obtained through the optical theorem in terms of

forward scattering functions [Tsang et al., 1985]. It is given as

$$\bar{\bar{\kappa}}_e(\theta,\phi) = \frac{2\pi n_0}{k} \begin{pmatrix} 2Im\langle f_{hh}\rangle & 0 & Im\langle f_{hv}\rangle & Re\langle f_{hv}\rangle \\ 0 & 2Im\langle f_{vv}\rangle & Im\langle f_{vh}\rangle & -Re\langle f_{vh}\rangle \\ 2Im\langle f_{vh}\rangle & 2Im\langle f_{hv}\rangle & Im\langle f_{vv}+f_{hh}\rangle & Re\langle f_{vv}-f_{hh}\rangle \\ -2Re\langle f_{vh}\rangle & 2Re\langle f_{hv}\rangle & Re\langle f_{vv}-f_{hh}\rangle & Im\langle f_{vv}+f_{hh}\rangle \end{pmatrix} \tag{3}$$

The phase matrix $\bar{\bar{P}}(\theta,\phi;\theta',\phi')$ characterizes the scattering of the Stokes vector from the (θ',ϕ') direction into the (θ,ϕ) direction. The phase matrix can be formulated in terms of scattering functions of the randomly distributed discrete scatterers, and it has the following form

$$\bar{\bar{P}}(\theta,\phi,\theta',\phi') = n_0 \begin{pmatrix} \langle|f_{hh}|^2\rangle & \langle|f_{hv}|^2\rangle & Re\langle f_{hv}f_{hh}^*\rangle & -Im\langle f_{hv}f_{hh}^*\rangle \\ \langle|f_{vh}|^2\rangle & \langle|f_{vv}|^2\rangle & Re\langle f_{vv}f_{vh}^*\rangle & -Im\langle f_{vv}f_{vh}^*\rangle \\ 2Re\langle f_{vh}f_{hh}^*\rangle & 2Re\langle f_{vv}f_{hv}^*\rangle & Re\langle f_{vv}f_{hh}^*+f_{vh}f_{hv}^*\rangle & -Im\langle f_{vv}f_{vh}^*-f_{vh}f_{hv}^*\rangle \\ 2Im\langle f_{vh}f_{hh}^*\rangle & 2Im\langle f_{vv}f_{hv}^*\rangle & Im\langle f_{vv}f_{hh}^*+f_{vh}f_{hv}^*\rangle & Re\langle f_{vv}f_{hh}^*-f_{vh}f_{hv}^*\rangle \end{pmatrix} \tag{4}$$

In equations (3) and (4), n_0 is number density of scatterers, f_{ab} is the scattering function for the incident field with polarization b and the scattered field with polarization a, a, b can be horizontal or vertical polarization.

Considering a plane wave incident on a particle, scattering matrix associated with scatterer is defined as

$$\begin{pmatrix} E_{hs} \\ E_{vs} \end{pmatrix} = \frac{e^{ikr}}{r} \begin{pmatrix} f_{hh} & f_{hv} \\ f_{vh} & f_{vv} \end{pmatrix} \cdot \begin{pmatrix} E_{hi} \\ E_{vi} \end{pmatrix} \tag{5}$$

which relates the incident electric field to the scattered electric field for horizontal and vertical polarizations. The scattering matrices obtained from the finite cylinder approximation for circular cylinder and from the physical optics approximation for elliptical disk, are given in the Appendix A and B, respectively.

Since the effective permittivity of each vegetation layer is very close to that of free space, reflection between different vegetation layers is neglected except the reflection at the ground boundary. The radiative transfer equations with the boundary

conditions can be solved using the iterative method to calculate the polarimetric backscattering coefficients [Tsang et al., 1985]. First, we let the specific intensity of the downgoing wave to be the same as the incident wave and ignore the reflections at the interface between regions n and $n-1$. This is a good approximation for a vegetation layer where the effective permittivity is very close to that of the air and there is no coupling between upgoing and downgoing intensities at interface between layers. At the bottom boundary $(z=-d_N)$, the coupling matrix is evaluated using the Fresnel reflection coefficients for flat ground or the Kirchhoff diffraction integral for the random rough surface. Hence the boundary conditions can be written as

$$\begin{aligned}
&\overline{I}_1(\pi-\theta,\phi,z=0)=\overline{I}_0\delta(\cos\theta-\cos\theta_0)\delta(\phi-\phi_0)\\
&\overline{I}_N(\theta,\phi,z=-d)=\int_0^{2\pi}d\phi'\int_0^{\frac{\pi}{2}}d\theta' sin\theta'\overline{\overline{R}}_N(\theta,\phi;\theta',\phi')\cdot\overline{I}_N(\pi-\theta',\phi',z=-d_N)\\
&\overline{I}_n(\theta,\phi,z=-d_n)=\overline{I}_{n+1}(\theta,\phi,z=-d_n)\\
&\overline{I}_n(\pi-\theta,\phi,z=-d_{n-1})=\overline{I}_{n-1}(\pi-\theta,\phi,z=-d_{n-1})
\end{aligned}\tag{6}$$

where $n=2,3,4.....N-1$ and the coupling matrix $\overline{\overline{R}}_N$ which includes incoherent and coherent rough surface scattering using Kirchhoff's approximation is described in Appendix C.

The iterative solution to the RT equation is obtained by assuming that the scattering effect is smaller than the extinction, i.e., for a layered medium with small albedo or small optical thickness, we can solve the radiative transfer equations iteratively. As the first term on the right-hand side of (1) is the dominant term, the zeroth-order solution is obtained by ignoring the second term on the right hand side which is the scattering contribution from other directions. By substituting the zeroth-order solution of the specific intensity into the integral part of the RT equation, we obtain the first-order solution. Hence, higher order solutions can be readily obtained by following this scheme.

2.2.1 First Order Iterative Solution

Let the upgoing and downgoing waves be separated by restricting $0 < \theta < \pi/2$, this leads to the following two coupled equations

$$\cos\theta \frac{d}{dz}\bar{I}_n(\theta,\phi,z) = -\bar{\bar{K}}_e(\theta,\phi)\cdot\bar{I}_n(\theta,\phi,z) + \bar{S}_n(\theta,\phi,z) \tag{7a}$$

$$-\cos\theta \frac{d}{dz}\bar{I}_n(\pi-\theta,\phi,z) = -\bar{\bar{K}}_e(\pi-\theta,\phi)\cdot\bar{I}_n(\pi-\theta,\phi,z) + \bar{W}_n(\pi-\theta,\phi,z) \tag{7b}$$

where $\bar{I}_n(\theta,\phi,z)$ and $\bar{I}_n(\pi-\theta,\phi,z)$ are the upgoing and the downgoing specific intensities in the n-th layer. The two source terms $\bar{S}_n(\theta,\phi,z)$ and $\bar{W}_n(\pi-\theta,\phi,z)$ account for the scattering effects and hence include the coupling of specific intensities between the upgoing and the downgoing waves.

$$\begin{aligned}\bar{S}_n(\theta,\phi,z) = \int_0^{2\pi} d\phi' \int_0^{\frac{\pi}{2}} d\theta' sin\theta' [&\bar{\bar{P}}_n(\theta,\phi;\theta',\phi')\cdot\bar{I}_n(\theta',\phi',z) \\ &+\bar{\bar{P}}_n(\theta,\phi;\pi-\theta',\phi')\cdot\bar{I}_n(\pi-\theta',\phi',z)]\end{aligned} \tag{8a}$$

$$\begin{aligned}\bar{W}_n(\pi-\theta,\phi,z) = \int_0^{2\pi} d\phi' \int_0^{\frac{\pi}{2}} d\theta' sin\theta' [&\bar{\bar{P}}_n(\pi-\theta,\phi;\theta',\phi')\cdot\bar{I}_n(\theta',\phi',z) \\ &+\bar{\bar{P}}_n(\pi-\theta,\phi;\pi-\theta',\phi')\cdot\bar{I}_n(\pi-\theta',\phi',z)]\end{aligned} \tag{8b}$$

The zeroth-order equations as obtained by neglecting the source terms in equation (7),

$$\cos\theta \frac{d}{dz}\bar{I}_n^{(0)}(\theta,\phi,z) = -\bar{\bar{K}}_e(\theta,\phi)\cdot\bar{I}_n^{(0)}(\theta,\phi,z) \tag{9a}$$

$$-\cos\theta \frac{d}{dz}\bar{I}_n^{(0)}(\pi-\theta,\phi,z) = -\bar{\bar{K}}_e(\pi-\theta,\phi)\cdot\bar{I}_n^{(0)}(\pi-\theta,\phi,z) \tag{9b}$$

Equations (9) are in the form of typical eigenvalue problems. Assuming the solution is of the form $\exp(-\beta \sec\theta z)$, the four eigenvalues can be obtained as

$$\begin{aligned} \beta_1 &= 2Im(K_1) \\ \beta_2 &= 2Im(K_2) \\ \beta_3 &= i(K_2^* - K_1) \\ \beta_4 &= i(K_1^* - K_2) \end{aligned} \tag{10}$$

where K_1 and K_2 are the two effective propagation constants

$$\begin{aligned} K_1 &= k + \frac{n_0\pi}{k}[< f_{vv}(\theta,\phi;\theta,\phi) > + < f_{hh}(\theta,\phi;\theta,\phi) > -R] \\ K_2 &= k + \frac{n_0\pi}{k}[< f_{vv}(\theta,\phi;\theta,\phi) > + < f_{hh}(\theta,\phi;\theta,\phi) > +R] \end{aligned} \tag{11}$$

and

$$R = \sqrt{[< f_{vv}(\theta,\phi;\theta,\phi) > - < f_{hh}(\theta,\phi;\theta,\phi) >]^2 + 4 < f_{hv}(\theta,\phi;\theta,\phi) >< f_{vh}(\theta,\phi;\theta,\phi) >} \tag{12}$$

under the condition

$$sgnRe(R) = sgn[< f_{vv} - f_{hh} >] \tag{13}$$

such that K_1 and K_2 will approach the effective propagation constants for the horizontally and vertically polarized waves, respectively, in the limit of small cross-polarization coupling.

We define a 4×4 "eigenmatrix" $\overline{\overline{E}}_n$ with its columns being the four eigenvectors corresponding to the four eigenvalues given in (11). Then this eigenmatrix satisfies

$$\overline{\overline{E}}_n \cdot \overline{\overline{\beta}}_n = \overline{\overline{K}}_e \cdot \overline{\overline{E}}_n \tag{14}$$

where $\overline{\overline{\beta}}_n$ is a 4 × 4 diagonal matrix with the eigenvalues β_i as its i-th diagonal element. The eigenmatrix can be expressed as follows

$$\overline{\overline{E}}(\theta,\phi)=\begin{pmatrix} 1 & |b_2|^2 & b_2 & b_2^* \\ |b_1|^2 & 1 & b_1^* & b_1 \\ 2Reb_1 & 2Reb_2 & 1+b_1^*b_2 & 1+b_1b_2^* \\ -2Imb_1 & 2Imb_2 & i(1-b_1^*b_2) & -i(1-b_1b_2^*) \end{pmatrix} \tag{15}$$

where

$$\begin{aligned} b_1 &= \frac{2n_0 < f_{hv}(\theta,\phi;\theta,\phi) >}{n_0 < f_{vv}(\theta,\phi;\theta,\phi) > -n_0 < f_{hh}(\theta,\phi;\theta,\phi) > +R} \\ b_2 &= \frac{2n_0 < f_{vh}(\theta,\phi;\theta,\phi) >}{n_0 < f_{hh}(\theta,\phi;\theta,\phi) > -n_0 < f_{vv}(\theta,\phi;\theta,\phi) > -R} \end{aligned} \tag{16}$$

To solve the coupled equation (7), the specific intensity is decomposed into its characteristic components, i.e., the eigenvectors, by defining $\overline{I}_n = \overline{\overline{E}}_n \cdot \overline{J}_n$. Then the radiative transfer equation for the upgoing wave (7) becomes

$$\begin{aligned} \cos\theta \frac{d}{dz}\overline{J}_n(\theta,\phi,z) &= -\overline{\overline{E}}_n^{-1}(\theta,\phi)\overline{\overline{K}}_e(\theta,\phi)\overline{\overline{E}}_n(\theta,\phi)\cdot\overline{J}_n(\theta,\phi,z)+\overline{\overline{E}}_n^{-1}\cdot\overline{S}_n(\theta,\phi,z) \\ &= -\overline{\overline{\beta}}_n(\theta,\phi)\cdot\overline{J}_n(\theta,\phi,z)+\overline{\overline{E}}_n^{-1}(\theta,\phi)\cdot\overline{S}_n(\theta,\phi,z) \end{aligned} \tag{17}$$

where (14) has been used. To incorporate the boundary conditions, we multiply both sides of the above equation by $\int_{-d_n}^{z}\overline{\overline{D}}_n(\beta_n(\theta,\phi)\sec\theta z')dz'$ and obtain

$$\begin{aligned} \cos\theta \int_{-d_n}^{z} & \overline{\overline{D}}_n(\beta_n(\theta,\phi)\sec\theta z')\cdot\frac{d}{dz'}\overline{J}(\theta,\phi,z')dz' \\ &= -\int_{-d_n}^{z}\overline{\overline{D}}_n(\beta_n(\theta,\phi)\sec\theta z')\overline{\overline{\beta}}_n(\theta,\phi)\cdot\overline{J}_n(\theta,\phi,z')dz' \\ &\quad +\int_{-d_n}^{z}\overline{\overline{D}}_n(\beta_n(\theta,\phi)\sec\theta z')\overline{\overline{E}}_n^{-1}(\theta,\phi)\cdot\overline{S}_n(\theta,\phi,z')dz' \end{aligned} \tag{18}$$

where $\overline{\overline{D}}_n(\beta_n(\theta,\phi)\sec\theta z')$ is the 4×4 diagonal matrix with $e^{(\beta_{n_i}(\theta,\phi)\sec\theta z')}$ as its i-th diagonal elements. Here β_{n_i} is the i-th eigenvalue of $\overline{\overline{K}}_e$ in layer n. Integrating

by parts the left-hand side of the above equation yields

$$\begin{aligned}
&\cos\theta\overline{\overline{D}}_n(\beta_n(\theta,\phi)\sec\theta z)\cdot\overline{J}_n(\theta,\phi,z)\\
&\quad=\cos\theta\overline{\overline{D}}_n(-\beta_n(\theta,\phi)\sec\theta d_n)\cdot\overline{J}(\theta,\phi,-d_n)\\
&\qquad+\int_{-d_n}^{z}\overline{\overline{D}}_n(\beta_n(\theta,\phi)\sec\theta z')\overline{\overline{E}}_n^{-1}(\theta,\phi)\cdot\overline{S}_n(\theta,\phi,z')dz'
\end{aligned}\tag{19}$$

After recovering the original notation of $\overline{I}(\theta,\phi,z)$, we have

$$\begin{aligned}
\overline{I}_n(\theta,\phi,z)&=\overline{\overline{E}}_n(\theta,\phi)\overline{\overline{D}}_n(-\beta_n(\theta,\phi)sec\theta(z+d_n))\overline{\overline{E}}_n^{-1}(\theta,\phi)\cdot\overline{I}_n(\theta,\phi,-d_n)\\
&+\sec\theta\overline{\overline{E}}_n(\theta,\phi)\int_{-d_n}^{z}\overline{\overline{D}}_n(\beta_n(\theta,\phi)\sec\theta(z'-z))\overline{\overline{E}}_n^{-1}(\theta,\phi)\cdot\overline{S}_n(\theta,\phi,z')dz'
\end{aligned}\tag{20}$$

It is instructive to view $\overline{\overline{E}}_n\ \overline{\overline{D}}_n\ \overline{\overline{E}}_n^{-1}$ in the above equation as a propagation operator which decomposes a specific intensity vector $\overline{I}_n$ into its characteristic components, and propagates each component with its own attenuation rate (e.g., $\beta_n\sec\theta$) in the z-direction, then recombines the characteristic components back into $\overline{I}_n$ at a new point in space. Thus we can interpret the first term on the right-hand side of (20) as the contribution from the upgoing $\overline{I}_n$ propagating from the boundary at $z=-d_n$ to z, and the second term as the contribution from the upgoing $\overline{I}_n$ created by scattering taking place at z' propagating to z.

Similarly, for the downgoing wave, we have

$$\begin{aligned}
\overline{I}_n(\pi-\theta,\phi,z)&=\overline{\overline{E}}_n(\pi-\theta,\phi)\overline{\overline{D}}_n(\beta_n(\pi-\theta,\phi)\sec\theta(z+d_{n-1}))\overline{\overline{E}}_n^{-1}(\pi-\theta,\phi)\cdot\overline{I}_n(\pi-\theta,\phi,-d_{n-1})\\
&+\sec\theta\overline{\overline{E}}_n(\pi-\theta,\phi)\int_{z}^{-d_{n-1}}\overline{\overline{D}}_n(\beta_n(\pi-\theta,\phi)\sec\theta(z-z'))\overline{\overline{E}}_n^{-1}(\pi-\theta,\phi)\cdot\overline{W}_n(\pi-\theta,\phi,z')dz'
\end{aligned}\tag{21}$$

The first term on the right-hand side of (21) can be interpreted as the contribution from the downgoing $\overline{I}_n$ propagating from the boundary at $z=-d_{n-1}$ to z, and the second term as the contribution from the downgoing $\overline{I}_n$ created by scattering taking place at z' propagating to z.

Making use of the boundary conditions (6) to replace $\overline{I}_n(\theta,\phi,-d_n)$ and $\overline{I}_n(\pi-\theta,\phi,-d_{n-1})$ in the above two equations and ignoring the coupling between upgoing and downgoing intensities at other layers, we have

$$\begin{aligned}\overline{I}_n(\pi-\theta,\phi,z) &= \overline{\overline{E}}_n(\pi-\theta,\phi)\overline{\overline{D}}_n(\beta_n(\pi-\theta,\phi)\sec\theta(z+d_{n-1}))\overline{\overline{E}}_n^{-1}(\pi-\theta,\phi)\\ &\cdot\prod_{i=n-1}^{1}(\overline{\overline{E}}_i\cdot\overline{\overline{D}}_i(\beta_i(\pi-\theta,\phi)\sec\theta h_i)\cdot\overline{\overline{E}}_i^{-1})\cdot\overline{I}_0\delta(\cos\theta-\cos\theta_0)\delta(\phi-\phi_0)\\ &+\sec\theta\overline{\overline{E}}_n\int_z^{-d_{n-1}}\overline{\overline{D}}_n(\beta_n(\pi-\theta,\phi)\sec\theta(z-z'))\overline{\overline{E}}_n^{-1}(\pi-\theta,\phi)\cdot\overline{W}_n(\pi-\theta,\phi,z')dz'\end{aligned} \tag{22}$$

for the downgoing wave, and

$$\begin{aligned}&\overline{I}_n(\theta,\phi,z)=\\ &\overline{\overline{E}}_n\cdot\overline{\overline{D}}_n(-\beta_n(\theta,\phi)\sec\theta(z+d_n))\overline{\overline{E}}_n^{-1}\cdot\prod_{i=n+1}^{N}(\overline{\overline{E}}_i\cdot\overline{\overline{D}}_i(-\beta_i(\theta,\phi)\sec\theta h_i)\overline{\overline{E}}_i^{-1})\\ &\int_0^{2\pi}d\phi'\int_0^{\frac{\pi}{2}}d\theta'\sin\theta'\overline{\overline{R}}(\theta,\phi;\theta',\phi')\cdot\prod_{i=N}^{1}(\overline{\overline{E}}_i\cdot\overline{\overline{D}}_i(-\beta_i(\pi-\theta',\phi')\sec\theta' h_i)\overline{\overline{E}}_i^{-1})\\ &\cdot\overline{I}_0\delta(\cos\theta'-\cos\theta_0)\delta(\phi'-\phi_0)\\ &+\overline{\overline{E}}_n\cdot\overline{\overline{D}}_n(-\beta_n(\theta,\phi)\sec\theta(z+d_n))\overline{\overline{E}}_n^{-1}\cdot\prod_{i=n+1}^{N}(\overline{\overline{E}}_i\cdot\overline{\overline{D}}_i(-\beta_i(\theta,\phi)\sec\theta h_i)\overline{\overline{E}}_i^{-1})\\ &\int_0^{2\pi}d\phi'\int_0^{\frac{\pi}{2}}d\theta'\sin\theta'\overline{\overline{R}}(\theta,\phi;\theta',\phi')\cdot\prod_{i=N}^{n+1}(\overline{\overline{E}}_i\cdot\overline{\overline{D}}_i(-\beta_i(\pi-\theta',\phi')\sec\theta' h_i)\overline{\overline{E}}_i^{-1})\cdot\sec\theta'\\ &\overline{\overline{E}}_n\int_{-d_n}^{-d_{n-1}}\overline{\overline{D}}_n(\beta_n(\pi-\theta',\phi')\sec\theta'(-d_n-z'))\overline{\overline{E}}_n^{-1}(\pi-\theta',\phi')\cdot\overline{W}_n(\pi-\theta',\phi',z')dz'\\ &+\sec\theta\overline{\overline{E}}_n(\theta,\phi)\int_{-d_n}^{z}\overline{\overline{D}}_n(\beta_n(\theta,\phi)\sec\theta(z'-z))\overline{\overline{E}}_n^{-1}(\theta,\phi)\cdot\overline{S}_n(\theta,\phi,z')dz'\end{aligned} \tag{23}$$

for the upgoing wave. h_n is the thickness of region n, or $h_n = d_n - d_{n-1}$. Here we ignore all other source terms $\overline{S}$ and $\overline{W}$ except those in layer n.

Now we can identify the zeroth-order solution by ignoring scattering terms involving $\overline{S}$ and $\overline{W}$. The zeroth order solutions for the up and down-going waves

are

$$\bar{I}_n^{(0)}(\theta,\phi,z) = \bar{\bar{E}}_n\bar{\bar{D}}_n(-\beta_n(\theta,\phi)\sec\theta(z+d_n))\bar{\bar{E}}_n^{-1}\cdot\prod_{i=n+1}^{N}(\bar{\bar{E}}_i\bar{\bar{D}}_i(-\beta_n(\theta,\phi)\sec\theta h_i)\bar{\bar{E}}_i^{-1}) \cdot\bar{\bar{R}}(\theta,\phi;\theta_0,\phi_0)\cdot\prod_{i=N}^{1}(\bar{\bar{E}}_i\bar{\bar{D}}_i(\beta_n(\pi-\theta_0,\phi_0)\sec\theta_0 h_i)\bar{\bar{E}}_i^{-1})\bar{I}_0 \tag{24a}$$

$$\bar{I}_n^{(0)}(\pi-\theta,\phi,z) = \bar{\bar{E}}_n\bar{\bar{D}}_n(\beta_n(\pi-\theta,\phi)\sec\theta(z+d_{n-1}))\bar{\bar{E}}_n^{-1} \cdot\prod_{i=n-1}^{1}(\bar{\bar{E}}_i\bar{\bar{D}}_i(\beta_i(\pi-\theta,\phi)\sec\theta h_i)\bar{\bar{E}}_i^{-1})\cdot\bar{I}_0\delta(\cos\theta-\cos\theta_0)\delta(\phi-\phi_0) \tag{24b}$$

which is the solution of (9) subject to the boundary condition (6).

To derive the first-order solution, the source terms $\bar{S}$ and $\bar{W}$ are calculated by substituting $\bar{I}_n^{(0)}(\theta,\phi,z)$ and $\bar{I}_n^{(0)}(\pi-\theta,\phi,z)$ into the integral part of (8).

$$\begin{aligned}\bar{S}_n^{(0)}(\theta,\phi,z) = {} & \int d\Omega'\bar{\bar{P}}_n(\theta,\phi;\theta',\phi')\cdot\bar{\bar{E}}_n\cdot\bar{\bar{D}}_n(-\beta_n(\theta',\phi')\sec\theta'(z+d_n))\bar{\bar{E}}_n^{-1}\\ & \cdot\prod_{i=n+1}^{N}(\bar{\bar{E}}_i\cdot\bar{\bar{D}}_i(-\beta_n(\theta',\phi')\sec\theta' h_i)\bar{\bar{E}}_i^{-1})\\ & \cdot\bar{\bar{R}}(\theta',\phi';\theta_0,\phi_0)\cdot\prod_{i=N}^{1}(\bar{\bar{E}}_i\cdot\bar{\bar{D}}_i(\beta_i(\pi-\theta_0,\phi_0)\sec\theta_0 h_i)\bar{\bar{E}}_i^{-1})\bar{I}_0\\ & +\bar{\bar{P}}_n(\theta,\phi;\pi-\theta_0,\phi_0)\cdot\bar{\bar{E}}_n\bar{\bar{D}}_n(\beta_n(\pi-\theta_0,\phi_0)\sec\theta_0(z+d_{n-1}))\bar{\bar{E}}_n^{-1}\\ & \cdot\prod_{i=n-1}^{1}(\bar{\bar{E}}_i\bar{\bar{D}}_i(\beta_i(\pi-\theta_0,\phi_0)\sec\theta_0 h_i)\cdot E_i^{-1})\cdot\bar{I}_0\end{aligned} \tag{25a}$$

$$\overline{W}_n^{(0)}(\pi-\theta,\phi,z)=\int d\Omega'\overline{\overline{P}}_n(\pi-\theta,\phi;\theta',\phi')\cdot\overline{\overline{E}}_n\cdot\overline{\overline{D}}_n(-\beta_n(\theta',\phi')\sec\theta'(z+d_n))$$
$$\overline{\overline{E}}_n^{-1}\cdot\prod_{i=n+1}^{N}(\overline{\overline{E}}_i\cdot\overline{\overline{D}}_i(-\beta_i(\theta',\phi')\sec\theta h_i)\overline{\overline{E}}_i^{-1})$$
$$\cdot\overline{\overline{R}}(\theta',\phi';\theta_0,\phi_0)\cdot\prod_{i=N}^{1}(\overline{\overline{E}}_i\cdot\overline{\overline{D}}_i(\beta_i(\pi-\theta_0,\phi_0)\sec\theta_0 h_i)\overline{\overline{E}}_i^{-1})\cdot\overline{I}_0$$
$$+\overline{\overline{P}}_n(\pi-\theta,\phi;\pi-\theta_0,\phi_0)\cdot\overline{\overline{E}}_n\overline{\overline{D}}_n(\beta_n(\pi-\theta_0,\phi_0)\sec\theta_0(z+d_{n-1}))\overline{\overline{E}}_n^{-1}$$
$$\prod_{i=n-1}^{1}(\overline{\overline{E}}_i\overline{\overline{D}}_i(\beta(\pi-\theta_0,\phi_0)\sec\theta_0 h_i)\cdot E_i^{-1})\cdot\overline{I}_0 \tag{25b}$$

Thereafter we can derive the first-order solution for the upgoing wave at $z=-d_{n-1}$ in terms of the incident specific intensity $\overline{I}_0$ by substituting $\overline{S}_n^{(0)}$ and $\overline{W}_n^{(0)}$ into (23). The first term in (23) is the zeroth-order solution as shown in (24) while the first-order solution is contained in the second and the third terms. Let us designate them as $\overline{I}_{n,1}^{(1)}$ and $\overline{I}_{n,2}^{(1)}$.

$$
\begin{aligned}
&\bar{I}_{n,1}^{(1)}(\theta,\phi,-d_{n-1}) = \\
&\quad \overline{\overline{E}}_n \cdot \overline{\overline{D}}_n(-\beta_n(\theta,\phi)\sec\theta(-d_{n-1}+d_n))\overline{\overline{E}}_n^{-1} \cdot \prod_{i=n+1}^{N} (\overline{\overline{E}}_i \cdot \overline{\overline{D}}_i(-\beta_i(\theta,\phi)\sec\theta h_i)\overline{\overline{E}}_i^{-1}) \\
&\quad \cdot \int_0^{2\pi} d\phi' \int_0^{\frac{\pi}{2}} d\theta' \sin\theta' \overline{\overline{R}}(\theta,\phi;\theta',\phi') \cdot \prod_{i=N}^{n+1} (\overline{\overline{E}}_i \cdot \overline{\overline{D}}_i(-\beta_i(\pi-\theta',\phi')\sec\theta' h_i)\overline{\overline{E}}_i^{-1}) \\
&\quad \cdot \sec\theta' \overline{\overline{E}}_n(\pi-\theta',\phi') \int_{-d_n}^{-d_{n-1}} \overline{\overline{D}}_n(\beta_n(\pi-\theta',\phi')\sec\theta'(-d_n-z'))\overline{\overline{E}}_n^{-1}(\pi-\theta',\phi') \\
&\quad \cdot \overline{\overline{P}}_n(\pi-\theta',\phi';\pi-\theta_0,\phi_0) \cdot \overline{\overline{E}}_n \cdot \overline{\overline{D}}_n(\beta_n(\pi-\theta_0,\phi_0)\sec\theta_0(z'+d_{n-1}))\overline{\overline{E}}_n^{-1} \\
&\quad \cdot \prod_{i=n-1}^{1} (\overline{\overline{E}}_i\overline{\overline{D}}_i(\beta_i(\pi-\theta_0,\phi_0)\sec\theta_0 h_i) \cdot E_i^{-1}) \cdot \bar{I}_0 \\
&\quad + \overline{\overline{E}}_n \cdot \overline{\overline{D}}_n(-\beta_n(\theta,\phi)\sec\theta(-d_{n-1}+d_n))\overline{\overline{E}}_n^{-1} \cdot \prod_{i=n+1}^{N} (\overline{\overline{E}}_i \cdot \overline{\overline{D}}_i(-\beta_i(\theta,\phi)\sec\theta h_i)\overline{\overline{E}}_i^{-1}) \\
&\quad \cdot \int_0^{2\pi} d\phi' \int_0^{\frac{\pi}{2}} d\theta' \sin\theta' \overline{\overline{R}}(\theta,\phi;\theta',\phi') \cdot \prod_{i=N}^{n+1} (\overline{\overline{E}}_i \cdot \overline{\overline{D}}_i(-\beta_i(\pi-\theta',\phi')\sec\theta' h_i)\overline{\overline{E}}_i^{-1}) \\
&\quad \cdot \sec\theta' \overline{\overline{E}}_n(\pi-\theta',\phi') \int_{-d_n}^{-d_{n-1}} \overline{\overline{D}}_n(\beta_n(\pi-\theta',\phi')\sec\theta'(-d_n-z'))\overline{\overline{E}}_n^{-1}(\pi-\theta',\phi') \\
&\quad \int d\Omega'' \overline{\overline{P}}_n(\pi-\theta',\phi';\theta'',\phi'') \cdot \overline{\overline{E}}_n \cdot \overline{\overline{D}}_n(-\beta_n(\theta'',\phi'')\sec\theta''(z'+d_n)) \\
&\quad \cdot \overline{\overline{E}}_n^{-1} \cdot \prod_{i=n+1}^{N} (\overline{\overline{E}}_i \cdot \overline{\overline{D}}_i(-\beta_i(\theta'',\phi'')\sec\theta'' h_i)\overline{\overline{E}}_i^{-1}) \\
&\quad \overline{\overline{R}}(\theta'',\phi'';\theta_0,\phi_0) \cdot \prod_{i=N}^{1} (\overline{\overline{E}}_i \cdot \overline{\overline{D}}_i(\beta_i(\pi-\theta_0,\phi_0)\sec\theta_0 h_i)\overline{\overline{E}}_i^{-1})\bar{I}_0
\end{aligned}
\tag{26a}
$$

$$\bar{I}^{(1)}_{n,2}(\theta,\phi,-d_{n-1}) = \sec\theta\bar{\bar{E}}_n \int_{-d_n}^{-d_{n-1}} dz'\bar{\bar{D}}_n(\beta_n(\theta,\phi)\sec\theta(z'+d_{n-1}))\cdot\bar{\bar{E}}_n^{-1}$$
$$\cdot P_n(\theta,\phi;\pi-\theta_0,\phi_0)\cdot(\bar{\bar{E}}_n\cdot\bar{\bar{D}}_n(\beta_n(\pi-\theta_0,\phi_0)\sec\theta_0(z'+d_{n-1}))\cdot\bar{\bar{E}}_n^{-1})$$
$$\cdot\prod_{i=n-1}^{1}(\bar{\bar{E}}_i\cdot\bar{\bar{D}}_i(\beta_i(\pi-\theta_0,\phi_0)\sec\theta_0 h_i)\cdot\bar{\bar{E}}_i^{-1})\cdot\bar{I}_0$$
$$+\sec\theta\bar{\bar{E}}_n\int_{-d_n}^{-d_{n-1}}dz'\bar{\bar{D}}_n(\beta_n(\theta,\phi)\sec\theta(z'+d_{n-1}))\cdot\bar{\bar{E}}_n^{-1}$$
$$\cdot\int d\Omega' P_n(\theta,\phi;\theta',\phi')\cdot(\bar{\bar{E}}_n\cdot\bar{\bar{D}}_n(-\beta_n(\theta',\phi')\sec\theta'(z'+d_n))\cdot E_n^{-1})$$
$$\cdot\prod_{i=n+1}^{N}(\bar{\bar{E}}_i\cdot\bar{\bar{D}}_i(-\beta_i(\theta',\phi')\sec\theta' h_i)\bar{\bar{E}}_i^{-1})$$
$$\cdot\bar{\bar{R}}(\theta',\phi';\theta_0,\phi_0)\cdot\prod_{i=N}^{1}(\bar{\bar{E}}_i\cdot\bar{\bar{D}}_i(\beta_i(\pi-\theta_0,\phi_0)\sec\theta_0 h_i)\bar{\bar{E}}_i^{-1})\cdot\bar{I}_0 \tag{26b}$$

The integration of $\bar{\bar{D}}$ along the $\hat{z}$ direction in (26) can be carried out analytically. The final result for the first-order solution is

$$
\begin{aligned}
&\bar{I}_n^{(1)}(\theta,\phi,z=-d_{n-1}) = \\
&\quad \sec\theta[\bar{\bar{E}}_n]\cdot[\bar{\bar{E}}_n^{-1}P_n(\theta,\phi;\pi-\theta_0,\phi_0)\bar{\bar{E}}_n]_{km}\frac{1-e^{-\beta_k(\theta,\phi)\sec\theta h_n-\beta_m(\pi-\theta_0,\phi_0)\sec\theta_0 h_n}}{\beta_k(\theta,\phi)\sec\theta+\beta_m(\pi-\theta_0,\phi_0)\sec\theta_0} \\
&\quad \cdot[\bar{\bar{E}}_n^{-1}]_{mj}\cdot\prod_{i=n-1}^{1}(\bar{\bar{E}}_i\cdot\bar{\bar{D}}_i(\beta_i(\pi-\theta_0,\phi_0)\sec\theta_0 h_i)\cdot\bar{\bar{E}}_i^{-1})\cdot\bar{I}_0 \\
&+\sec\theta[\bar{\bar{E}}_n]\cdot\int_0^{2\pi}d\phi'\int_0^{\frac{\pi}{2}}d\theta'\sin\theta'[\bar{\bar{E}}_n^{-1}P_n(\theta,\phi;\theta',\phi')\bar{\bar{E}}_n]_{km}\frac{e^{-\beta_k(\theta,\phi)\sec\theta h_n}-e^{-\beta_m(\theta',\phi')\sec\theta' h_n}}{\beta_m(\theta',\phi')\sec\theta'-\beta_k(\theta,\phi)\sec\theta} \\
&\quad \cdot\prod_{i=n+1}^{N}(\bar{\bar{E}}_i\cdot\bar{\bar{D}}_i(-\beta_i(\theta',\phi')\sec\theta' h_i)\bar{\bar{E}}_i^{-1})\cdot[E_n^{-1}\bar{\bar{R}}(\theta',\phi';\theta_0,\phi_0)]_{mj} \\
&\quad \prod_{i=N}^{1}(\bar{\bar{E}}_i\cdot\bar{\bar{D}}_i(\beta_i(\pi-\theta_0,\phi_0)\sec\theta_0 h_i)\bar{\bar{E}}_i^{-1})\cdot\bar{I}_0 \\
&+\prod_{i=n+1}^{N}(\bar{\bar{E}}_i\cdot\bar{\bar{D}}_i(-\beta_i(\theta,\phi)\sec\theta h_i)\bar{\bar{E}}_i^{-1})\cdot\int_0^{2\pi}d\phi'\int_0^{\frac{\pi}{2}}d\theta'\tan\theta'\bar{\bar{E}}_n \\
&\quad \bar{\bar{D}}_n(-\beta_n(\theta,\phi)\sec\theta h_n)\bar{\bar{E}}_n^{-1}\bar{\bar{R}}(\theta,\phi;\theta',\phi')\prod_{i=N}^{n+1}(\bar{\bar{E}}_i\cdot\bar{\bar{D}}_i(-\beta_i(\pi-\theta',\phi')\sec\theta' h_i)\bar{\bar{E}}_i^{-1}) \\
&\quad [\bar{\bar{E}}_n\bar{\bar{P}}_n(\pi-\theta',\phi';\pi-\theta_0,\phi_0)\bar{\bar{E}}_n]_{km}\frac{e^{-\beta_k(\pi-\theta',\phi')\sec\theta' h_n}-e^{-\beta_m(\pi-\theta_0,\phi_0)\sec\theta_0 h_n}}{\beta_m(\pi-\theta_0,\phi')\sec\theta_0-\beta_k(\pi-\theta',\phi')\sec\theta'}[\bar{\bar{E}}_n^{-1}]_{mj} \\
&\quad \cdot\prod_{i=n-1}^{1}(\bar{\bar{E}}_i\bar{\bar{D}}_i(\beta_i(\pi-\theta_0,\phi_0)\sec\theta_0 h_i)\cdot E_i^{-1})\cdot\bar{I}_0 \\
&+\prod_{i=n+1}^{N}(\bar{\bar{E}}_i\cdot\bar{\bar{D}}_i(-\beta_i(\theta,\phi)\sec\theta h_i)\bar{\bar{E}}_i^{-1})\cdot\int_0^{2\pi}d\phi'\int_0^{\frac{\pi}{2}}d\theta'\tan\theta'\bar{\bar{E}}_n\cdot \\
&\quad \bar{\bar{D}}_n(-\beta_n(\theta,\phi)\sec\theta h_n)\bar{\bar{E}}_n^{-1}\bar{\bar{R}}(\theta,\phi;\theta',\phi')\bar{\bar{E}}_n(\pi-\theta',\phi') \\
&\quad \prod_{i=N}^{n+1}(\bar{\bar{E}}_i\cdot\bar{\bar{D}}_i(-\beta_i(\pi-\theta',\phi')\sec\theta' h_i)\bar{\bar{E}}_i^{-1})\int_0^{2\pi}d\phi''\int_0^{\frac{\pi}{2}}d\theta''sin\theta''[\bar{\bar{E}}_n^{-1}\bar{\bar{P}}_n(\pi-\theta',\phi';\theta'',\phi'')\bar{\bar{E}}_n]_{km} \\
&\quad \frac{1-e^{-\beta_k(\pi-\theta',\phi')\sec\theta' h_n-\beta_m(\theta'',\phi'')\sec\theta'' h_n}}{\beta_k(\pi-\theta',\phi')\sec\theta'+\beta_m(\theta'',\phi'')\sec\theta''}\cdot\prod_{i=n+1}^{N}(\bar{\bar{E}}_i\cdot\bar{\bar{D}}_i(-\beta_i(\theta'',\phi'')\sec\theta'' h_i)\bar{\bar{E}}_i^{-1}) \\
&\quad \cdot[\bar{\bar{E}}_n^{-1}\cdot\bar{\bar{R}}(\theta'',\phi'';\theta_0,\phi_0)]_{mj}\cdot\prod_{i=N}^{1}(\bar{\bar{E}}_i\cdot\bar{\bar{D}}_i(\beta_i(\pi-\theta_0,\phi_0)\sec\theta_0 h_i)\bar{\bar{E}}_i^{-1})\bar{I}_0
\end{aligned}
\tag{27}
$$

The first term in the above equation represents the single volume scattering contribution, the second and third terms represent the interaction between surface and volume scattering, and the last term represents two surface scattering and one volume scattering as shown in Figure 2.

To obtain $\overline{I}^{(1)}(\theta,\phi,0)$ for a N-layer medium, we simply sum up the contribution from each layer and take into account the attenuation through upper layers.

$$\overline{I}^{(1)}(\theta,\phi,0)=\sum_{n=1}^{N}\prod_{i=n-1}^{1}(\overline{\overline{E}}_i\cdot\overline{\overline{D}}_i\cdot\overline{\overline{E}}_i^{-1})\cdot\overline{I}_n^{(1)}(\theta,\phi,-d_{n-1}) \tag{28}$$

2.2.2 Second Order Solution with Long Cylinder Approximation

Follow the same scheme, the second order iterative solution of the RT equation can be easily obtained. The solution involves the double integral representing the double scattering from one scattering direction to another. In forests, the trunks constitute a large portion of total biomass and due to the long structures, the second order scattering between the trunks and other components of the foliage will be considered to assess the higher order scattering effect.

Using the finite cylinder approximation where the induced current on the cylinder is the same as the one on an infinite long cylinder, the scattering function can be expressed as

$$S_{\alpha\beta}(\hat{k}',\hat{k}_i)=S_{0\alpha\beta}(\hat{k}',\hat{k}_i)\int_{-d/2}^{d/2}dz\;e^{-ik_0(\cos\theta'-\cos\theta_i)z} \tag{29}$$

where d is the length of the cylinder, k_0 is the wave number in the free space, $\hat{k}_i$ and $\hat{k}'$ are the incident and scattering directions for a trunk, respectively, θ_i and θ' are the incident angle and scattering angles, α and β are scattered and incident

polarizations and can be either h or v polarization. The phase matrix elements which are the correlation between different scattering matrix elements can be expressed as

$$P_{\alpha\beta\gamma\delta}(\hat{k}', \hat{k}_i) = S_{0\alpha\beta}(\hat{k}', \hat{k}_i) \cdot S^*_{0\gamma\delta}(\hat{k}', \hat{k}_i) \frac{\sin^2[(\frac{k_0 d}{2})(\cos\theta' - \cos\theta_i)]}{[(\frac{k_0 d}{2})(\cos\theta' - \cos\theta_i)]^2} \cdot d^2 \tag{30}$$

where α, β, γ, δ can be either h or v polarization.

If $k_0 d$ is large as the case of tree trunks at microwave frequencies, the scattering from trunks $P(\hat{k}', \hat{k}_i)$ is peaked at $\theta' = \theta_i$. Assuming that the scattering from other components $P_1(\hat{k}', \hat{k}_i)$ is slowly varying compared with the scattering from trunks, the double scattering term in the second order solution of RT equation is in terms of

$$\begin{aligned} &\int_0^{2\pi} d\phi' \int_0^{\pi} d\theta' \sin\theta' P_1(\hat{k}_s, \hat{k}') \cdot P(\hat{k}', \hat{k}_i) \\ &\qquad = \int_0^{2\pi} d\phi' P_1(\hat{k}_s, \hat{k}') \cdot S_{0\alpha\beta}(\hat{k}', \hat{k}_i) S_{0\gamma\delta}(\hat{k}', \hat{k}_i)^* \mid_{\theta'=\theta_i} \\ &\qquad \cdot d^2 \int_0^{\pi} d\theta' \sin\theta' \frac{\sin^2[(\frac{k_0 d}{2})(\cos\theta' - \cos\theta_i)]}{[(\frac{k_0 d}{2})(\cos\theta' - \cos\theta_i)]^2} \end{aligned} \tag{31}$$

and in the limit of $k_0 d \to \infty$,

$$\int_0^{\pi} d\theta' \sin\theta' \frac{\sin^2[(\frac{k_0 d}{2})(\cos\theta' - \cos\theta_i)]}{[(\frac{k_0 d}{2})(\cos\theta' - \cos\theta_i)]^2} = \frac{2}{k_0 d} \cdot \pi \tag{32}$$

The remaining integration over ϕ' can be carried numerically.

The effect of the double scattering is illustrated with a simple tree structure with only trunks and branches as shown in Figure 3. The tree trunk has a radius of $4.0cm$ and length $5.0m$. There are 50 branches attached to the the upper $2m$ of each trunk. The radius and length of branches are $1.0cm$ and $0.5m$ respectively. The fractional volume of crown layer is 0.1% The HH and HV backscattering coefficients as functions of incident angles are shown in Figures 4(a) and 4(b) in which the 1st-order and 2nd-order denote the RT solutions of first order and second order with long

cylinder approximation. It is shown that the second-order scattering has little effect on co-polarized backscattering coefficients although there is about 0.5 dB difference for the cross-polarized backscattering coefficient. As the fractional volume increases to 0.2% the effect becomes larger as shown in Figure 5.

2.3 SCATTERING FUNCTION FOR CLUSTERED STRUCTURES

The Radiative Transfer theory has been widely used for the remote sensing of earth terrain because of its simple formulation. The important task is the accurate calculation of the phase matrix and extinction matrix. In order to account for the multi-frequency response, accurate terrain geometries need to be included. Beside the multi-scale sizes of the forest scatterers, the structure effect would also affect the frequency response. In this Section, two structure effects are studied. One is the clustering structure of branches which has smaller scale scatterers attached to the larger scale scatterers such as branches attached to the trunk. Another is the clustering effect of scatterers close to each other and form a larger scale scatterers with different shapes.

2.3.1 Cluster Effect of Branching Structure

In order to account for the coherent scattering effect due to clustered vegetation structures in the radiative transfer theory, the phase matrix based on the branching model of vegetation needs to be formulated. In pine forest, most of the scatterers are of cylindrical shape. Hence the main subject in this section is the clusters consisting of multiple cylinders. For a cylinder cluster that has one center cylinder and N branching cylinders as shown in Figure 1(b), the total backscattering function $f_{\alpha\beta}$ is

$$f_{\alpha\beta} = f_{0\alpha\beta} + \sum_{n=1}^{N} f_{n\alpha\beta}\, e^{i\phi_n} \tag{33}$$

where $f_{0\alpha\beta}$ is the $\alpha\beta$-th element of the scattering matrix for the center cylinder, and $f_{n\alpha\beta}$ is $\alpha\beta$-th element of the scattering matrix for the n-th branching cylinder. $\alpha, \beta, \gamma, \delta$ represent horizontal or vertical polarizations.

Assuming all the branching cylinders are identical and independent of each other, and their relative positions are independent of their sizes and orientations, the correlation of f is given by

$$\begin{aligned}\langle f_{\alpha\beta} f^*_{\gamma\delta}\rangle &= \langle f_{0\alpha\beta} f^*_{0\gamma\delta}\rangle + N\langle f_{n\alpha\beta} f^*_{n\gamma\delta}\rangle \\ &\quad + 2N\,\mathrm{Re}\left[\langle f_{0\alpha\beta}\rangle\langle f^*_{n\gamma\delta}\rangle\langle e^{-i\phi_n}\rangle\right] \\ &\quad + N(N-1)\langle f_{m\alpha\beta}\rangle\langle f^*_{n\gamma\delta}\rangle\langle e^{i\phi_m}\rangle\langle e^{-i\phi_n}\rangle \end{aligned} \tag{34}$$

The relative phase of the n-th branch with respect to the center cylinder is defined as

$$\phi_n = (\overline{k}_i - \overline{k}_s)\cdot\overline{r}_n$$

where $\overline{k}_i$ and $\overline{k}_s$ are the incident and scattered wave vectors, respectively. $\overline{r}_n$ is the location of the n-th branching cylinder relative to the center cylinder.

In (34), the third and fourth terms are the coherent scattering terms. It can be seen that the incoherent scattering approximation is valid when the average of the random phase factor $\langle e^{i\phi_j}\rangle$ is small such that the coherent terms are negligible compared to the incoherent terms. However, this is not true for vegetation structures with scale lengths comparable to the wavelength, as demonstrated with a two-scale cluster [Yueh et al., 1992].

In the calculation of scattered fields from different cluster elements, dielectric cylinders can be used to model trunks, branches, and coniferous leaves [Karam et al., 1988; Durden et al., 1989]. Leaves of deciduous tree can be modelled as disks [Karam et al., 1988; Lang and Saleh, 1985]. The truncated infinite cylinder approximation [Van de Hulst, 1957] is employed to calculate scattered fields from cylinders.

2.3.2 Effect of Leaves Structure

For the vegetation, the leave shape is complicated and there may be several pieces of leaves connected on the same twigs. However, due to the complexity of scattering function for the scatterers with arbitrary shapes, circular cylinders and disks are usually used to model the coniferous and deciduous leaves [Karam, et al., 1988]. The common practice is to use the simple shape scatterers of the same volume. However, the appropriate approximation may depend on the wavelength.

A typical pine tree needle structure is consisted of two to five cylinders connected together as shown in Figure 6. Since the needles are close to each other and the multiple scattering and coherent interaction would be important. If the first order scattering function is used, the correlation of scattering function can be formulated similar to the last Section as

$$S = \sum_{m=1}^{N} S_m(\alpha_m, \beta_m, \gamma_m) \tag{35}$$

$$\begin{aligned} \langle |S|^2 \rangle = & \sum_{m=1}^{N} \langle |S_m(\alpha_m, \beta_m, \gamma_m)|^2 \rangle \\ & + \sum_{m_1=1}^{N} \sum_{m_2=1_{m_2 \neq m_1}}^{N} \langle S_{m_1}(\alpha_{m_1}, \beta_{m_1}, \gamma_{m_1}) S^*_{m_2}(\alpha_{m_2}, \beta_{m_2}, \gamma_{m_2}) \rangle \end{aligned} \tag{36}$$

where α, β and γ represent the Eulerian angles of rotation.

The effect of the leaves structure is illustrated with the simulation of backscattering coefficients from a half-space random medium with randomly distributed needle-shaped scatterers. The incident angle is 45° and the frequency range is from 1 GHz to 10 GHz. The separation angle between two needles is 5°. The radius and length

of needles are 0.6mm and 15cm, respectively. The dielectric constant of leaves is (20.2,6.4). As shown in Figure 7, at lower frequencies, the scattering from two needles approaches the scattering from one larger needle with equivalent volume of two needles and at higher frequencies, it is scattered like independent scattering.

2.3.3 Modification to Phase Matrix and Extinction Matrix

Phase matrix is defined in terms of the correlation of scattering function elements which is readily obtained from the previous Section where the average of the field correlation is calculated with clustering effect of scatterers included.

As for the extinction, it is the sum of absorption loss and scattering loss and also can be expressed as in terms of imaginary part of forward scattering function based on the optical theorem. The modification of the scattering function with clustering model should result the modification of extinction to ensure the energy conservation. From this energy conservation criterion, the imaginary part of the scattering function can be expressed as follow [Tsang et al., 1992]

$$\frac{4\pi}{k} Im[f_{vv}(\hat{s},\hat{s})] = \kappa_{av}(\hat{s}) + \int_{4\pi} d\Omega' [|f_{vv}(\hat{s}',\hat{s})|^2 + |f_{hv}(\hat{s}',\hat{s})|^2] \tag{37a}$$

$$\frac{4\pi}{k} Im[f_{hh}(\hat{s},\hat{s})] = \kappa_{ah}(\hat{s}) + \int_{4\pi} d\Omega' [|f_{hh}(\hat{s}',\hat{s})|^2 + |f_{vh}(\hat{s}',\hat{s})|^2] \tag{37b}$$

$$\begin{aligned} \frac{4\pi}{k} Im[f_{hv}(\hat{s},\hat{s})] &= \frac{4\pi}{k} Im[f_{vh}(\hat{s},\hat{s})] \\ &= \frac{1}{2}[\kappa_{ah}(\hat{s}) + \kappa_{av}(\hat{s})] \\ &\quad + \frac{1}{2}\int_{4\pi} d\Omega' [|f_{vv}(\hat{s}',\hat{s}) + f_{vh}(\hat{s}',\hat{s})|^2 + |f_{hv}(\hat{s}',\hat{s}) + f_{hh}(\hat{s}',\hat{s})|^2] \\ &\quad - \frac{2\pi}{k}\{Im[f_{hh}(\hat{s},\hat{s}) + Im[f_{vv}(\hat{s},\hat{s})]\} \end{aligned} \tag{37c}$$

where $\kappa_{a\beta}$ is the absorption loss of β polarization.

Usually the forward scattering function has small imaginary part to satisfy the optical theorem. Problems may occur when the approximation to the scattering function is used. Even when the approximation is valid for a single scatterer, the energy may still not conserve when the coherent scattering effect is included in the phase matrix only but not the extinction matrix. To resolve the problem caused by the clustering structure, the average imaginary part of the forward scattering function need to be changed as follow

$$\frac{4\pi}{k} Im[\langle f_{vv}(\hat{s},\hat{s})\rangle] = \langle \kappa_{av}(\hat{s})\rangle + \int_{4\pi} d\Omega' [\langle |f_{vv}(\hat{s}',\hat{s})|^2\rangle + \langle |f_{hv}(\hat{s}',\hat{s})|^2\rangle] \tag{38a}$$

$$\frac{4\pi}{k} Im[\langle f_{hh}(\hat{s},\hat{s})\rangle] = \langle \kappa_{ah}(\hat{s})\rangle + \int_{4\pi} d\Omega' [\langle |f_{hh}(\hat{s}',\hat{s})|^2\rangle + \langle |f_{vh}(\hat{s}',\hat{s})|^2\rangle] \tag{38b}$$

$$\begin{aligned}
&\frac{4\pi}{k} Im[\langle f_{hv}(\hat{s},\hat{s})\rangle] = \frac{4\pi}{k} Im[\langle f_{vh}(\hat{s},\hat{s})\rangle] \\
&= \frac{1}{2}[\langle \kappa_{ah}(\hat{s}) + \kappa_{av}(\hat{s})\rangle] \\
&\quad + \frac{1}{2}\int_{4\pi} d\Omega' [\langle |f_{vv}(\hat{s}',\hat{s}) + f_{vh}(\hat{s}',\hat{s})|^2\rangle + \langle |f_{hv}(\hat{s}',\hat{s}) + f_{hh}(\hat{s}',\hat{s})|^2\rangle] \\
&\quad - \frac{2\pi}{k}\{Im[\langle f_{hh}(\hat{s},\hat{s})\rangle] + Im[\langle f_{vv}(\hat{s},\hat{s})\rangle]\}
\end{aligned} \tag{38c}$$

where $\langle\rangle$ is the ensemble average. $\langle f_{\alpha\beta} f^*_{\beta\gamma}\rangle$ is the average correlation of scattering function with coherent clustering effect taken into account. $\kappa_{a\beta}$ is the absorption loss of β polarization which can be obtained by integrating the internal field of the scatterers or by subtracting the scattering loss from the total extinction with the use of the optical theorem.

The coherent clustering effect is illustrated with the backscattering from a layer of forest as shown in Figure 3. The fractional volume in the crown layer is 0.1%. Figure 8 shows the effect of coherent scattering and extinction correction to the HH and HV polarizations. It is found that the coherent effect is more significant for co-polarized

backscattering coefficient while the extinction correction has more effect at higher incident angles. It also shows that the modified extinction affect HH backscattering return more than HV return. This is because that the main scattering mechanism is from the tree and ground interaction which is more sensitive to attenuation.

2.4 COMPARISON WITH EXPERIMENTAL DATA

The Landes forest in South-Western France is the major test site for several airborne SAR campaigns such as Maestro-1 and MacEurope. It is also one of the test sites for Shuttle Imaging Radar-C and X-band SAR (SIR-C/XSAR) mission. It is the largest plantation forest in France which constitutes nearly one million hectares and produces 20% of the French timber. The main species in this forest is maritime pine (*pinus pinaster*). Since this forest is managed for the production of timber, there are large statistically homogeneous stand of trees with the same age which is easy to collect ground truth for the validation and simulation of theoretical model.

To model the pine forest, the RT model described in previous Sections is applied to a configuration shown in Figure 1. The top layer (region 1) consists of vertically orientated three-scale dielectric cylinder clusters characterizing trunks and branches. The branching clusters include primary and secondary branches, as well as needles. In the four-scale model, all the smaller scale cylinders are uniformly located along a larger scale center cylinder and the angular distribution in the azimuthal direction is uniform from -180° to 180°. The primary branch angle β_1 is uniformly distributed between 50° and 70° and the secondary branches angle β_2 is 70° and needles angle β_3 is 70°. Region 2 contains only tree trunks whose orientation is uniformly distributed between 0° and 10°. In region 3, nearly vertical orientated cylinders coexisted with randomly oriented thin cylinders characterizing a mixture of the tree trunks and short vegetation in the forest understory. The underlying ground has rms height $1.2cm$ and correlation length $6.0cm$

In preparation for the flight of the Spaceborne Imaging Radar-C (SIR-C) of April

and October 1994, two previous airborne experiment campaigns have been carried out on the Landes Forest test site with the use of NASA/JPL three-frequency polarimetric AIRSAR system operating at P band (0.44 GHz), L band (1.25 GHz) and C band (5.3 GHz). In addition, spaceborne SAR data acquired by ERS-1 (C band, VV polarization, 23° of incidence) and JERS-1 (L band, HH polarization, 35° of incidence) satellites in 1992 were also available.

2.4.1 MAESTRO-1 Experiment

The MAESTRO-1 campaign was conducted by the Centre d'Etude Spatiale BIOsphere (CESBIO) and the Jet Propulsion Laboratory (JPL) in August 1989 at the Landes forest in southwest France. During the experiment, the NASA/JPL synthetic aperture radar (SAR) was used to monitor the radar responses of the maritime pine trees in the forest. A strong correlation between P-band (0.44 GHz) backscattering coefficients and pine forest physical parameters has been observed in the measurement data [Le Toan et al., 1992]. The measurement data demonstrated potential use of SAR for monitoring forest parameters.

With this model, the backscattering coefficients are calculated for six selected pine stands of different ages. The age classes of the forest under investigation are 3, 8, 13, 20, 30, 38, and 46 years old, respectively. The average radius of tree trunks and the average tree height increase with age. The primary and secondary branches grow as well. In general, the above-ground biomass increases despite the decrease in the number of trees per unit area with age. The model input parameters is derived from measured and estimated forest data [Beaudoin et al., 1992]. Table 1 shows the input parameters of crown and trunk layers used in this calculation. The radius and

length of needle are $0.7mm$ and $15cm$, respectively. The density of needle is 450 per meter of secondary branch. Understory vegetation inside the forest is modelled as a 1-meter thick layer with randomly orientated cylinder to represent the short vegetation twigs. The radius and length of the cylinders are 0.04cm and 10cm, respectively. The fractional volume is 0.1%. The dielectric constant is calculated with a measured gravimetric moisture content of 55 % using a dielectric model [Ulaby and El-Rayes, 1987]. The rms height and correlation length of rough soil surface is 1.2 cm and 6.0 cm, respectively. The dielectric constant of soil is calculated from the soil moisture of 20 % using a empirical soil dielectric model [Hallikainen, et al., 1985].

The simulated results for P-band are shown in Figure 9. The discrete points are the mean backscattering coefficients retrieved from large forest stands in the calibrated SAR image in the range of incident angles between 40° to 50°; the curves are the theoretical results calculated at 45° incident angle. From the simulation results, it is found that the two major contributions to the HH returns at P-band are the trunk–ground double scattering and direct crown backscattering. As the forest grows older, the trunks are getting bigger and taller, hence the trunk–ground scattering effect increases. Therefore, as shown in Figure 10(a), the HH returns appear to be dominated by the trunk–ground scattering for older forests. However, for young forests, it is mainly from crown–ground interaction. The VV returns mainly come from the crown scattering for older forests, and for young forests, both the crown–ground interaction and direct crown scattering contribute as shown in Figure 10(b). As for the HV returns it is clear from Figure 10(c) that the main contribution to the backscattering coefficients comes from the direct scattering by the crown layer. When the forest grows older, the primary branches get bigger and the HV returns increase in spite of the decrease in the tree density. From the theoretical simulation, the

results explain the increase of HH, VV, and HV returns with forest age for different reasons. This leads to different dynamic range of radar returns for the same range of forest age. The variation in the measurement data for a given forest biomass can be attributed to the fact that the radar returns are linked to trunk (for HH returns) and crown (for HV and VV returns) biomasses, but not directly to the total biomass.

The results for L-band and C-band backscattering coefficients are shown in Figures 11 and 12. It is found that backscattering coefficients at C-band is almost flat because the main scatterers at this frequency is needles and small branches which are similar for all ages. As for L-band, co-polarization return is almost flat while there is an increasing trend for the cross-polarized backscattering coefficient. However, it is saturated at about 60 $tons/ha$. The contribution of scattering mechanisms for L-band HH backscattering is shown in Figure 13. It is found that the main backscattering mechanism is direct crown scattering and ground bounce term. As for VV and HV backscattering, the main scattering mechanism is direct crown return. For the case of C-band, it is found that the main scattering mechanism for all polarizations is direct crown scattering. From further analysis of the scattering contribution, the main scatterers for C-band is from clustering of small branches and needles.

2.4.1 SIR-C/XSAR Experiment

SIR-C/XSAR is the first multi-frequency, and fully polarimetric SAR system on space. It provides wide coverage of earth terrain and accurate account of incident angle which has very stable response. The frequencies used are L-, C-, and X-band. The incident angle over the Landes forest on the first mission is $26°$. Since from the MAESTRO-1 experiment, it is found that the L-band backscattering coefficients

saturate at low biomasses, additional effort is made to survey the test sites with trees under 8 years old. The soil moisture content and tree moisture content are 20 % and 65 %, respectively.

Figures 14 and 15 display experimental and theoretical backscattering coefficients σ^0_{hh}, σ^0_{vv} and σ^0_{hv} for both forest stands and clear-cut areas at L band and C band respectively. Clear-cut areas where short vegetation presented are corresponding to a biomass of 4 tons/ha. In the case of L band, the copolarized backscatter is fairly constant as a function of forest biomass which is consisted with the MAESTRO-1 experiment. For L band HV, the increase of backscatter responses as a function of forest biomass is noticeable. Theoretical simulation shows the same trend. Nevertheless, for forest stands with biomass higher than 40 tons/ha, the backscatter response reaches saturation. The dynamic range in σ^0_{hv} measurement from clear-cut to old forest is about 5 dB. In the C band case, we observe a decreasing trend of co-polarized return when forest biomass is increasing from 8 tons/ha to 40 tons/ha. From the theoretical simulation, it is found that for young forest stand, the scattering from soil rough surface is very strong because the near normal incident angle. However, as the forest grows older, the attenuation increases and thus the backscattering decrease. The soil contribution does not show up at L-band since at lower frequencies backscattering from soil is not significantly higher than the backscattering from vegetation. Its effect on the cross-polarized backscattering is also negligible.

In addition to the study of conventional backscattering coefficients, the normalized correlation coefficient between HH and VV polarizations, ρ, is also investigated. Figures 16 and Figure 17 represent the experimental and theoretical variations of ρ coefficient for both forest stands and clear-cut areas at L band and C band respectively. For bare soil, the correlation coefficient is close to 1 according to the

experiment and theoretical simulation using Kirchhoff's approximation or Small Perturbation Model. When the electromagnetic wave does not penetrate to the ground, the magnitude of ρ drops to a value of 0.35 for older stands.

Figure 18 shows the measured and simulated backscattering coefficients at X-band. The continuous curves are the theoretical simulation for VV polarization and the symbol is the measured data. It is found that the scattering from X-band is mainly from needles. This indicates that the X-band backscattering could be used to discriminate different types of vegetation according to their leaves structures.

Figures 19 shows the coherent effect of needles and branches at C-band for HH and HV polarizations. It is found that the independent scattering from individual tree components can not explain the backscattering return and the whole structure of branches and needles have to be considered.

2.5 DISCUSSION AND CONCLUSION

The radiative transfer theory is applied to the modeling of polarimetric radar backscatter from pine forest. Comparing with the traditional radiative transfer formulation, the phase matrix and extinction matrix used here is calculated by considering the structure of the forest components. It is found that the clustering effect of branches is important for the low frequency case while the needle structure is important at higher frequencies. The coherent effect on the extinction is also investigated. The theoretical simulation is compared with the multi-frequency, polarimetric backscattering data obtained from NASA/JPL AIRSAR and SIR-C/XSAR missions.

From the analysis of the measurement data and the theoretical simulation with measured ground truth, it is found that the cross-polarized returns at lower frequencies such as P-, and L-bands are sensitive to the forest biomass. The use of cross-polarized return for biomass monitoring has been demonstrated in Figure 20 where the biomass maps of 1989 and 1994 are compared. It shows that the younger forests grow older and trees at some old forests have been cut down to become clear-cut or regrowth forests. The correlation coefficient of HH and VV polarization ρ can be used to separate the volume scattering return such as the backscattering from forest and surface scattering return such as backscattering from soil. At low incident angles, ρ can also be used to retrieve biomass but the result is sensitive to the soil condition. The fine structure of leaves is found to have impact on the scattering characteristics at higher frequencies such as C- and X-band. The frequency dependence of the leaves structure can be used to separate different species of trees.

Comparing the SIR-C data with the MAESTRO-1 measurement, it is found that

the backscattering from forest is very complicated and it is dependent on the system parameters such as frequency, incident angle as well as the environmental conditions such as the soil moisture and plant moisture content. The developed theoretical models can be used to investigate the dependence of experimental observations on forest physical parameters and to construct the retrieval algorithms for interested parameters such as biomass.

	crown boles		primary branches			secondary branches		
age	radius (cm)	length (m)	radius (cm)	length (m)	density (m^{-1})	radius (cm)	length (m)	density (m^{-1})
3	1.56	1.16	0.48	0.61	13.0	0.15	0.18	7.0
8	3.80	5.10	0.70	1.23	7.60	0.41	0.41	7.0
14	4.10	5.62	0.90	1.40	7.12	0.44	0.44	7.0
22	4.50	6.19	1.10	1.69	6.46	0.48	0.48	7.0
30	4.80	6.62	1.20	1.99	6.05	0.52	0.52	7.0
38	4.93	7.0	1.36	2.25	5.75	0.56	0.56	7.0
46	5.10	7.25	1.55	2.49	5.50	0.60	0.60	7.0

Table 1 Table of the Landes forest parameters in crown layer

age	density (m^{-2})	radius (cm)	length (m)
3	0.40	1.56	1.16
8	0.103	3.80	5.10
14	0.084	4.10	5.62
22	0.061	4.50	6.19
30	0.045	4.80	6.62
38	0.033	4.93	7.0
46	0.024	5.10	7.25

Table 2 Table of the Landes forest parameters in trunk layer

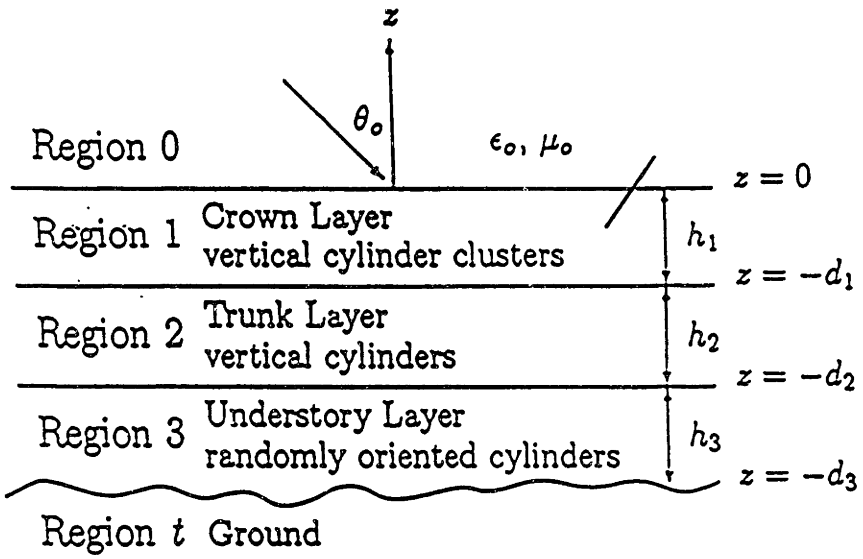

Figure 1 (a) Four layer Forest Model

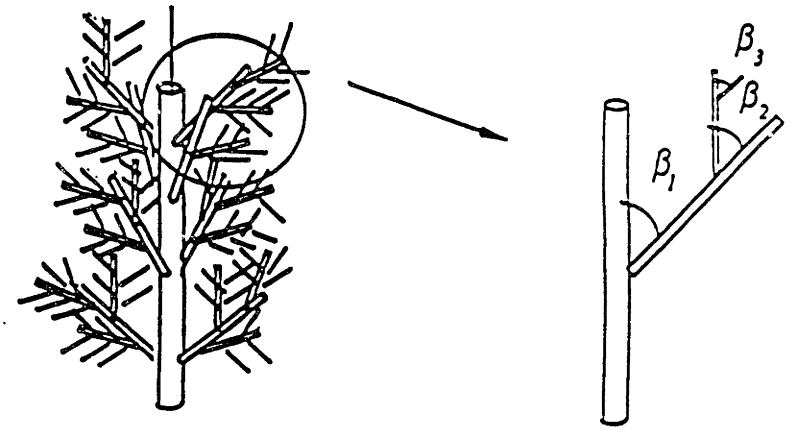

Figure 1 (b) Tree Crown Cluster Model

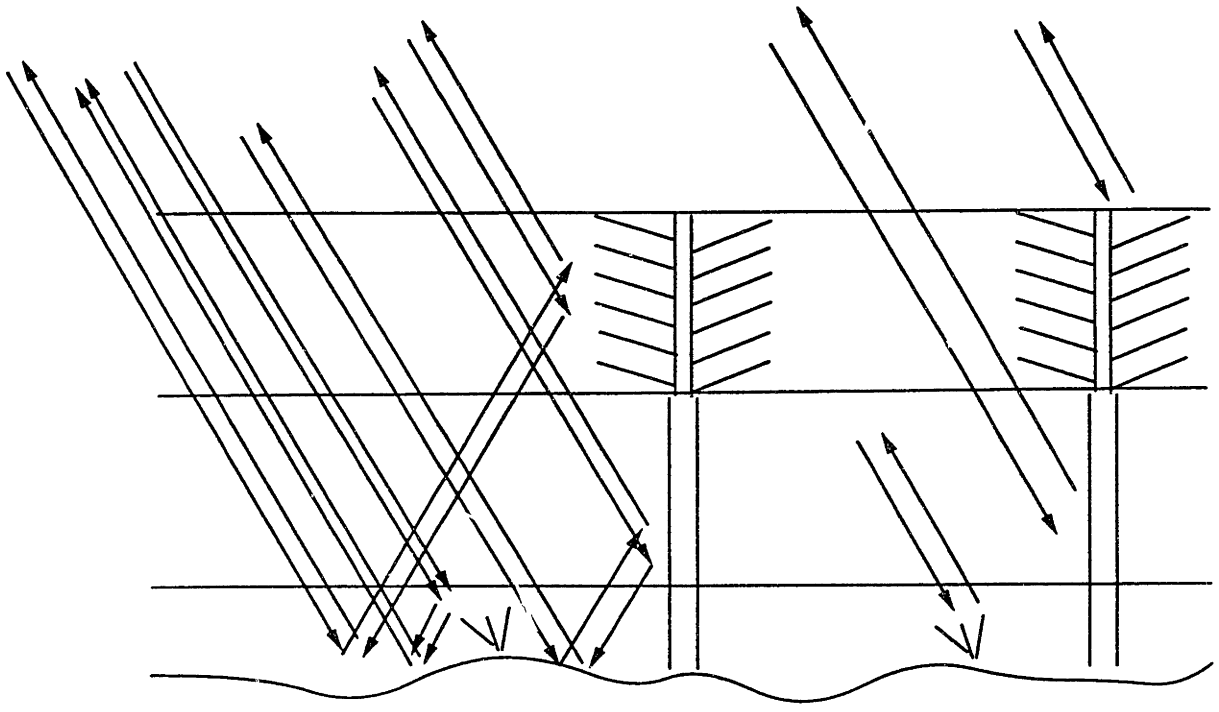

Figure 2 Scattering Mechanisms

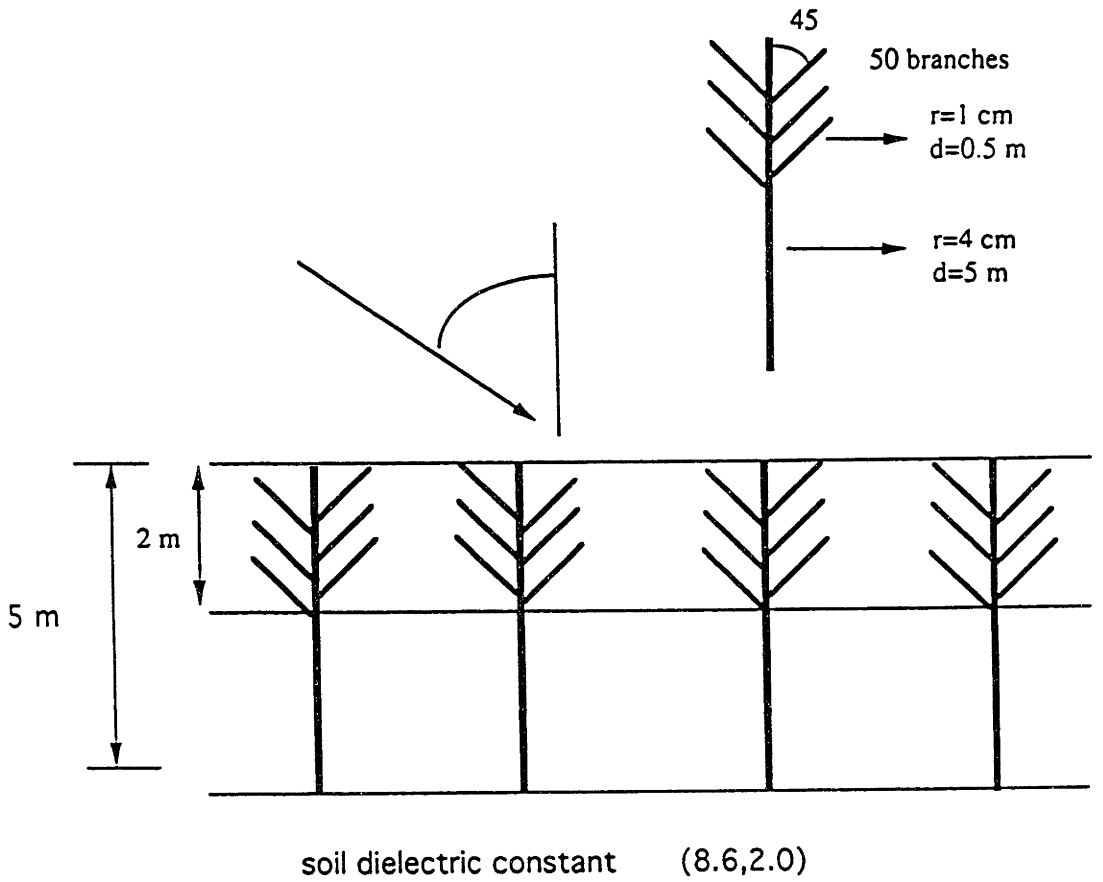

Figure 3 Simple Two-scale Tree Model

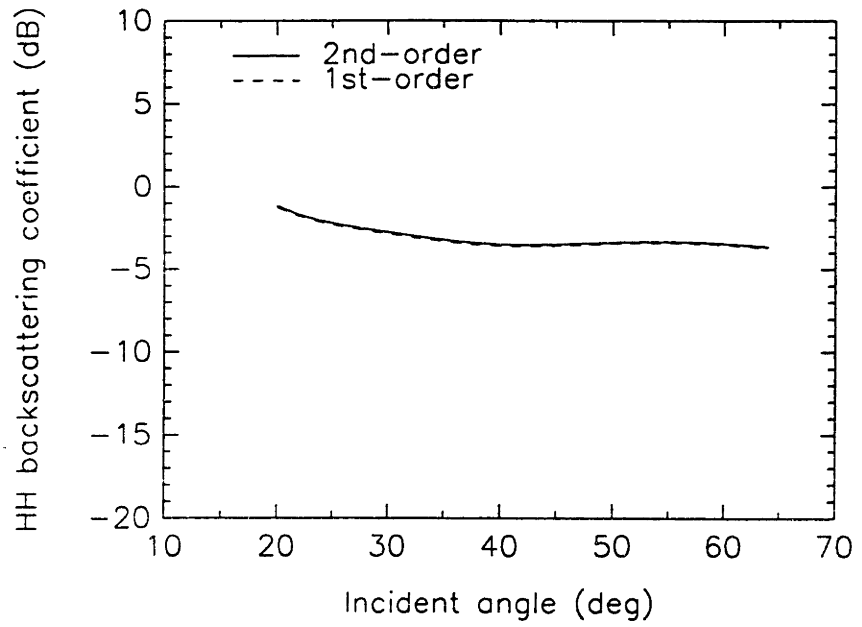

Figure 4 (a) Effect of Double Scattering for HH polarization

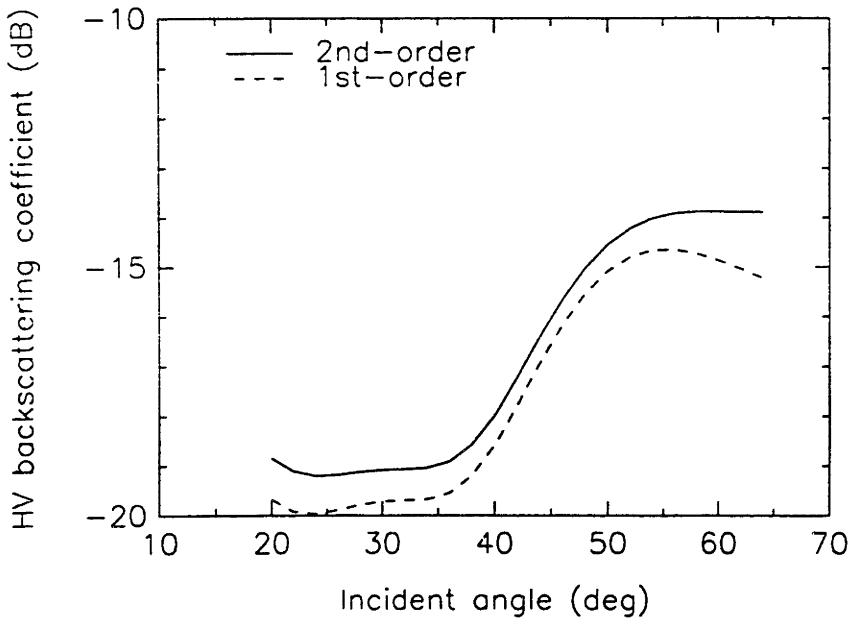

Figure 4 (b) Effect of Double Scattering for HV polarization

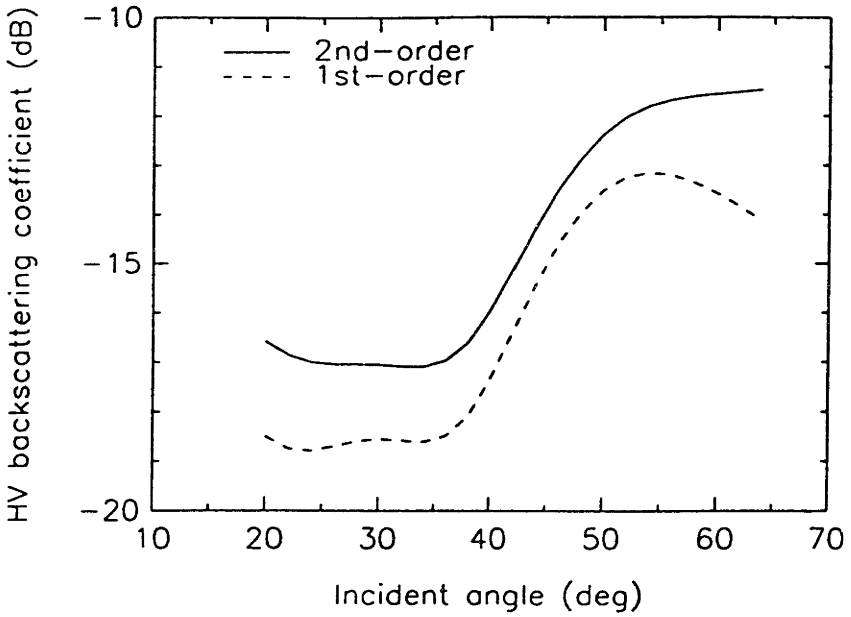

Figure 5 Effect of Double Scattering for HV polarization with 0.2% fractional volume

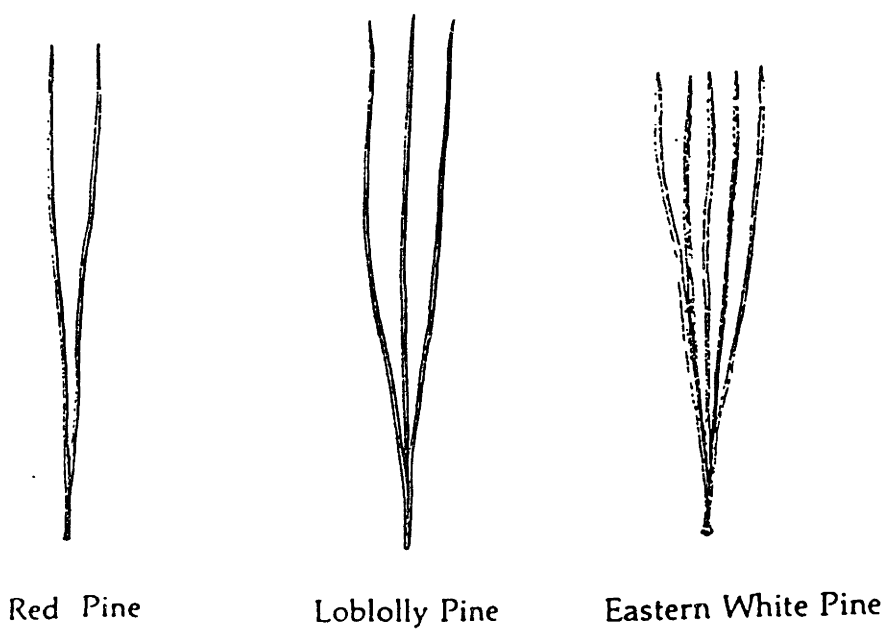

Figure 6 Sample of Pine Tree Needles (from "City of Trees" by Choukas-Bradley and Alexander)

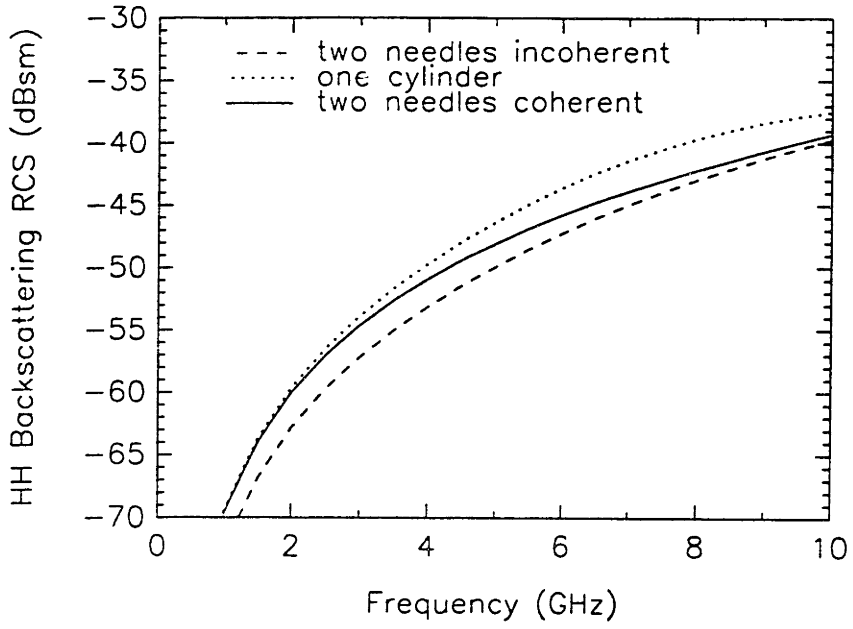

Figure 7 (a) Frequency Dependence of Tree Needles Structure for HH-Pol

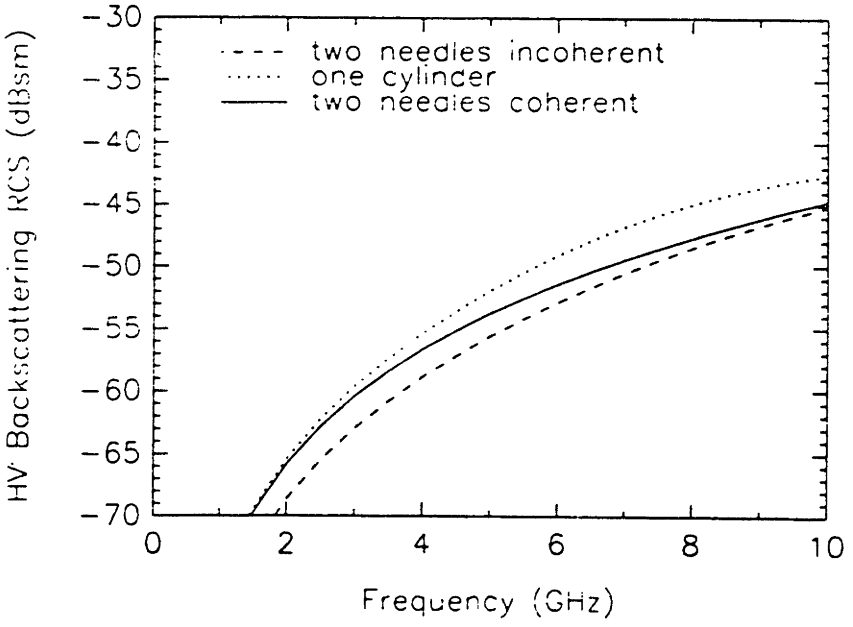

Figure 7 (b) Frequency Dependence of Tree Needles Structure for HV-Pol

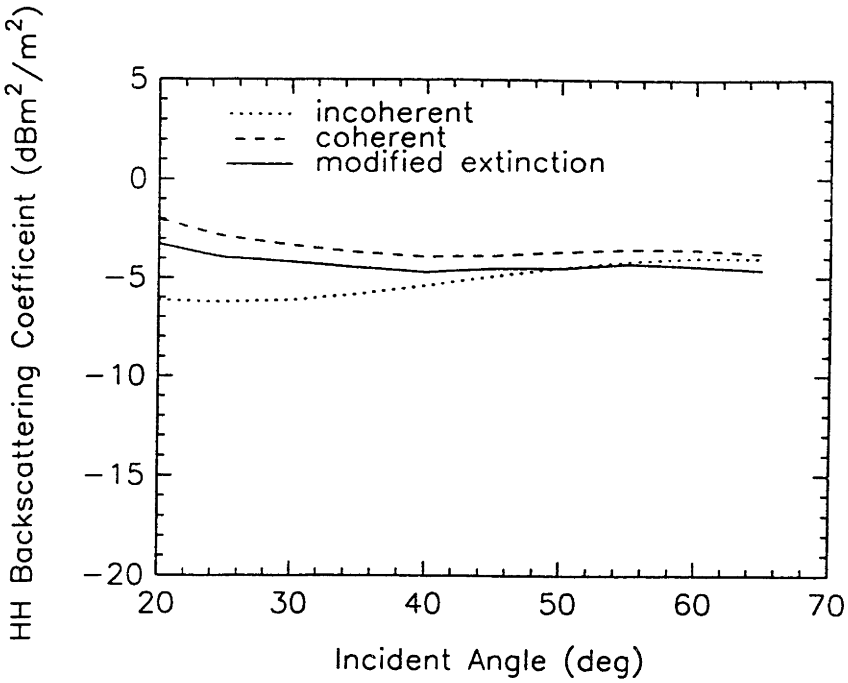

Figure 8 (a) Effect of Extinction Correction for HH-pol

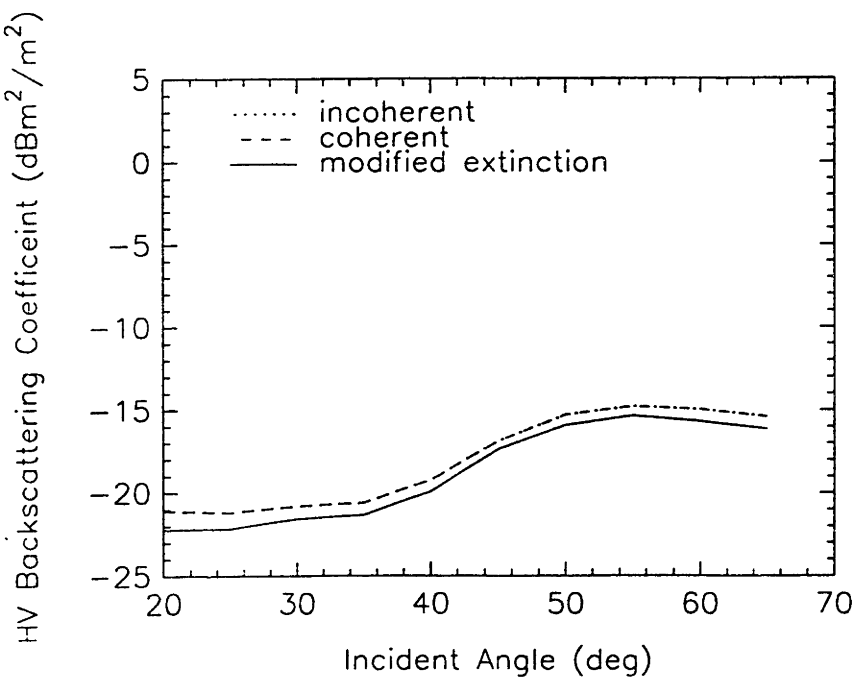

Figure 8 (b) Effect of Extinction Correction for HV-pol

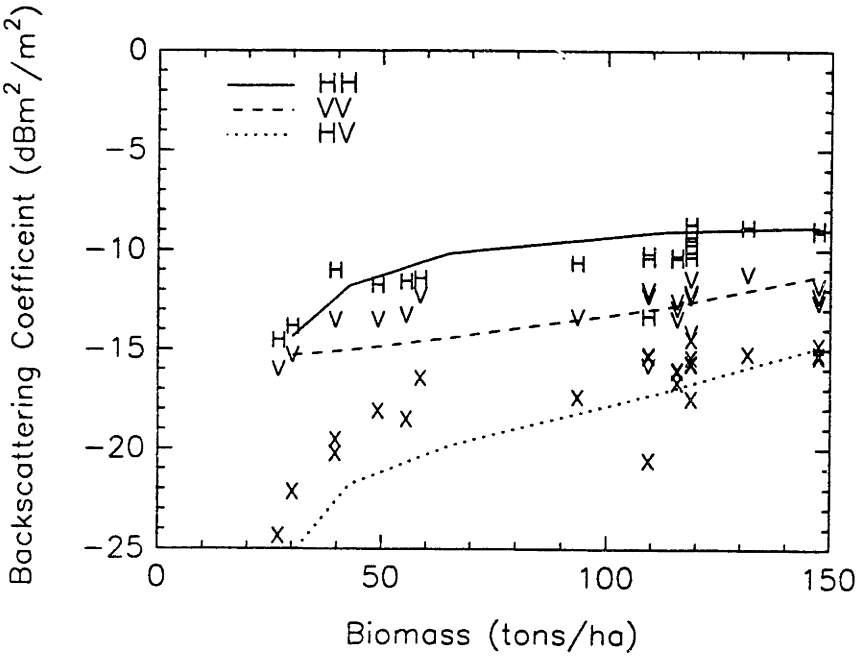

Figure 9 Comparison of Mastro-1 Data and Theoretical Simulation at P-band

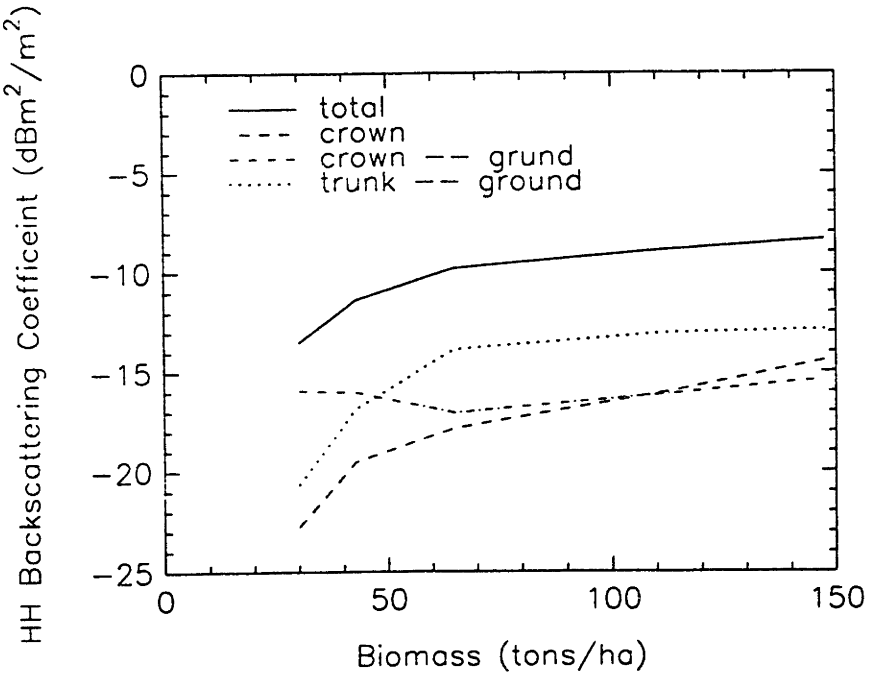

Figure 10 (a) Contribution to P-band Backscattering for HH-pol

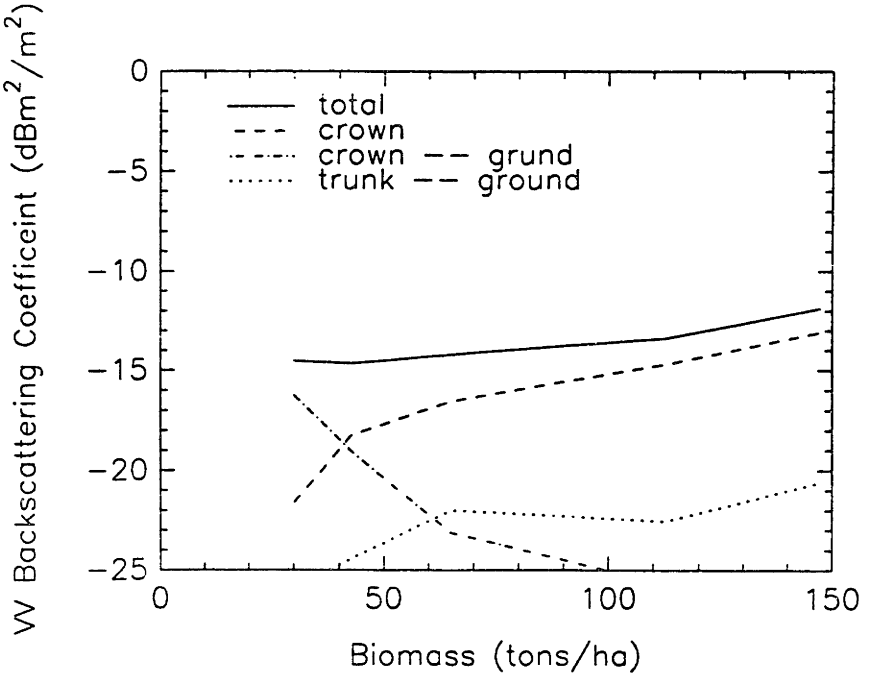

Figure 10 (b) Contribution to P-band Backscattering for VV-pol

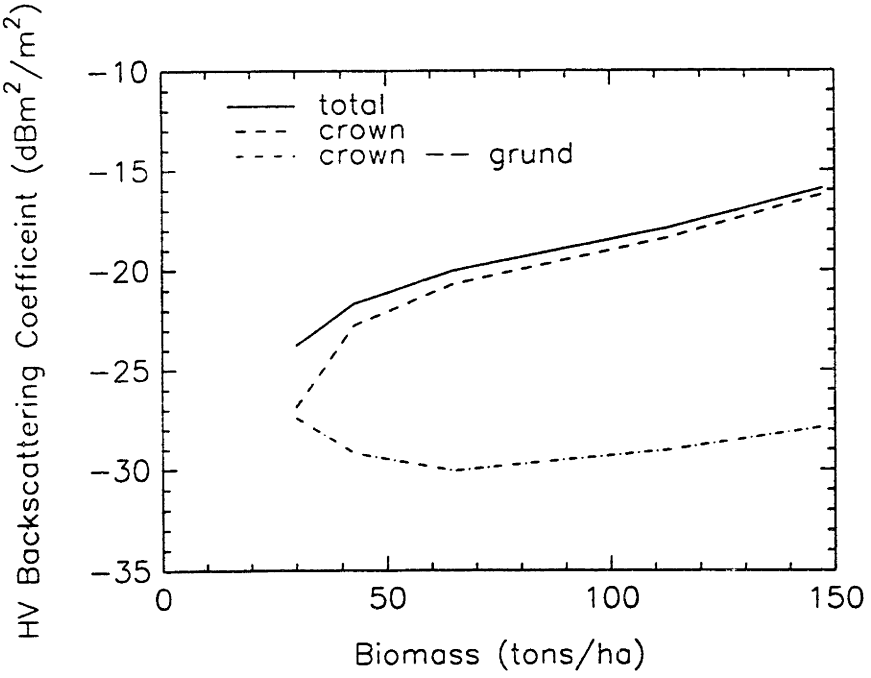

Figure 10 (c) Contribution to P-band Backscattering for HV-pol

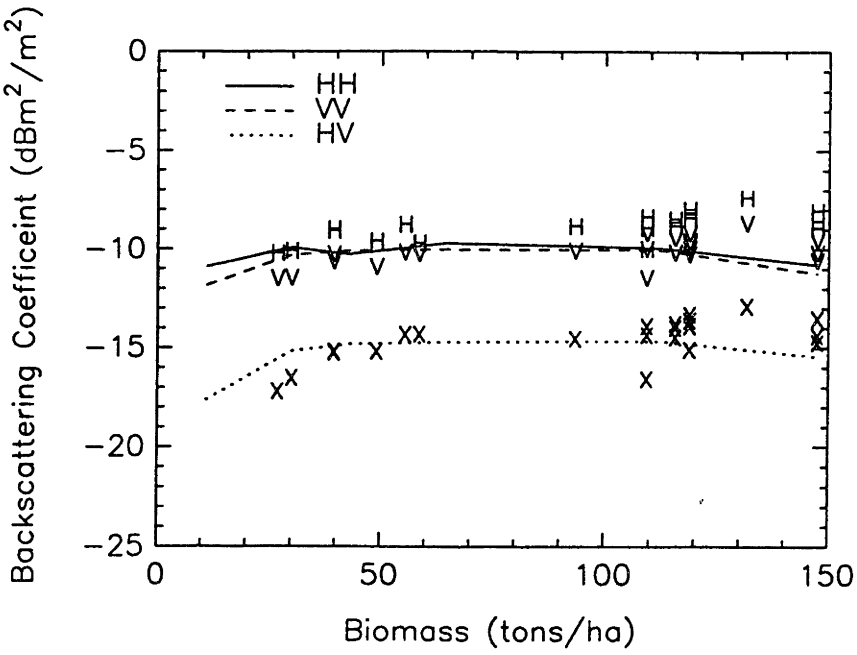

Figure 11 Comparison of Mastro-1 Data and Theoretical Simulation at L-band

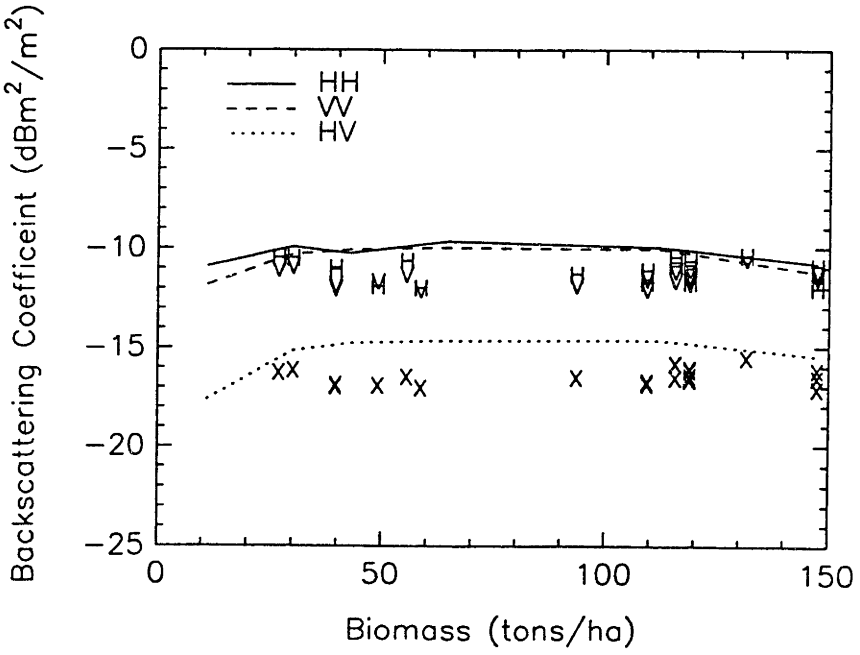

Figure 12 Comparison of Mastro-1 Data and Theoretical Simulation at C-band

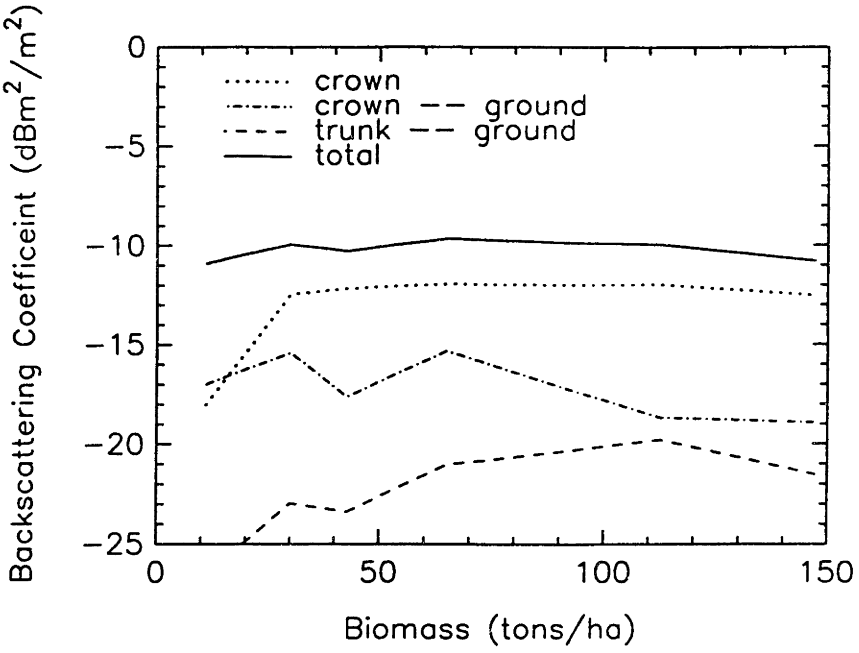

Figure 13 Contribution to L-band Backscattering for HH-pol

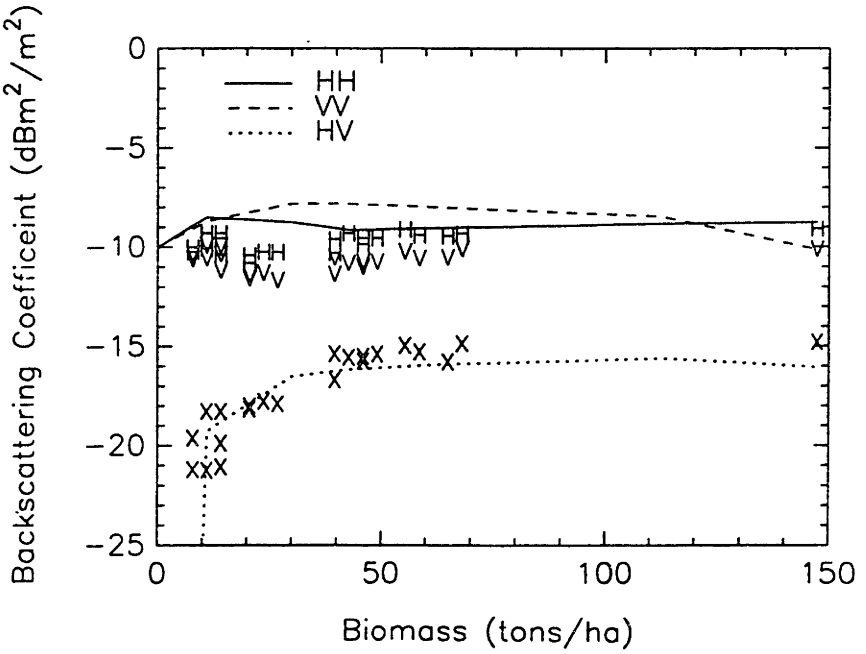

Figure 14 Comparison of SIR-C Data and Theoretical Simulated σ_0 at L-band

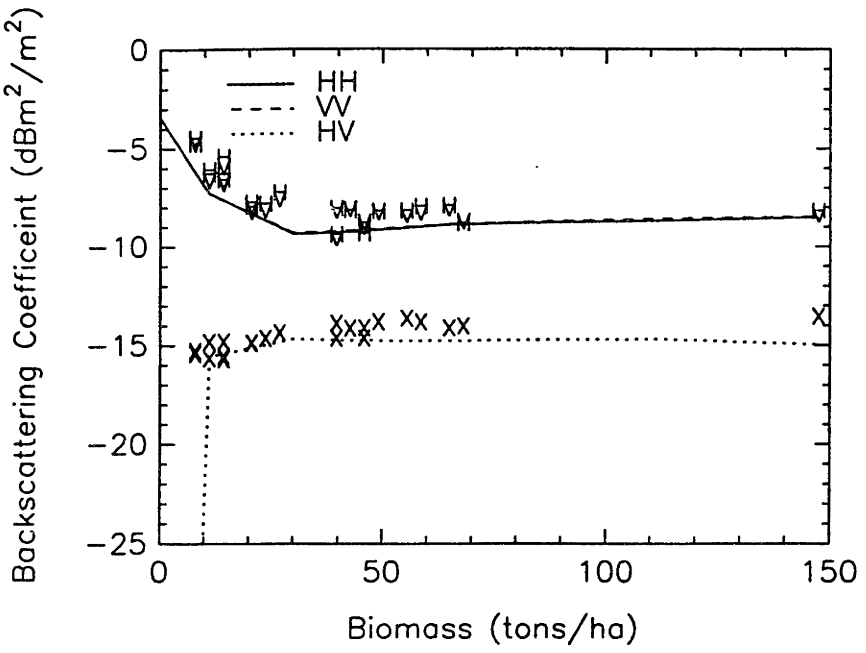

Figure 15 Comparison of SIR-C Data and Theoretical Simulated σ_0 at C-band

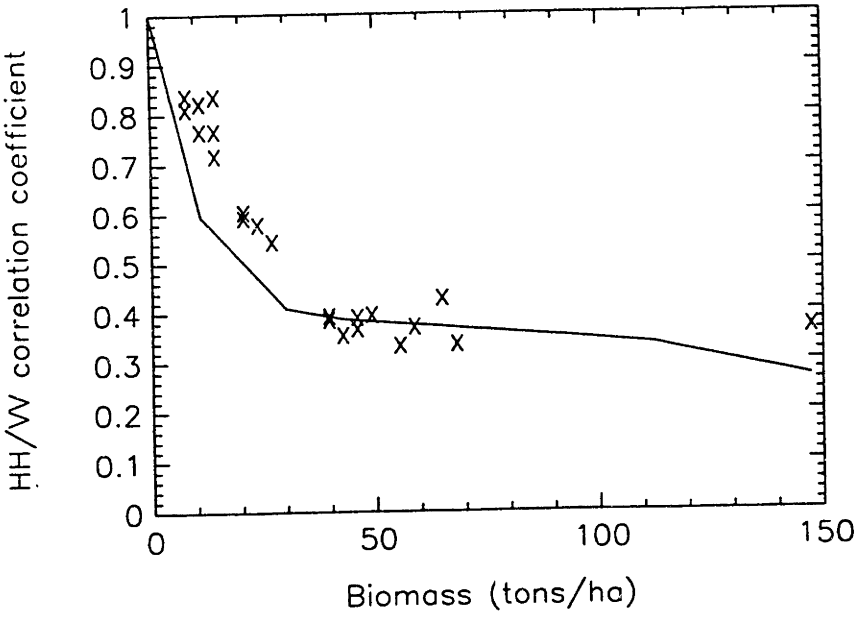

Figure 16 Comparison of SIR-C Data and Theoretical Simulated ρ at L-band

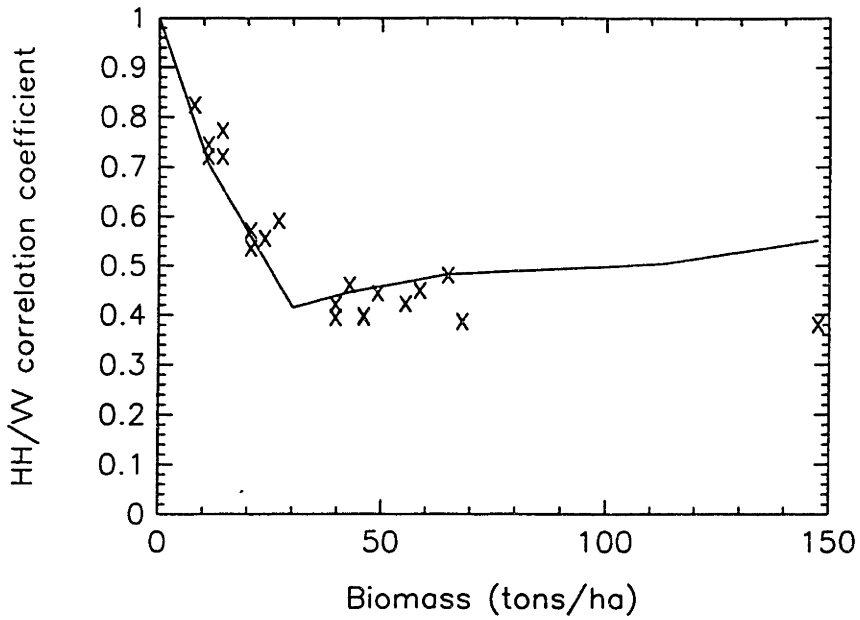

Figure 17 Comparison of SIR-C Data and Theoretical Simulated ρ at C-band

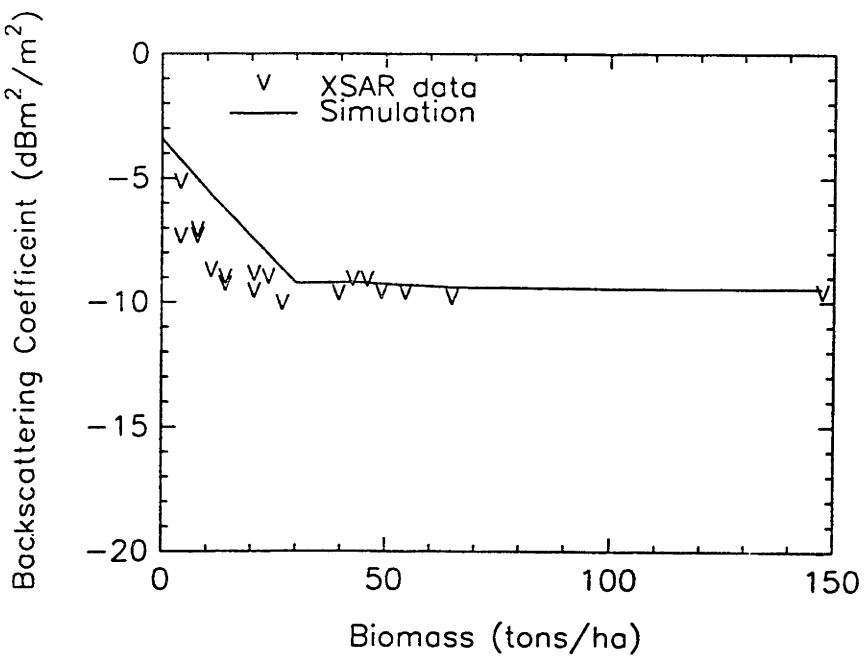

Figure 18 Comparison of SIR-C/XSAR Data and Theoretical Simulated σ_0 at X-band

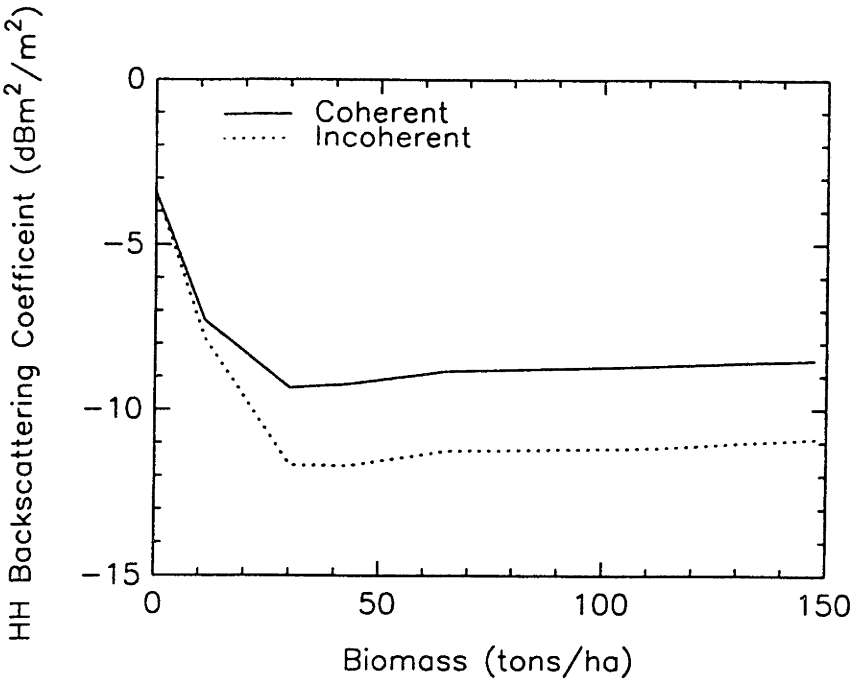

Figure 19 (a) Coherent Structure Effect at C-band with HH-pol

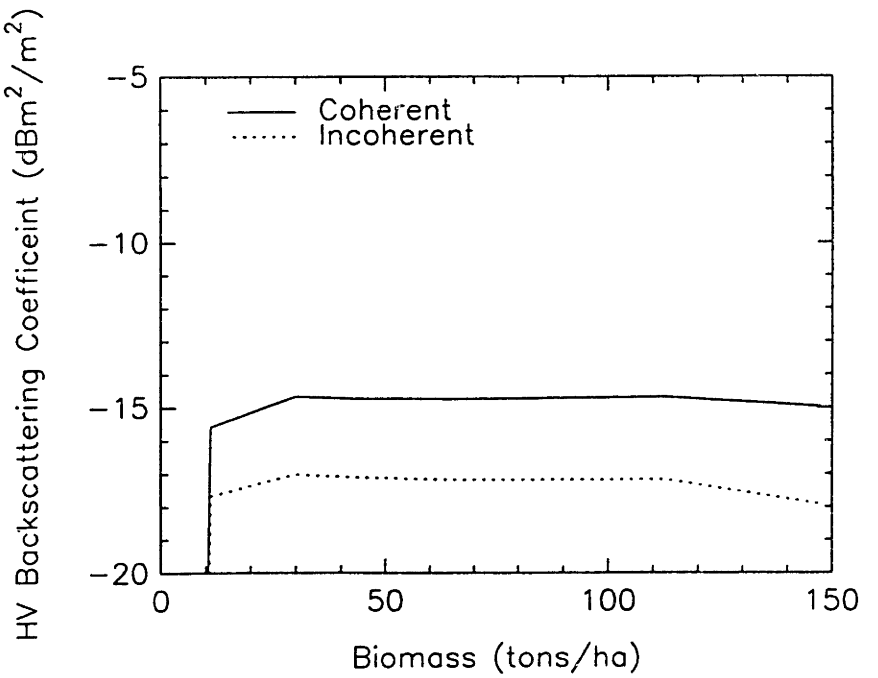

Figure 19 (b) Coherent Structure Effect at C-band with HV-pol

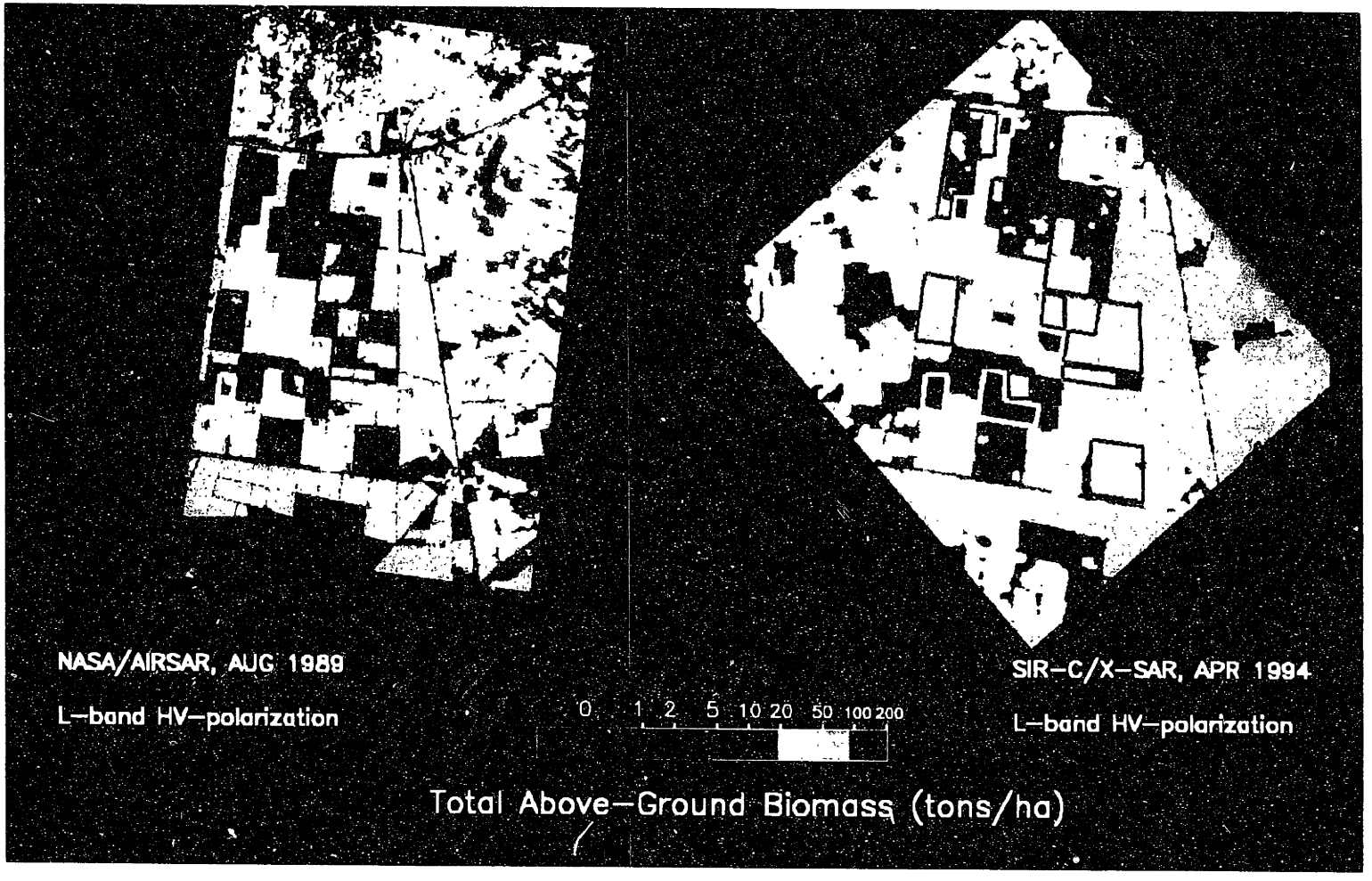

Figure 20 Biomass Monitoring over the Landes Forest between 1989 and 1994

(Courtesy of CESBIO and JPL)

Chapter 3.

MMW Scattering from Isolated Tree

ABSTRACT – The physical characterization of the terrain background is usually in terms of a layered random medium with continuous or discrete scatterer models. To simulate the MMW scattering from isolated trees, a tree model which is consisted of a crown as the random medium and trunks and large branches as deterministic objects is developed. The trunk is modeled as a circular cylinder with random surface roughness where Kirchhoff's approximation is used to calculate the radar return from the surface of the trunk. Transmission loss factors, which is caused by absorption and scattering, are included when computing the contribution from interior branches and trunks. The scattering from crown is calculated with the radiative transfer theory. The theoretical predictions are compared with the measurement data of coniferous and deciduous trees by Army Research Laboratory using a 94GHz radar.

3.1 INTRODUCTION

With the advance of high frequency radar technology and its wide application for target detection with the high resolution capability, the milli-meter wave (MMW) radar has been developed and the experiments over man-made and natural terrain have been conducted [Schwering, et al., 1988; Borel and McIntosh, 1990]. However, few MMW scattering models were developed and most researchers resorted to empirical models.

Electromagnetic scattering from the earth terrain is a very sophisticated physical phenomenon. Usually, the earth terrains modeled as a continuous statistical homogeneous layer of random discrete scatterers or permittivity fluctuation [Tsang et al., 1985]. However, in the three-dimensional milli-meter wave (MMW) radar simulation, it is sometimes necessary to consider isolated trees and shrubs as part of the background because of the high resolution associated with the short wavelength as well as individual trees instead of a layer of forest is seen. Also, in the MMW region, the tree crown is large enough to be considered as a layer of random medium with arbitrary shape. In this case, we add additional parameters to characterize the size of the canopy when using the layered random medium model. This model provides means of summing the contributions from individual scatterers, including multiple scattering effects, thus allows us to work on a tree-by-tree basis. Basically, the tree trunk can be treated as a deterministic scatterer much like targets, whereas for branches and leaves we apply the random scatterer model to calculate the backscattering returns.

In this chapter, a radiative transfer (RT) approach in conjunction with the rough surface scattering is constructed for the modeling of an isolated tree. Section 3.2 describes the tree model which is consisted of a crown as a finite size random medium and large trunks and branches as deterministic scattering objects. Part of this work has been published in cooperation with researcher of the Army Research Laboratory (ARL) [Hsu, et al., 1992, 1993b]. In Section 3.3, formulae for the calculation of range profile of trees are developed. Section 3.4 presents the comparison between the theoretical simulation and the experimental data collected by the Army Research Laboratory using a 94 GHz radar. Finally, a sensitivity study and discussion is presented in Section 3.5.

3.2 THE MMW TREE MODEL

The canopy of a tree can be modeled as a random medium of certain shape; e.g., a cone. As shown in Figure 1, the random medium is composed of randomly distributed discrete scatterers embedded in a homogeneous background. Inside the crown, there are trunks or large branches which are modeled as circular cylinders with top random rough surface on top of it. The trunks and large branches are considered to be deterministic objects whose locations, orientation angles, and sizes are specified. The crown layer is treated as a finite size random medium where the twigs and coniferous leaves are modeled as dielectric circular cylinders and elliptical disks are used to model the deciduous leaves. The statistical orientation and size distribution of twigs and leaves are considered in the calculation of attenuation and scattering characteristics of the random medium.

The scattering from the crown as a random medium is solved with the use of the radiative transfer (RT) theory. The vector RT equation for the specific intensity in the scattering region has the following form

$$\begin{aligned}\frac{d\bar{I}(\theta,\phi,s)}{ds} &= -\bar{\bar{\kappa}}_e(\theta,\phi)\cdot\bar{I}(\theta,\phi,s) \\ &\quad + \int_{4\pi} d\Omega' \bar{\bar{P}}(\theta,\phi;\theta',\phi')\cdot\bar{I}(\theta',\phi',s)\end{aligned} \tag{1}$$

where (θ,ϕ) is the direction of specific intensity and s is the distance of wave traveling inside the random medium. The Stokes vector $\bar{I}$ contains the information regarding field intensity and phase relation of the two orthogonal polarizations h and v and is defined as

$$\bar{I} = \begin{pmatrix} I_h \\ I_v \\ U \\ V \end{pmatrix} = \frac{1}{\eta}\begin{pmatrix} \langle|E_h|^2\rangle \\ \langle|E_v|^2\rangle \\ 2\,\mathrm{Re}\langle E_v E_h^*\rangle \\ 2\,\mathrm{Im}\langle E_v E_h^*\rangle \end{pmatrix} \tag{2}$$

In (2), the subscripts h and v represent the horizontal and vertical polarizations, respectively. The angular bracket $\langle\ \rangle$ denotes ensemble average over the size and orientation distributions of scatterers; and $\eta = \sqrt{\mu_0/\epsilon_0}$ is the free-space characteristic impedance.

The extinction matrix $\overline{\overline{\kappa}}_e$ represents the attenuation caused by both the scattering and absorption, and can be obtained through the optical theorem using the forward scattering function. The phase matrix $\overline{\overline{P}}(\theta, \phi; \theta', \phi')$ characterizes the scattering of the Stokes vector from (θ', ϕ') direction into (θ, ϕ) direction. It can be calculated from the scattering functions of randomly distributed discrete scatterers. Along with the boundary conditions that require the Stokes vector to be continuous, we can solve the radiative transfer equations iteratively for the backscattering radar cross-section as described in chapter 2. The boundary condition for this case is the specific intensity is continuous across the cone-shape crown.

To model the scattering from trunks and large branches with rough surfaces, a two scale surface structure is considered. The large variation is circular and represents the general shape of the trunks or large branches. The small scale variation is a random rough surface with the height and surface correlation function assumed to be Gaussian processes. The Kirchhoff's approximation is used to calculate the scattering from the random rough surface. Since the large scale variation is slowly varying compared with the wavelength in MMW, the curved surface effect is considered by integration over the distribution of large scale surface tilted angles.

3.3 CALCULATION OF RANGE PROFILE

For ground or vehicular radar system where the antenna is looking up or nearly horizontal, the ground effect can be ignored. The first-order iterative solution of the RT equation, which specifies the scattering Stokes vector $\bar{I}_s$ in terms of incident Stokes vector $\bar{I}_0$ is expressed as follows:

$$\begin{aligned}\bar{I}_s(\theta,\phi,s=l_2) = &\int_{l_2}^{l_1} ds' \overline{\overline{D}}(\beta(\theta,\phi)(l_2-s'))\overline{\overline{D}}(\beta(\pi-\theta_0,\phi_0)(l_2-s')) \\ &\overline{\overline{P}}(\theta,\phi,\pi-\theta_0,\phi_0)\cdot\bar{I}_0(\pi-\theta_0,\phi_0,s=l_2) \\ =&\overline{\overline{M}}\cdot\bar{I}_0(\pi-\theta_0,\phi_0,s=l_2)\end{aligned} \tag{3}$$

where $\overline{\overline{D}}(\beta(\theta,\phi)s')$ is a 4×4 diagonal matrix with $e^{(\beta_i(\theta,\phi)s')}$ as its i-th diagonal element. Here β_i is the i-th eigenvalue of $\overline{\overline{\kappa}}_e$. s' is in the distance in the direction of propagation and l_1, l_2 are the boundaries of the random medium.

Equation (3) represents the single scattering by the discrete scatterers inside the random medium with the attenuation taken into consideration. $\overline{\overline{D}}$ is the attenuation factor and $\overline{\overline{P}}$ can be considered as the scattering function for the intensity. $\overline{\overline{M}}$ is the Mueller matrix with elements M_{11}, M_{22} and M_{12} related to the radar cross-sections per unit area for HH and VV and HV polarizations, respectively. Assuming the uniform density of scatterers inside the crown, the backscattering can be expressed as

$$\begin{aligned}M_{11} &= \int_{l_2}^{l_1} ds' n_0 < |f_{hh}|^2 > \cdot e^{-2\kappa_{eh}(s'-l_2)} \\ M_{22} &= \int_{l_2}^{l_1} ds' n_0 < |f_{vv}|^2 > \cdot e^{-2\kappa_{ev}(s'-l_2)} \\ M_{12} &= \int_{l_2}^{l_1} ds' n_0 < |f_{hv}|^2 > \cdot e^{-(\kappa_{ev}+\kappa_{eh})(s'-l_2)}\end{aligned} \tag{4}$$

where $\kappa_{e\alpha} = \frac{2\pi n_0}{k}\cdot 2Im < f_{\alpha\alpha} >$ is the attenuation rate for the polarization α which could be either h or v. n_0 is the number density of the scatterers. $< |f_{\alpha\beta}|^2 >$ is the average scattered intensity from scatterers and is a function of particle size, shape and dielectric properties.

If the random medium is azimuthally symmetrical around the propagation direction, the radar cross-section per unit range in the propagation direction for the polarization $\alpha\beta$ can be expressed as

$$\sigma_{\alpha\beta}(l) = 4\pi \int_{l-\delta_l}^{l+\delta_l} ds' \int_{A'} d\bar{r}' n_0 < |f_{\alpha\beta}|^2 > \cdot e^{-(\kappa_{e\alpha}+\kappa_{e\beta})s'}/2\delta_l \tag{5}$$

where A' is the plane where the distance to the radar is l and s' is the distance the wave travels inside the crown. δ_l is smaller than the resolution of the radar and with A' contains a large number of scatterers.

In the computation of trunk scattering contributions, the surface roughness is an important factor. At MMW, the wavelength is much smaller than the radius of the trunk and thus the surface roughness, no matter how small it is, can still be comparable to the wavelength. The radar cross-section is calculated by breaking up the trunk surface into small pieces and summing up the response from the individual pieces where the scattering from a tilted random rough surface is calculated using Kirchhoff's approximation. The rough surface height and correlation function statistics are assumed to be Gaussian. The radar cross-section of each small surface is calculated by multiplying the area with the scattering coefficient. Thus the backscattering radar cross-section is

$$\sigma_{\alpha\beta} = \int_A d\bar{r}' \gamma(\theta, \phi, \bar{r}') \cdot e^{-(\kappa_{e\alpha}+\kappa_{e\beta})s'} \tag{6}$$

where A is the trunk surface. γ is the scattering coefficient for the reflected wave from the trunk surface. It is a function of the incident angle (θ, ϕ) and the local curvature of trunk at $\bar{r}'$. s' is the distance of the wave traveled inside the crown before scattered from the trunks.

The scattering from crown and trunks are summed up incoherently to obtain the total backscattering radar cross-section. To calculate the range profile, we need to convolve the radar cross-section per unit length (from Equations 5 and 6) with the radar response of a point target. This impulse response is determined by the bandwidth and the filter function of the radar system.

3.4 COMPARISON WITH EXPERIMENTAL DATA

Two sets of measurements were conducted by the Army Research Laboratory (ARL) using a truck-mounted 94 GHz FM CW radar at the Prado Regional Park near Chino, CA and in Bend, Oregon. The radar system is the Rockwell Instrumented Millimeter Wave System (RIMS). In these experiments, calibrated range profiles of several trees are collected. A high range-resolution of about one foot is achieved by stepping the radar frequency through 470MHz bandwidth. With frequency step size of 10MHz and a total of 48 steps, the system provides range ambiguity to about 15 meters which is larger than the total extent of trees in consideration. The radar looking angle is almost horizontal.

In the first ARL experiment, the radar was aimed at two isolated coniferous trees, as shown in Figure 2. The elevation angles are around 5 degrees (looking up); therefore, the ground effect is ignored in our calculation. Within the cluster, the contribution to scattered fields at 94 GHz mainly comes from the leaves and small branches. The scattered field from the trunk has also been computed separately. The small needles of the tree leaves inside the canopy are modeled as randomly oriented dielectric cylinders.

Using the photographs taken at the scene as shown in Figure 2, in which a yardstick is inserted in front of each tree, these two trees are modeled as cone shape crowns with vertical trunk inside, as shown in Figure 3. The first tree is estimated at 9 meters tall and with the crown length of 7 meters (calculated from the the first live branch to the top of tree). The radii of the top and bottom circles are 0.75m and 3.0m, respectively. As to the second tree, the height of the tree is estimated at 8 meters and the crown length of 6.5 meters. The upper and lower circle radii are 0.2m and 2.7m, respectively. The size and number density of scatterers are given in table 1. The radius and length of the dielectric cylinders, of which the random medium is composed, are assumed to be 0.1cm and 2cm, respectively. The number density of the leaves is $12000/\mathrm{m}^3$ and the dielectric constant is $7 + i1.5$ which is derived from 50% water content with a dielectric model [Ulaby and El-Rayes, 1987] .

The comparisons between the predicted and measured range profiles from the crown of both trees are given in Figures 4 (a) and (b) for the first and the second trees. The measurement and prediction results are given for the HH polarization. The horizontal axis is the range in meter and the vertical axis is the radar cross-section in meter square which is the total radar cross-section within the resolution of the radar. The plotted range which corresponds to the relative range is not the actual range from radar to the trees. The dotted curves are the measured data and the continuous curves are the theoretical simulation. Because we did not have the ground truth information for nearby terrains, the comparison is limited to the extent of the trees. The scattering from the trunk is calculated with the rough trunk surface which have rms height as 0.2cm and correlation length as 1cm. The radius of the trunk of the first tree is estimated as 0.2m and the radius of the second tree as 0.15m. The theoretical simulation includes the contribution from the trunk and the scattering from the crown. The small jump at around 4 meter range for the second tree is the contribution from trunk. It is found that the scattering of the trunk is not important in these two cases because the high density of the leaves. The agreement between the theoretical prediction and the experimental data are generally good although the theoretical simulation is about 2 dB lower than the data. The discrepancy may be due to the fact that the multiple scattering effect is ignored in our calculation.

In the second ARL experiment, the ground truth information is measured more thoroughly. For each tree, the tree type, the height of tree, the sizes of trunk and branches and the average size of leaves are collected in the experiment. The water contents of the trunk and leaves are also measured. The dielectric constants are then derived from the same dielectric model used in the first experiment.

Here we consider two sets of data from the experiment. Pictures and simplified models of two different trees are shown in Figures 5 and 6. The first tree is a Bluegum Eucalyptus and the second one is a California Peppertree. Both trees are deciduous trees with long, narrow leaves. To model these trees, a crown with cone shape and trunks and large branches which are modeled as circular cylinders with Gaussian random roughness on the surface are used. Inside the crown, twigs and leaves are

assumed to be uniformly distributed and randomly orientated in both elevation and azimuthal directions. For tree 1, there are two trunks each with radius of 30cm and height of 11m. For tree 2, there is one trunk with radius of 50cm and height of 2.6m, and three major branches with radii of 40cm, 30cm, and 20cm, and lengths of 8.5m, 8m and 5m. The tilted angle is about 15°. The dielectric constant of bark is $2.1 + i0.18$ which is derived from the 12% water content. The size and density of twigs and leaves inside the crown are summarized in Table 2. The dielectric constant of leaves is $5.2 + i1.7$ which is derived from the 50% water content.

The comparison between the theoretical calculation and the measured data is shown in Figure 7. The range is plotted along the horizontal axis, and the vertical axis shows backscattering radar cross-section for HH polarization. The dotted curves are measured radar cross-section within the range resolution bin of 0.3m, and the solid curves are theoretical calculations which include the trunk and large branches contributions to the scattering. The scattering from trunks and large branches in the deciduous tree is more notable than in the coniferous tree because in general the trunks in deciduous tree is larger and the density of tree leaves is smaller which results in higher scattering and lower attenuation. As shown in the Figure, while the average value of radar cross-section is close to the measured data, there are significant deviations between the smooth theoretical curve and the data curve. Since the variation of leaves density for deciduous tree is much higher than that of coniferous tree, it cannot be explained solely by the random fluctuations (i.e., speckle) in the measurement. Based on the photo of the trees, this variation may also come from the variations in the scatterer density from one range bin to another. Because the received field is the coherent scattering from multiple scatterers within the radar field of view in both angles and ranges, this fluctuation can be reduced if the data is averaged over multiple angles. As can be seen from the picture of these two trees, their outlines are not exactly cone shapes as we assumed, and the leaves and twigs inside the crown are not uniformly distributed. There are voids in various spots. These factors result in the variation of effective scatterer density within the range bin, which corresponds to a slice from the total tree volume. From the observation of Figure 7 (a), it is also found that the back part of the curve for tree number 1 did not fit as well. The reason

is probably because that the fractional volume of leaves in tree number 1 is higher so that the multiple scattering effect, which is ignored in our calculation, is important. Multiple scattering could appear as late time returns which correspond to the further range.

3.5 NUMERICAL SIMULATION

Due to the fact that the geometry of trees are very complicated and considerable simplification has been made to simulate the measured radar return, it is necessary to examine several physical factors that might affect the returns using numerical simulations. In part of this study, we are also interested in the quantitative dependence of the range profile on selective parameters of the tree model. These parameters tend to vary from trees to trees, and hence should provide more insights to the modeling effort. The following is a sensitivity study based on the tree size, number density of leaves and the orientation distribution of leaves. The variations are limited to the crown, so the contribution from trunk are not shown in the comparison.

First of all, the number density and the size of the tree are varied. It is found that for overall backscattering cross-section, the most sensitive parameters are the size of the tree and the scattering versus attenuation ratio. While increasing leave density would increase both attenuation and scattering, it has much less impact on the total scattered power. It is also found from this study of deciduous trees that the backscattering cross-section has little dependence on the sizes and shapes of leaves as long as they are randomly orientated.

Figure 8 shows the range profile of two trees with different sizes. One has radii of top and bottom circles as 0.75m and 3.0m, respectively, and is 9m tall. Another has radii of top and bottom circles at 1.125m and 4.5m, respectively, and is 13.5m tall. It was shown that the peak radar cross-section of the second tree is about 2 to 3 dB higher and the range of significant radar return is about 50% wider. This matches the increase in the tree size. The simulation on different number density of the leaves is shown in Figure 9. As the number density increases, the radar cross-section from the front part of the range profile increases, but it also decreases faster with increasing range at the backside of the tree. This is because as the number density of leaves increases, both scattering and attenuation increase. The radar return from the front part of the tree would increase but the return from the back side of the tree would decrease due to the higher attenuation.

A few simplifications in our model and some uncertainties of physical parameters of scatterers may have affected the accuracy. First, the scattering and attenuation from the leaves are calculated from the approximated solution in terms of both physical model and scattering function. Also, the dielectric constant is derived from a empirical model which measures the reflectivity and transmissivity of the tree samples. Since the MMW measurement is very difficult, the highest frequency used is 20 GHz [Ulaby and El-Rayes, 1987]. The extrapolation to 94 GHz may be erroneous. These uncertainties are likely to have impact upon the scattering/attenuation ratio (Albedo). Therefore, We performed a simulation in which the scattering coefficient is kept intact but the attenuation coefficient is varying. As the results shown in Figure 10, the front part of the range profile does not change, as is expected since the attenuation does not affect this part significantly. But for the backside of the tree, the lower attenuation is, the larger the radar cross-section and the wider the range with appreciated radar return. Therefore in the model, a correct estimation of attenuation is very important.

Another parameter which would have large impact on the backscattering cross-section is the elevation orientation distribution of leaves. Here we use the average leaf size of tree number 1 as the size of elliptic disk scatterers and simulate several cases. The azimuthal orientation angle is assumed to be uniformly distributed. The backscattering cross-sections with various orientation distributions are shown in Figure 11 (a). The horizontal axis is the depression angle and the vertical axis is the backscattering cross-section. For elevation angle distribution, $\sin\theta$ represents uniformly distributed leaves, $\sin\theta\cos\theta$ represents more vertically orientated leaves, and $\sin^2\theta$ represents more horizontally oriented leaves. For a radar look angle near the horizontal axis, strong returns come from leaves with surface normals close to the incident angle, which is horizontal. As expected, for uniformly distributed leaves, the angular response is flat. When the leaves tend to be more vertical, the backscattering becomes higher at lower depression angle and decreases with increasing depression angle. When the leaves tend to be more horizontally distributed, it is the other way around. Therefore, we conclude that the backscattering cross-section is sensitive to the orientation distribution of leaves. This orientation dependence is also observed in another study

[Borel and McIntosh, 1990]. On the other hand, the impact of orientation distribution on the attenuation is small, as shown in Figure 11 (b). This is because that the total attenuation is a sum of the scattering loss and the absorption loss. The absorption loss has little dependence on orientation angle of scatterers and the scattering pattern of scatterers would change dramatically with orientation angle distribution. The integration of all scattering angles which give rise to the scattering loss is not as sensitive to the orientation angle distribution.

As suggested in the previous section, one possible reason for the variation shown in the measured range profile is the irregular shapes of crown and the nonuniform density distribution of leaves inside the crown. We attempt to verify this postulate by simulating the effect of varying density of scatterers inside the crown based on the pictures of trees and the measured data. The parameters used are the same as those of Figure 12. The only difference is that the density of leaves is varying from 100 to 400 $/m^3$ for tree number 1. As shown in the Figure, the inhomogeneous distribution of scatterers can indeed generate larger variation of backscattering cross-section similar to the measured data. This suggests that future observations may include measurements of effective scatterer density on every slice of range bin to provide quantitative comparison with the theory.

3.6 CONCLUSION

In this study, a MMW scattering model of single tree is developed based on the combination of the random medium model and the scattering from deterministic objects is proposed. Using this model, The theoretical calculations are compared with measured radar range profiles at 94 GHz using the collected ground truth. We found that the simulation results are consistent with the observed range profiles, with the exception of some large variations from one range bin to another. Some slight discrepancy with experimental data may be resulted from the approximation in the physical model of tree components. The simulation is also presented to examine the sensitivity of different parameters.

Tree	1	2
top circle radius	0.75 m	0.2 m
bottom circle radius	3.0 m	2.7 m
height	7.0 m	6.5 m
radius of twigs	0.4 cm	0.4 cm
length of twigs	20 cm	20 cm
density of twigs	$150 / m^3$	$150 / m^3$
radius of needles	0.1 cm	0.1 cm
length of needles	2.0 cm	2.0 cm
density of needles	$12000 / m^3$	$12000 / m^3$

Table 1 Table of the Parameters for Two Coniferous Trees

Tree	1	2
top circle radius	2.0 m	3.0 m
bottom circle radius	3.5 m	4.0 m
height	11.6 m	9.2 m
radius of twigs	0.2 cm	0.1 cm
length of twigs	20 cm	20 cm
density of twigs	$10 / m^3$	$5 / m^3$
major axis of leaves	7.62 cm	1.9 cm
minor axis of leaves	0.95 cm	0.635 cm
thickness of leaves	0.02 cm	0.02 cm
density of needles	$200 / m^3$	$300 / m^3$

Table 2 Table of the Parameters for Two Deciduous Trees

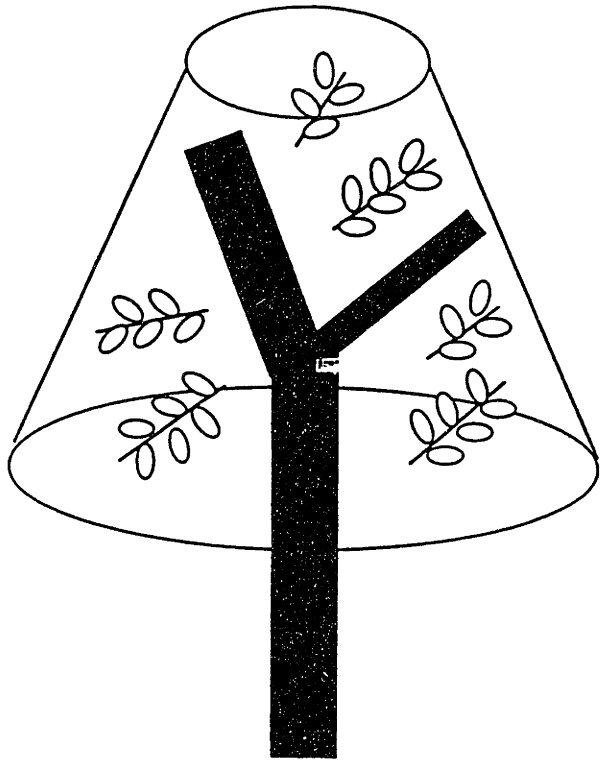

Figure 1 Configuration of the Model

Figure 2 (a) Picture of Coniferous Trees 1

Figure 2 (b) Picture of Coniferous Trees 2

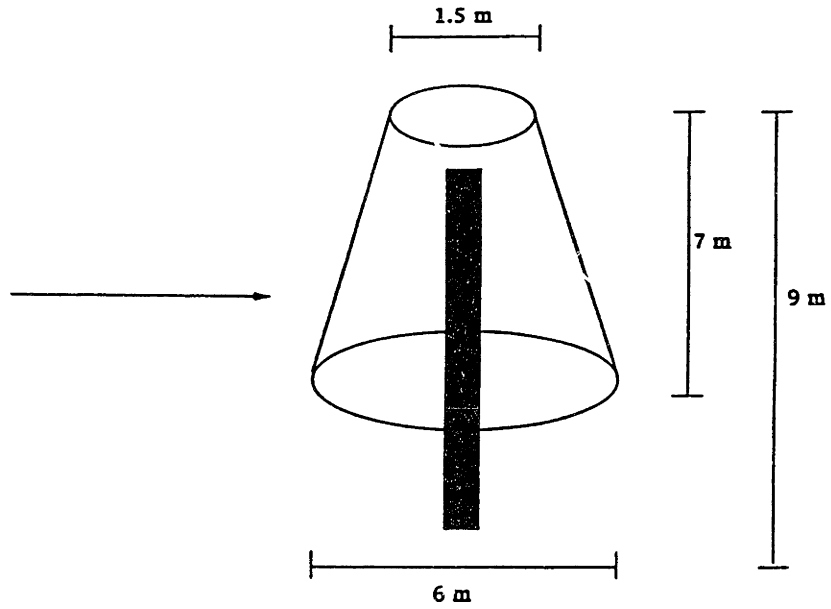

Figure 3 (a) Model of Coniferous Trees 1

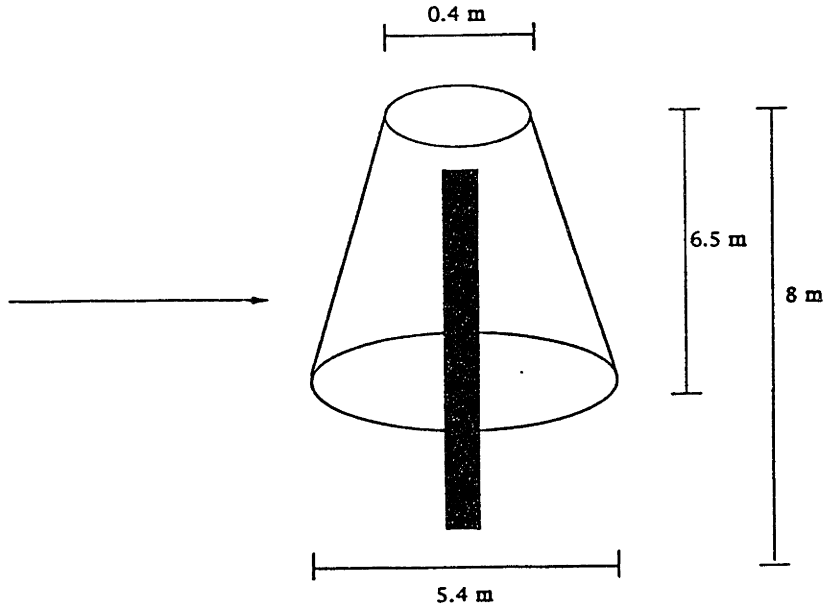

Figure 3 (b) Model of Coniferous Trees 2

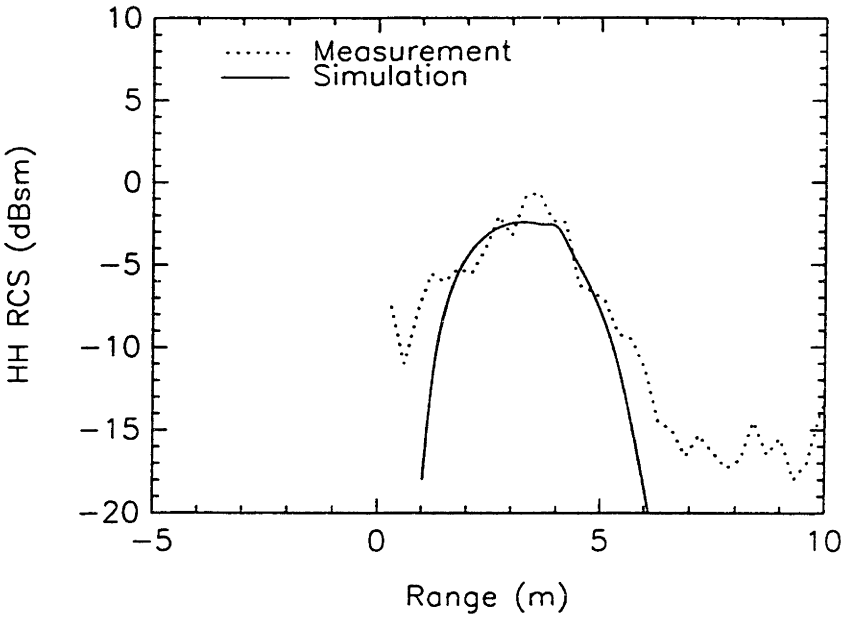

Figure 4 (a) Comparison of Measured and Simulated Range Profile for Coniferous Tree 1

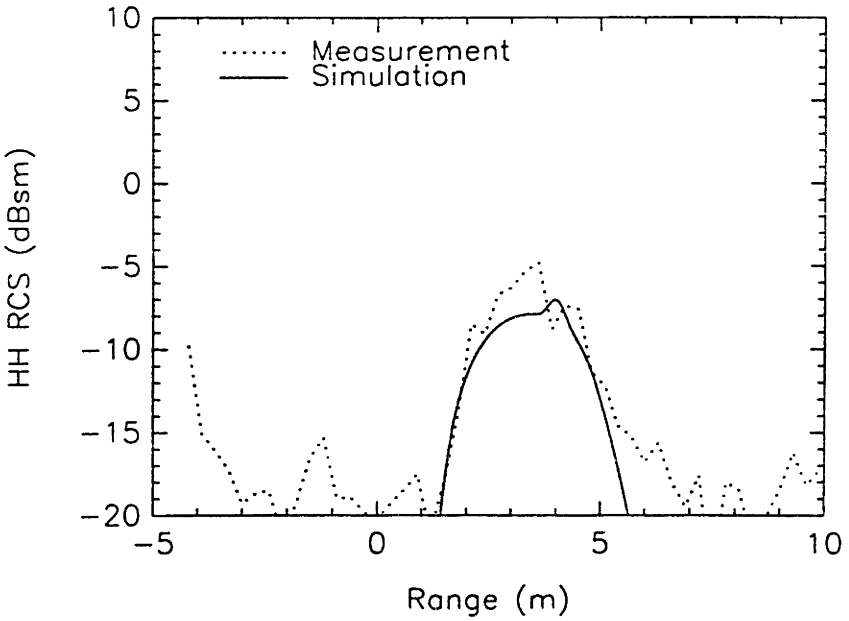

Figure 4 (b) Comparison of Measured and Simulated Range Profile for Coniferous Tree 2

Figure 5 (a) Picture of Deciduous Trees 1

Figure 5 (b) Picture of Deciduous Trees 2

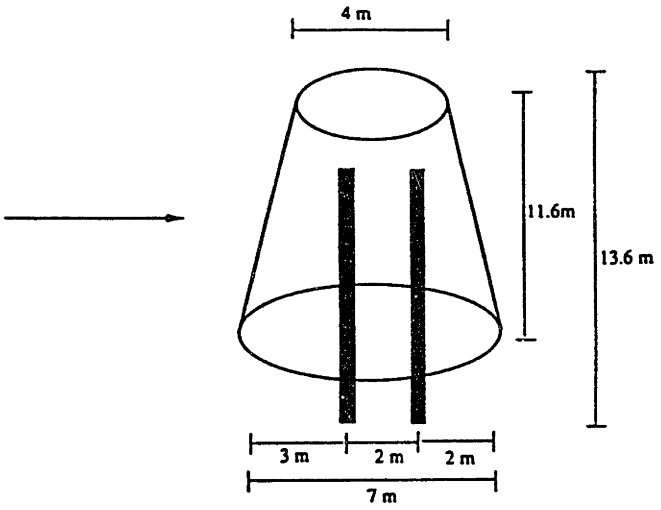

Figure 6 (a) Model of Deciduous Trees 1

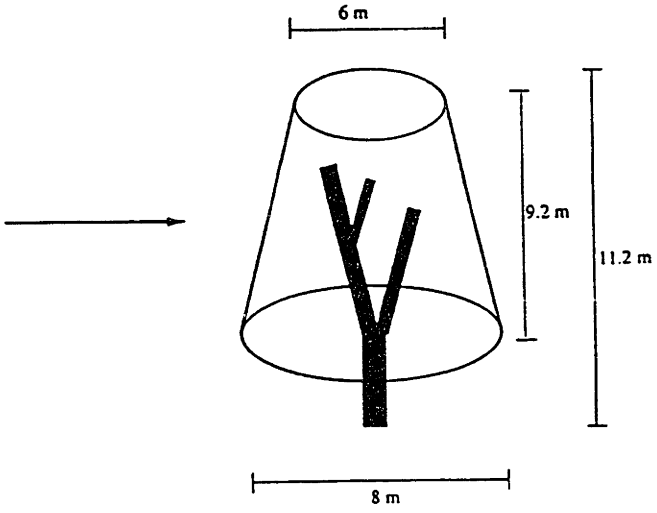

Figure 6 (b) Model of Deciduous Trees 2

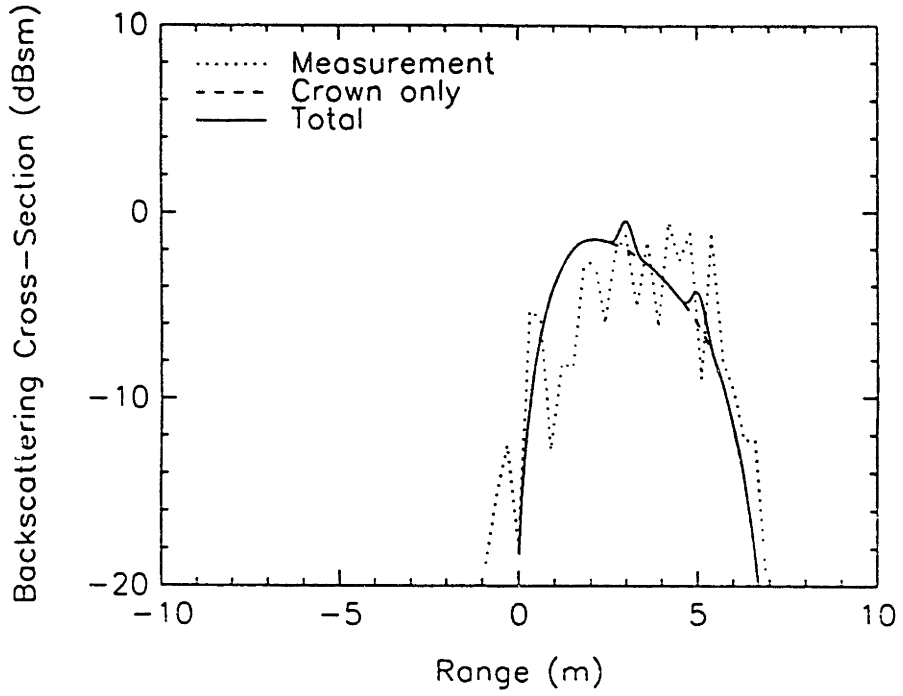

Figure 7 (a) Comparison of Measured and Simulation Deciduous Tree 1 Range Profile

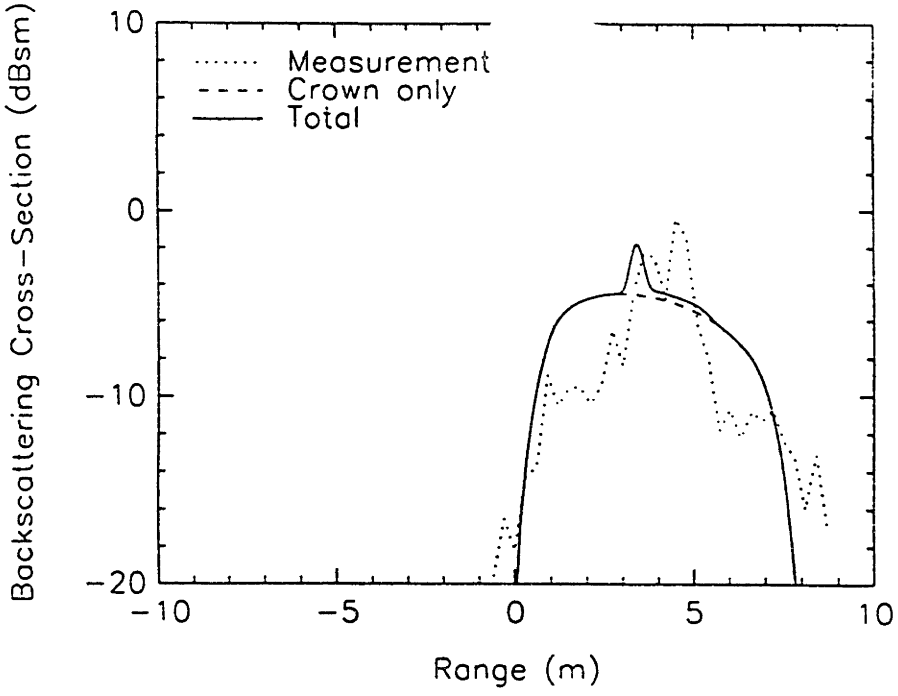

Figure 7 (b) Comparison of Measured and Simulation Deciduous Tree 2 Range Profile

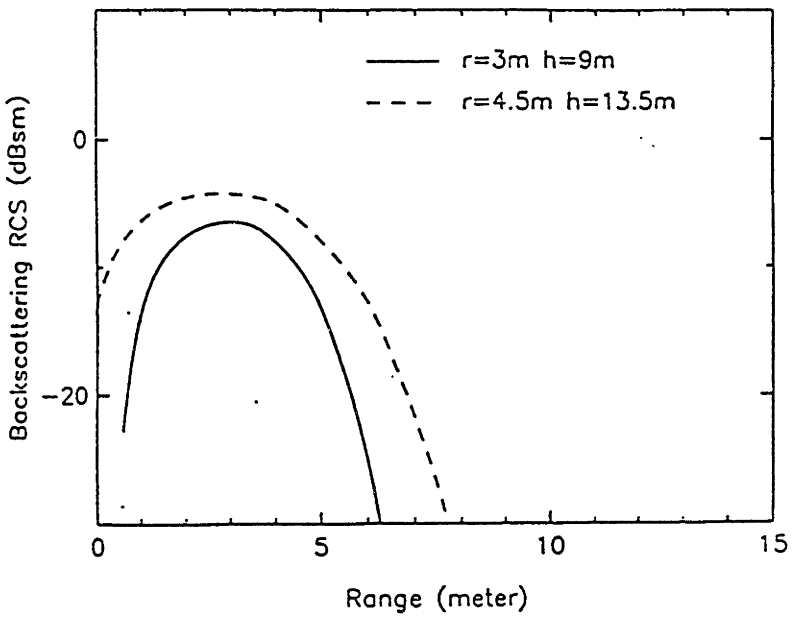

Figure 8 Effect of Tree Size on its Range Profile

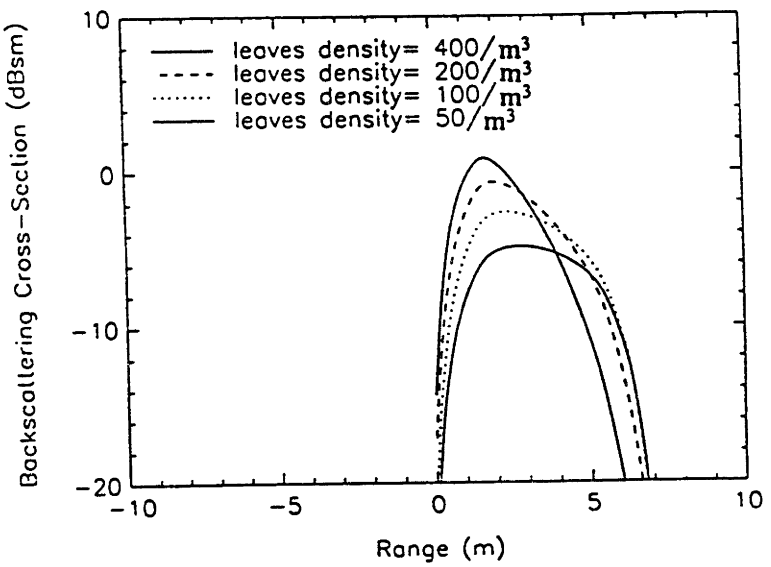

Figure 9 Effect of Leaves Density on its Range Profile

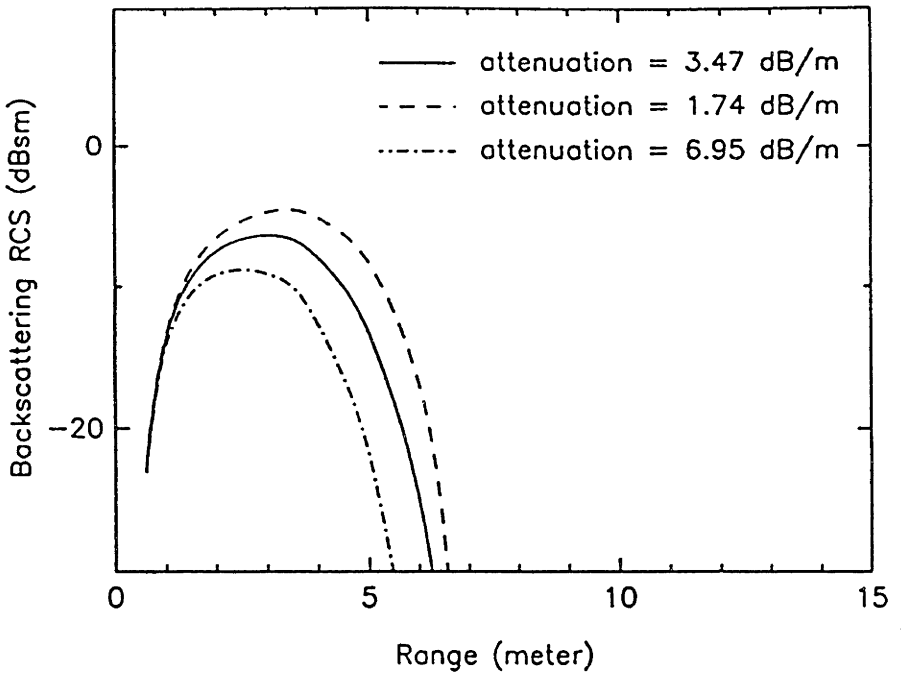

Figure 10 Effect of Albedo on its Range Profile

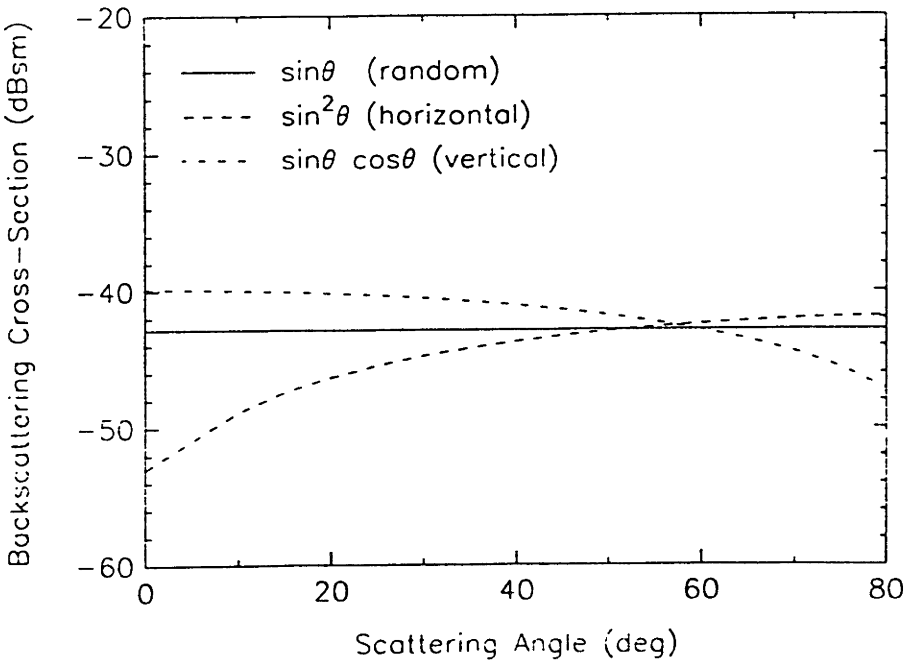

Figure 11 (a) Effect of Leaves Orientation Distribution on Backscattering Cross-section

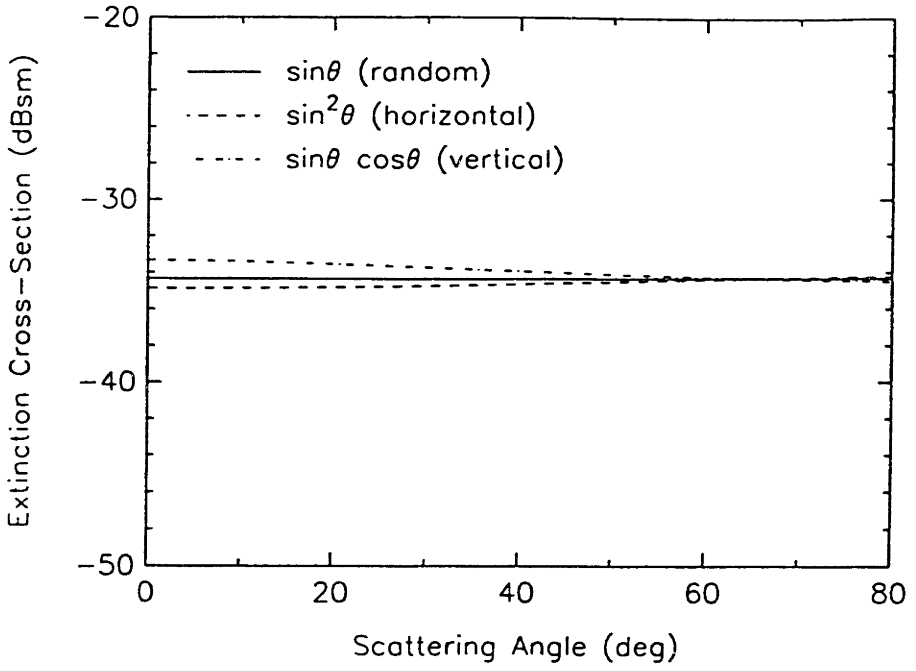

Figure 11 (b) Effect of Leaves Orientation Distribution on Extinction Cross-section

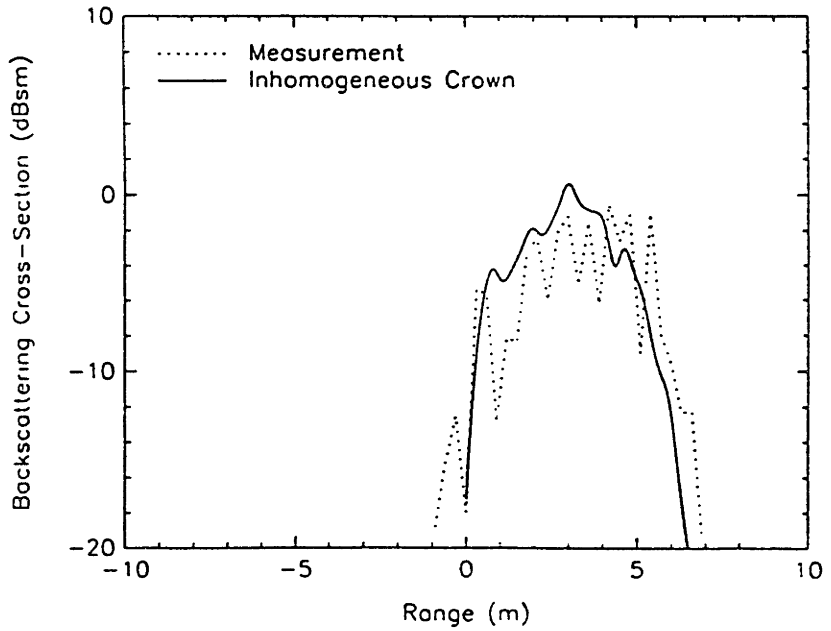

Figure 12 Effect of Leaves Density Distribution on Range Profile

Chapter 4.

Attenuation and Phase Fluctuation due to Foliage

ABSTRACT – In this study, a theoretical model is developed to calculate the mean attenuation, the amplitude and the phase fluctuations of electromagnetic waves propagating through foliage. The attenuation of the average received field is obtained from the sum of the absorption loss and the scattering loss. The amplitude fluctuation of electromagnetic wave is calculated from the bistatic scattering coefficients using the radiative transfer theory. The phase fluctuation is obtained from the amplitude fluctuation assuming the phase of the fluctuation field is uniformly distributed from $-\pi$ to π. The attenuation is then obtained by comparing the radiated power from a source under the foliage to the received power from a source in free space. The theoretical results are compared with experimental data collected by MIT Lincoln Laboratory during the 1990 Foliage Penetration Experiment. In the experiment, transmitters were placed inside the forest and an airborne receiver was used to measure the one-way propagation. This theoretical model is also used to illustrate the polarization and angular dependencies of attenuation and phase fluctuations.

4.1 INTRODUCTION

The utilization of radar to detect stationary targets under the foliage faces several problems. One is the attenuation of electromagnetic wave caused by the foliage. Another is the distortion of received signal. Furthermore, Synthetic Aperture Radar (SAR) has been used to achieve high resolution. However, since SAR system is a coherent process which integrates the receiving field along the synthetic aperture, the random phase fluctuation caused by the foliage occurs along the pass of the antenna will deteriorate the ability to image the target. This attenuation and the phase and amplitude fluctuations of electromagnetic wave caused by the presence of the foliage and their impact on the synthetic aperture radar (SAR) image has been a topic of great interest to radar community. The MIT Lincoln Laboratory conducted a Foliage Penetration (FOPEN) experiment [Ayasli et al., 1991] to investigate the feasibility of detecting stationary targets located inside the forest. Based on the experimental data, the attenuation and the phase fluctuation caused by different polarizations, frequencies, as well as the effect of depression angles and synthetic aperture length have been analyzed [Toups, 1992].

To further investigate the mechanisms for those effects and their dependence on frequencies, polarizations, and incident angles, it is necessary to develop a theoretical model in order to simulate the measurement results. Although there exists abundant theoretical models which can calculate the average scattering coefficients and attenuation from random medium, very few of them are able to simulate the fluctuation of the electromagnetic field in random medium. One such model is proposed by Chu et al. where the wave theory and the continuous random medium model are used to simulate the electromagnetic response of a point source under a layer of random medium [Chu et al., 1992]. The mean attenuation as well as the variance of the phase

fluctuations are obtained. However, small fluctuations are assumed in order to solve the problem analytically.

Since the measured attenuation caused by foliage shows significant fluctuations, it is necessary for theoretical models to include the effect of large fluctuations. One approach is to combine theoretical models for the average scattered coefficients and the statistical clutter model to calculate the fluctuation of the scattering field. The approaches to calculate the average electromagnetic quantities from the random medium have been discussed in chapter 2. In this study, the radiative transfer model is used. As to the statistical clutter model, Gaussian distribution has been used when there are many scattering sources. However, when the resolution of the image becomes higher, the composite K-distribution has to be used [Jao, 1984]. Since the main concern in this study is the average attenuation and phase fluctuation, no assumption of clutter model is made besides the phase of incoherent scattered field, which is assumed to be completely random.

In this chapter, the average attenuation and bistatic scattering coefficients are calculated using a RT model for forest. With the assumption of uniform phase distribution of the scattered field, the statistical average of other electromagnetic quantities such as the amplitude and phase distributions are calculated. Part of this work has been published in cooperation with the MIT Lincoln Laboratory [Hsu, et al., 1993a]. The FOPEN experiment is described in Section 4.2. In Section 4.3, the methodology of this approach is described. The forest scattering model is described in Section 4.4 and finally, a comparison between the measured attenuation and phase fluctuation and the theoretical simulation is presented in Section 4.5.

4.2 FOPEN EXPERIMENT

The MIT Lincoln Laboratory conducted a Foliage Penetration experiment (FOPEN) on July, 1990 at Portage, Maine. The area surrounding Portage is predominantly coniferous forests with varying densities and ages. The radar system used in this experiment was the National Aeronautics and Space Administration (NASA) / Jet Propulsion Laboratory (JPL) Synthetic Aperture Radar (SAR) on board a DC-8 aircraft. The SAR system has three frequencies – P-band (0.46 GHz), L-band (1.25 GHz), and C-band (5.3 GHz) and with both horizontal and vertical polarizations capability. On the ground, several 8-foot trihedral reflectors were deployed at open area for the purpose of calibration and inside the forest to test the ability of the SAR system to image the objects under the foliage. Also, several "tone generator" (a horn antenna with a signal generator) of P-, L-, and C-band were set up to transmit an electromagnetic wave from inside the forest and this signal was received by the receiver in the airplane to measure the attenuation and phase fluctuation of the field caused by the foliage. During the mission, airborne SAR flew by the test sites with $30°$, $45°$ and $60°$ depression angles. The tone generators at test sites 1, 3, and 4 were obscured by the foliage while the site 2 was a reference site in an open area. The attenuation and the amplitude and phase fluctuation were obtained by averaging the received signals from $-20°$ to $20°$ azimuthal angles of the tone generator mainlobe. The difference of the antenna gain at different azimuthal angles was corrected by comparing with the received single at site 2.

During this experiment, detailed ground truth survey was performed to assist the analysis of the measurement data [MIT/LL, 1990]. The Applied Microwave Portable Dielectric Probe (PDP) was used to measure the dielectric constants of the tree

trunks. The average dielectric constants of trees at P, L, and C bands are $15.5+i2.23$, $14.4 + i3.19$, $12.3 + i4.56$, respectively. The moisture content of the soil and tree twigs and leaves were also measured. Near the site of the trihedral reflectors and tone generators, information on the tree species, diameters at breast height (dbh), and total tree height were collected. For the primary branches, the average size and the average inclination angle were estimated. The biomass of the foliage and the trunks as well as the number density of trees were also estimated. The average height of the first live branch was found to be 5.4m, 4.6m and 5.8m for sites 1, 3, and 4, respectively. The average orientation angle of the primary branches is also recorded in the survey of the ground truth. The inclination angle of primary branches is assumed to be uniformly distributed over a range of $20°$ angle centered at the average inclination angle. The average primary branch angle β_1 is between $60°$ and $80°$, $55°$ and $75°$, and $70°$ and $90°$ for sites 1, 3 and 4, respectively. The average inclination angle of small branches and needles are assumed to be $60°$ for all sites. The biomass ratio of primary branches, secondary branches and leaves is assumed to be $4 : 2 : 3$. Under the assumption that the density of trunks, branches and leaves are the same, the number density of the primary branches, secondary branches and needles are calculated for each site using the biomass of trunks, branches and leaves. The parameters used in theoretical simulation are listed in Table 1. The densities of branches and needles listed are in terms of number per unit length of larger scale scatterers.

4.3 METHODOLOGY

In this study, a theoretical model based on the RT theory using a medium of discrete scatterers and a random phase clutter model is developed to simulate the mean attenuation as well as the amplitude and phase fluctuations of the electromagnetic wave propagating through the foliage. The mean field is obtained from the effective field approximation (Foldy's approximation) which is also used in the derivation of extinction matrix in the RT equation [Tsang, et al., 1985]. The attenuation caused by the absorption and the scattering losses is calculated with the optical theorem which relates the total attenuation to the imaginary part of the forward scattered amplitude from scatterers. Assuming that the phase of incoherent scattering field is completely random, the amplitude fluctuation of electromagnetic wave is related to the bistatic scattering coefficients of forests. The average received power, which is directly related to the average attenuation, is calculated from the sum of the power of the mean field and the power of the fluctuation field. The phase fluctuation is derived from the amplitude fluctuation by assuming the phase of the incoherent field is uniformly distributed from $-\pi$ to π.

The configuration of the problem is shown in Figure 1, where a source (tone generator) radiates the electromagnetic wave inside the forest, and the signal is received by the antenna on an airplane. Since the ground is outside the mainlobe of the source antenna pattern, the ground effect is ignored in the following theoretical derivation.

Under the discrete scatterer model, the attenuation of the average field is obtained from the sum of the absorption loss caused by the dielectric property of scatterer and the scattering loss caused by the wave which is scattered into other directions by

the scatterer. From the optical theorem, the total attenuation can be related to the imaginary part of the forward scattering amplitude as

$$\sigma_e = \frac{4\pi}{k} Im[f]$$

where σ_e is the extinction cross-section, k is the wave number, f is the forward scattering amplitude and IM stand for the imaginary part.

The average field of the electromagnetic wave propagating through the foliage is then

$$|\langle E_s \rangle|^2 = e^{-\langle n_0 \sigma_e \rangle L} \cdot |E_{ref}|^2 \tag{1}$$

where E_{ref} is the received field without the attenuation caused by the foliage, E_s is the received field after the wave has propagated through the foliage, n_0 is the number density of scatterers per unit volume, L is the path length of the wave propagating through the foliage, and $\langle\ \rangle$ denotes the ensemble average over the size, shape, and orientation distribution of scatterers.

When an electromagnetic wave propagates through a scattering medium, not only is the intensity absorbed, it is also scattered to other directions. Since the phase of scattered field is random, it is the fluctuating part of the electromagnetic field. This fluctuating component is related to the bistatic scattering coefficients. The definition of the bistatic scattering coefficient is

$$\gamma(\theta_s, \phi_s; \theta_i, \phi_i) = \lim_{r \to \infty} \frac{4\pi r^2 \langle |E_{sf}(\theta_s, \phi_s)|^2 \rangle}{A \cos\theta_i |E_i(\theta_i, \phi_i)|^2} \tag{2}$$

where E_{sf} is the incoherent scattered field, E_i is the incident field, A is the area of illumination, and r is the distance between the target and the receiver. To obtain the fluctuation of the electromagnetic field, it is assumed that both the incident and scattered fields are plane waves. This assumption may be of limited validity because

of the finite distance between the transmitter and the scatterers inside the forest. Under this assumption, equation (2) can be approximated as

$$\frac{\langle |E_{sf}|^2 \rangle}{|E_i|^2} \approx \frac{A \cos\theta_i}{4\pi r^2} \gamma(\theta_s, \phi_s; \theta_i, \phi_i) \tag{3}$$

Since the beamwidth of the transmitted antenna is very broad, the total incoherent intensity is calculated by integrating the whole area of illumination. From the relationship between the reference field E_{ref} and the incident field E_i, $|E_i| = |E_0|\, G(s)/r_s^2 = |E_{ref}| \cdot G(s)/G_0 \cdot r^2/r_s^2$, the total fluctuation intensity can be obtained from equation (2) as

$$\begin{aligned} \frac{\langle |E_{sf}|^2 \rangle}{|E_{ref}|^2} &\approx \int\int_A \cos\theta_i \frac{\gamma(s)}{4\pi r_s^2} \frac{G(s)}{G_0} ds \\ &= \int_0^{\pi} d\theta_i \sin\theta_i \int_0^{2\pi} d\phi_i \frac{\gamma(\theta_s, \phi_s; \theta_i, \phi_i)}{4\pi} \frac{G(\theta_i, \phi_i)}{G_0} \end{aligned} \tag{4}$$

where the relationship of $ds = r_s^2 \tan\theta_i d\theta_i d\phi_i$ is used. E_0 is the field from the source, r_s is the distance between the source and the scattering medium (here it is assumed that the source is under the medium although it is on the boundary). G is the antenna pattern of the transmitter and G_0 is the gain of the antenna pattern in (θ_i, ϕ_i) direction. In this study, the far field pattern of a horn antenna is used although the trees are in general not in the far field of the tone generator.

Assuming that the phase of the incoherent field is uniformly distributed from $-\pi$ to π

$$E_s = \langle E_s \rangle + E_{sf} = \langle E_s \rangle (1 + \delta e^{i\phi}) \tag{5}$$

where the amplitude fluctuation δ is defined as the square root of the variance of the receiving power normalized by the average receiving power

$$\delta = \sqrt{\frac{\langle |E_{sf}|^2 \rangle}{|\langle E_s \rangle|^2}} = \sqrt{\frac{\langle |E_s|^2 \rangle - |\langle E_s \rangle|^2}{|\langle E_s \rangle|^2}} \tag{6}$$

The phase θ of the scattered field is

$$\theta = \tan^{-1}\left(\frac{\delta \sin\phi}{1+\delta\cos\phi}\right) \tag{7}$$

The phase fluctuation can be obtained from the amplitude fluctuation by averaging over ϕ as

$$\sqrt{\langle\theta^2\rangle} = \sqrt{\frac{1}{2\pi}\int_{-\pi}^{\pi}\theta^2 d\phi} = \sqrt{\frac{1}{2\pi}}\sqrt{\int_{-\pi}^{\pi} d\phi[\tan^{-1}\left(\frac{\delta\sin\phi}{1+\delta\cos\phi}\right)]^2} \tag{8}$$

The average attenuation is defined as the average of the received power with a source under the foliage compared with the received power with a source in free space

$$\frac{\langle|E_s|^2\rangle}{|E_{ref}|^2} = \frac{\langle|\langle E_s\rangle + E_{sf}|^2\rangle}{|E_{ref}|^2} = \frac{|\langle E_s\rangle|^2 + \langle|E_{sf}|^2\rangle}{|E_{ref}|^2} = e^{-\langle n_0\sigma_e\rangle L}\cdot(1+\delta^2) \tag{9}$$

It is noted that no clutter statistics is assumed in this formulation. If the fluctuation of the receiving power is of concern, the Gaussian or K-distribution statistics can be used [Jao, 1984].

4.4 RADIATIVE TRANSFER MODEL OF FOREST

Forest is modeled as a multi-layer random medium which includes a crown layer, a trunk layer, a bush layer, and an underline random rough soil surface as shown in Figure 2. The crown layer is consisted of a tree bole, the primary branches, the secondary branches and the attached leaves. The trunk layer includes the vertical trunk only. The short vegetation presented in the forest is modeled as randomly distributed twigs and leaves inside the bush layer. The half-space soil surface is considered to be randomly rough with Gaussian statistics. The trunks, branches and coniferous leaves are modeled as dielectric circular cylinders where the finite cylinder approximation is used to calculate the scattering response. The deciduous leaves are modeled as elliptical circular disks where the physical optics approximation is used to compute the scattering. The orientation of trees are considered to be uniformly distributed from vertical to the maximum trunk tilted angle. As shown in Figure 2, the orientation of each element is described by its relation to the next bigger scale element. The azimuthal angle of each smaller scatterer to the larger elements is uniformly distributed between -180° and 180°.

The scattering from the forest is formulated with the radiative transfer theory. The vector radiative transfer equation for the specific intensity in each scattering region is of the form

$$\cos\theta \frac{d\bar{I}(\theta,\phi,z)}{dz} = -\bar{\bar{\kappa}}_e(\theta,\phi,z)\cdot\bar{I}(\theta,\phi,z) + \int_{4\pi} d\Omega' \bar{\bar{P}}(\theta,\phi;\theta',\phi')\cdot\bar{I}(\theta',\phi',z) \tag{9}$$

where $\bar{\bar{\kappa}}_e$ is the extinction matrix, $\bar{\bar{P}}$ is the phase matrix which describes the scattering of specific intensity from one direction into another direction. The specific

intensity $\bar{I}$ containing information regarding field intensity and phase relation of the two orthogonal polarizations is defined as

$$\bar{I} = \begin{pmatrix} I_h \\ I_v \\ U \\ V \end{pmatrix} = \frac{1}{\eta} \begin{pmatrix} \langle |E_h|^2 \rangle \\ \langle |E_v|^2 \rangle \\ 2\,\mathrm{Re}\langle E_v E_h^* \rangle \\ 2\,\mathrm{Im}\langle E_v E_h^* \rangle \end{pmatrix} \tag{10}$$

the subscripts h and v represent the horizontal and vertical polarizations, respectively. The angular bracket $\langle\ \rangle$ denotes ensemble average over the size and orientation distributions of scatterers, and $\eta = \sqrt{\mu_0/\epsilon_0}$ is the free-space characteristic impedance. From the RT equation (9), the specific intensity is attenuated when propagating inside the medium, and is enhanced by the intensity from other directions which are scattered into the direction of interest. The extinction matrix $\bar{\bar{\kappa}}_e$ represents the attenuation caused by both the scattering and absorption losses, and can be obtained through the optical theorem in terms of the forward scattering function. The phase matrix $\bar{\bar{P}}(\theta, \phi; \theta', \phi')$ characterizes the scattering of the Stokes vector from (θ', ϕ') direction into (θ, ϕ) direction and can be formulated in terms of scattering functions of the randomly distributed discrete scatterers.

For forests, trees only constitute a small fraction of the total volume (usually less than 1 %), so the effective permittivity is very close to that of free space. Therefore it is assumed that the reflection between different layers can be neglected except at the bottom soil interface. Along with the appropriate boundary conditions, we can solve the radiative transfer equations iteratively to obtain the bistatic scattering coefficients [Tsang et al., 1985]. The resulting bistatic coefficients are the incoherent intensities which are related to the fluctuating part of electromagnetic wave.

4.5 COMPARISON OF THEORETICAL SIMULATION AND MEASUREMENT DATA

With the collected ground truth information about the average sizes of the trunks and branches and the number density of the trees instead of information for each individual tree, the proposed RT model is applied to simulate the average attenuation and phase fluctuations for different sites. The first-order iterative solution, which only includes single scattering, is used in calculating the fluctuation field. The statistical results of the one way attenuations for P, L and C bands are shown in Figure 3. The horizontal axis represents the measured attenuation averaged over azimuthal angles for 3 depression angles at 3 test sites, and the vertical axis is the result of average attenuation from the theoretical calculation. The two straight lines indicate the bound of 2 dB difference between the measured and calculated attenuations. It shows that in general, the attenuation is higher at higher frequencies. Also, at P-band the vertical polarization tends to attenuate more than the horizontal polarization does because the vertical trunks have more effect on vertical polarization at low frequencies. The difference between the theoretical result and the measurement is within 2 dB for most cases at P and L bands. As the attenuation becomes larger, the difference between the measurement and prediction tends to be larger. The finite samples of the measurements and the positions of the tone generators would also affect the measured attenuation.

Based on the theoretical calculations, it is found that the attenuation at different frequencies is caused by different components of trees. The contribution of the trunks, branches and leaves to the total attenuation for site 1 is shown in Figures 4 to 6 for the frequencies of P-, L-, and C-bands. The vertical axis is the magnitude of the

average complex received field (from equation 1) normalized with the magnitude of the received field in free space. The horizontal axis is the observation angles in degree. The normalized field indicates how much the field is attenuated caused by scatterers. The uppermost curve is the attenuation caused by the trunks only. The next curve is the attenuation caused by the trunks and the primary branches. The third curve is the attenuation caused by the trunks and the primary and secondary branches. The bottom curve includes the effects of all scatterers. From Figure 4, it is shown that the dominant scatterers contributing to the attenuation at P-band vertical polarization are the trunks while for horizontal polarization the attenuation from primary branches is also important. As shown in Figure 5, for the L-band, the trunks and the primary branches are the main contributors to the attenuation. The large attenuation of horizontal polarization caused by the primary branches is because most of the large branches are more horizontal. At C-band the attenuation is mainly caused by the leaves and the small branches as shown in Figure 6.

The polarization and depression angle dependencies are also illustrated in Figure 4 to 6. As the depression angle decreases, the path length of the wave propagating through the foliage increases, so the attenuation increases. At P band, because the main contribution to the attenuation is from vertical trunks, the vertically polarized field attenuates much more than horizontally polarized field. The difference between the two polarizations is smaller at C band since the main scatterers (the leaves and the small branches) are almost randomly orientated. These polarization dependencies are also observed from the measured data as shown in Figure 3.

Using the bistatic scattering coefficients calculated from the RT theory and with the assumption of random phase on the incoherent scattering field, the phase fluctuation can be calculated as shown in the Section 5.3. The measured phase fluctuation

at P and L bands are shown in Figure 7. The theoretical simulation is shown in figure 8. The horizontal axis is the one-way attenuation and the vertical axis is the phase fluctuation. Based on the theoretical calculation, it is shown that as the attenuation increases, the phase fluctuation also increases. The correlation between the measured attenuation and phase fluctuation is not as clear as in the theoretical calculation but still shows the same trend. Also from both the measured data and theoretical calculation, the vertically polarized field shows larger phase fluctuation than the horizontally polarized field with the same attenuation. Since the attenuation is resulted from both the scattering loss and absorption loss whereas the fluctuation is mainly from the scattering, this phenomenon can be explained by noting that the vertical polarized field has higher ratio of scattering loss to the total attenuation.

4.6 CONCLUSION

In this chapter, the attenuation and phase fluctuations of electromagnetic waves propagating through the foliage is investigated with a theoretical model. These fluctuations are important in determining how well an object obscured by the foliage can be imaged with a synthetic aperture radar. The bistatic scattering coefficient and mean attenuation are calculated using the radiative transfer theory with the discrete scatterer model. The phase fluctuation is obtained from the amplitude fluctuation assuming that the phase of the fluctuation field is uniformly distributed between $-\pi$ and π. The average received power is obtained from the sum of the power of the average field and the power of the fluctuation field. The attenuation is then obtained by comparing the radiated power from a source under the foliage to the received power from a source in free space. The theoretical results are compared with experimental data collected by MIT Lincoln Laboratory during the 1990 Foliage Penetration Experiment. In the experiment, transmitters were placed inside the forest and an airborne receiver was used to measure the one-way propagation. The one-way attenuation and phase fluctuation caused by the foliage are obtained by comparing the radiated field from tone generators under the foliage with those in the open space.

The theoretical model is used to illustrate the frequency, polarization and angular dependencies of the attenuation and phase fluctuations. It is found that the vertical polarized attenuation is higher than the attenuation for the horizontal polarization at P-band because of the contribution from the trunk. The polarization dependence at L- and C-bands is found to be small. The increase of attenuation with frequency and incident angle and the contribution of different scatterers is investigated using the developed theoretical model. With this proposed model, it is also possible to

examine the attenuation and phase fluctuation for different tree moisture contents, tree types and forest densities.

	trunk			primary branch			small branch			needle		
site	radius (cm)	length (m)	density (m^{-2})	radius (cm)	length (m)	density (m^{-1})	radius (cm)	length (cm)	density (m^{-1})	radius (cm)	length (cm)	density (m^{-1})
1	8.8	9.4	0.22	1.1	1.2	12.2	0.4	50	7.65	0.1	5	480
3	12.4	8.8	0.17	1.5	0.8	11.66	0.4	50	13.88	0.1	5	480
4	8.76	8.45	0.17	1.35	1.0	8.87	0.4	50	11.4	0.1	5	480

Table 1 Table of the Parameters

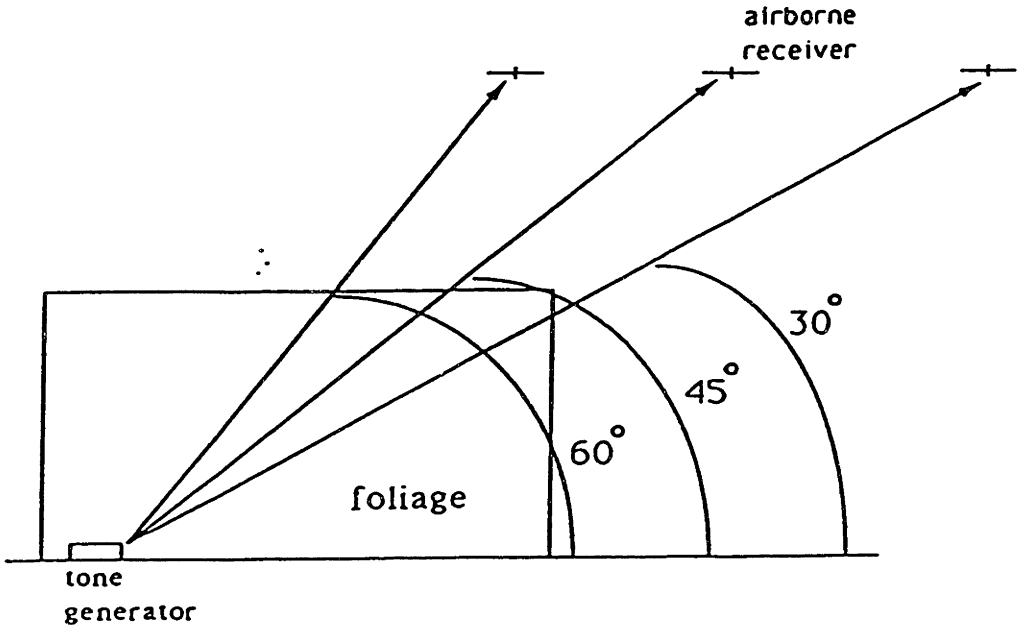

Figure 1 Configuration of the Problem

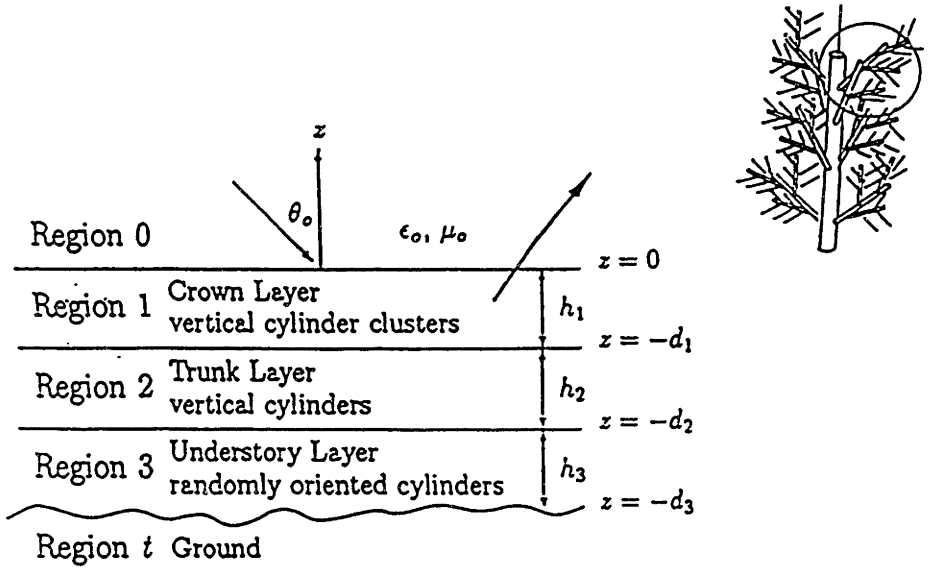

Figure 2 Forest Model

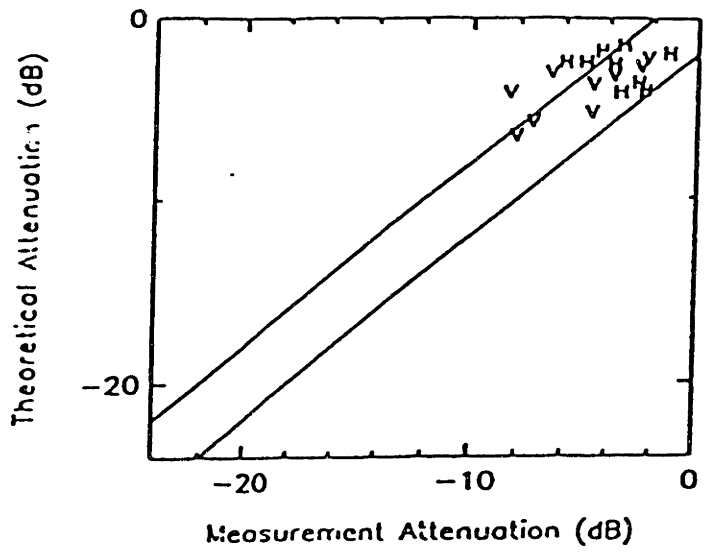

Figure 3 (a) Comparison of Measured and Simulated One-way Attenuation at P-band

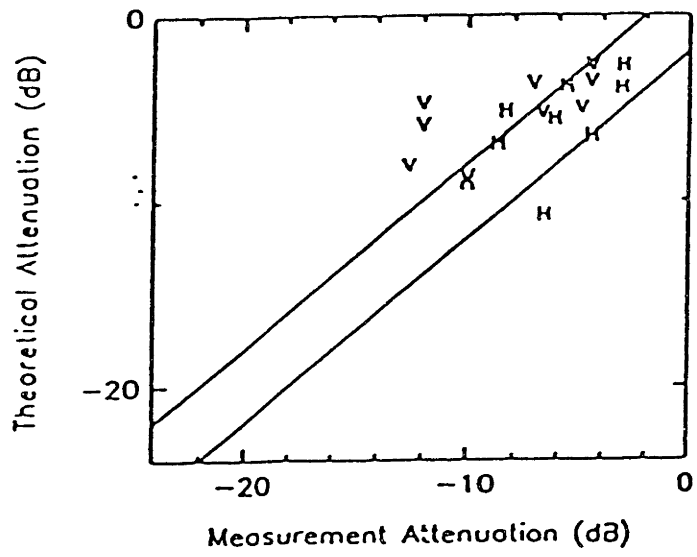

Figure 3 (b) Comparison of Measured and Simulated One-way Attenuation at L-band

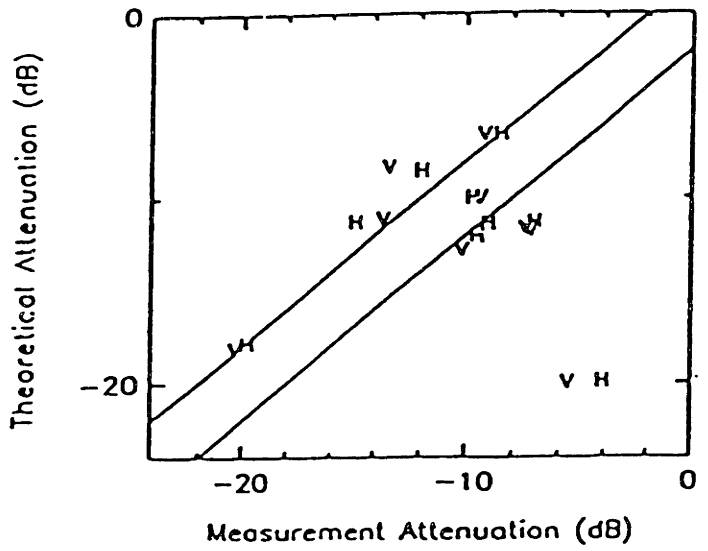

Figure 3 (c) Comparison of Measured and Simulated One-way Attenuation at C-band

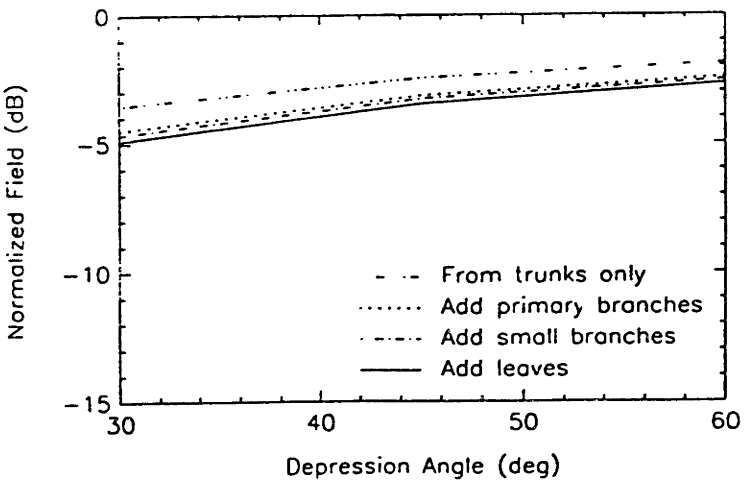

Figure 4 (a) Contribution of One-way H-pol. Attenuation at P band

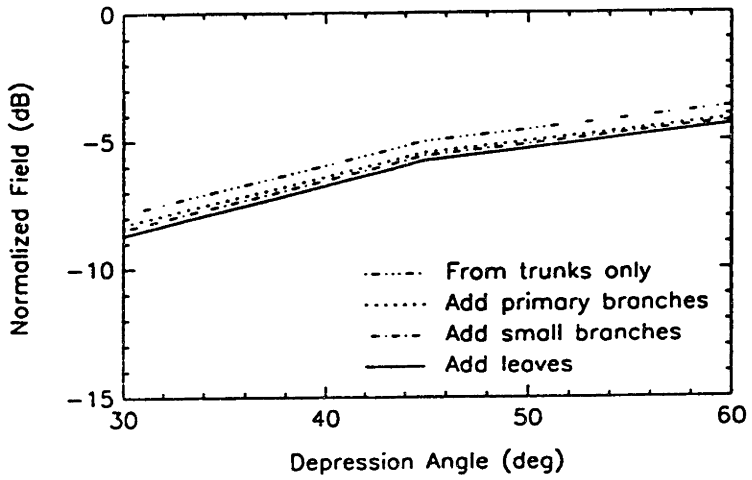

Figure 4 (b) Contribution of One-way V-pol. Attenuation at P band

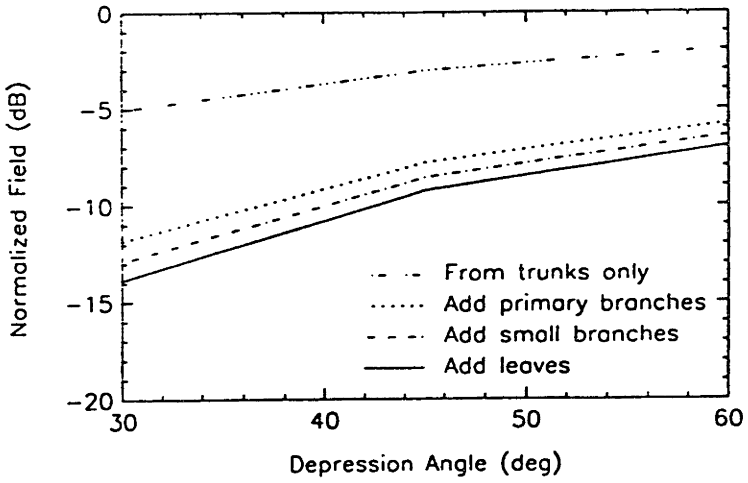

Figure 5 (a) Contribution of One-way H-pol. Attenuation at L band

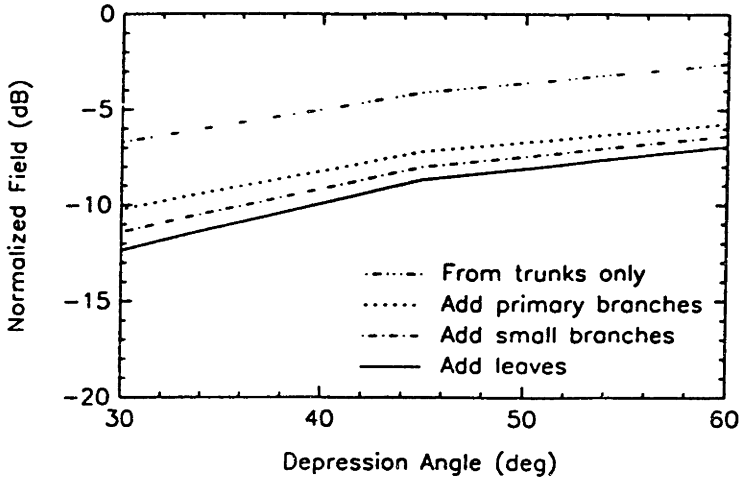

Figure 5 (b) Contribution of One-way V-pol. Attenuation at L band

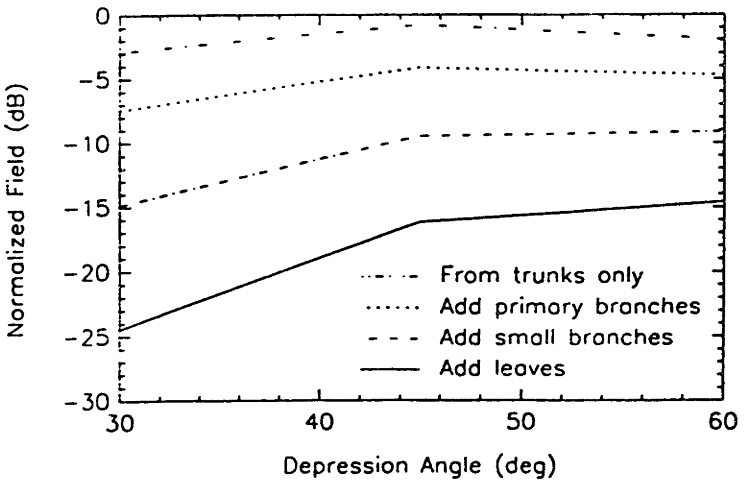

Figure 6 (a) Contribution of One-way H-pol. Attenuation at C band

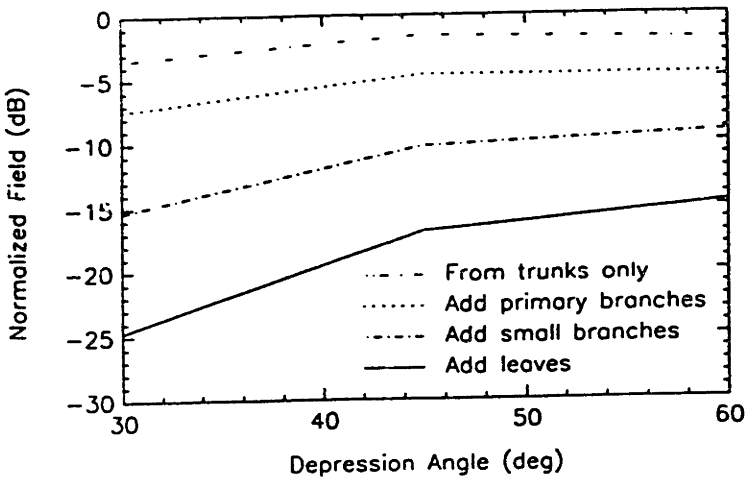

Figure 6 (b) Contribution of One-way H-pol. Attenuation at C band

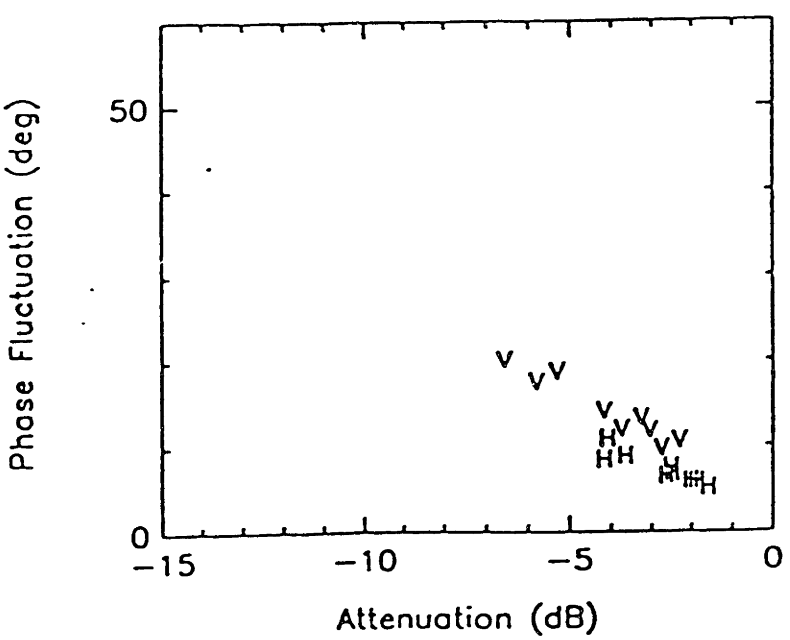

Figure 7 (a) Measured One-way Attenuation and Phase Fluctuation at P band

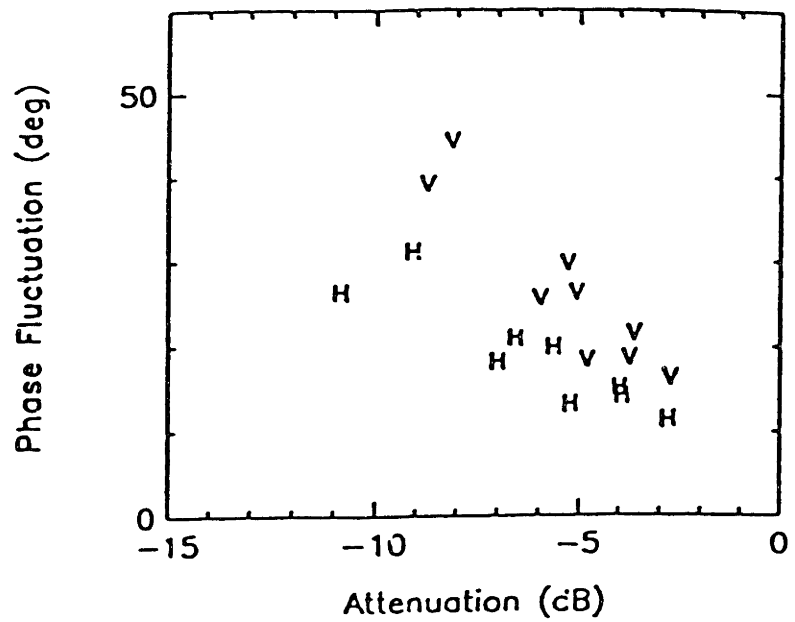

Figure 7 (b) Measured One-way Attenuation and Phase Fluctuation at L band

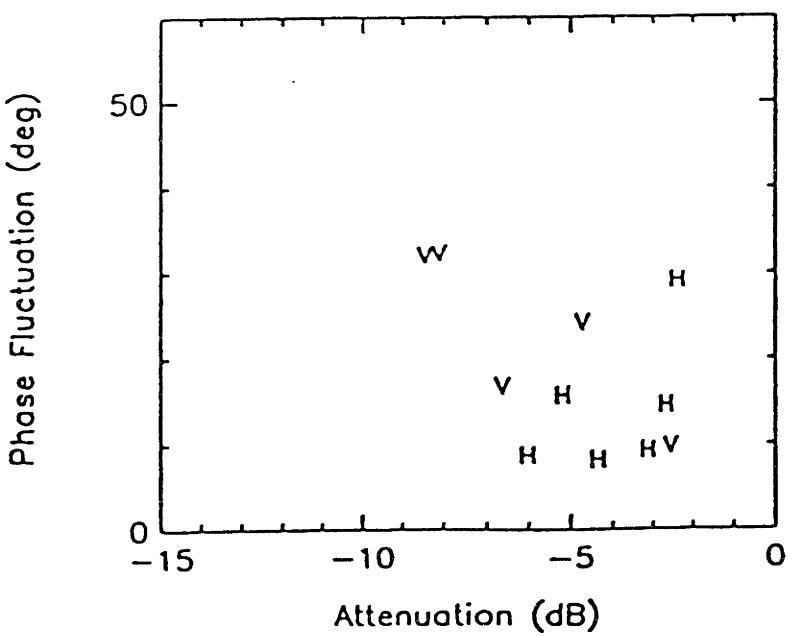

Figure 8 (a) Simulated One-way Phase Fluctuation at P band

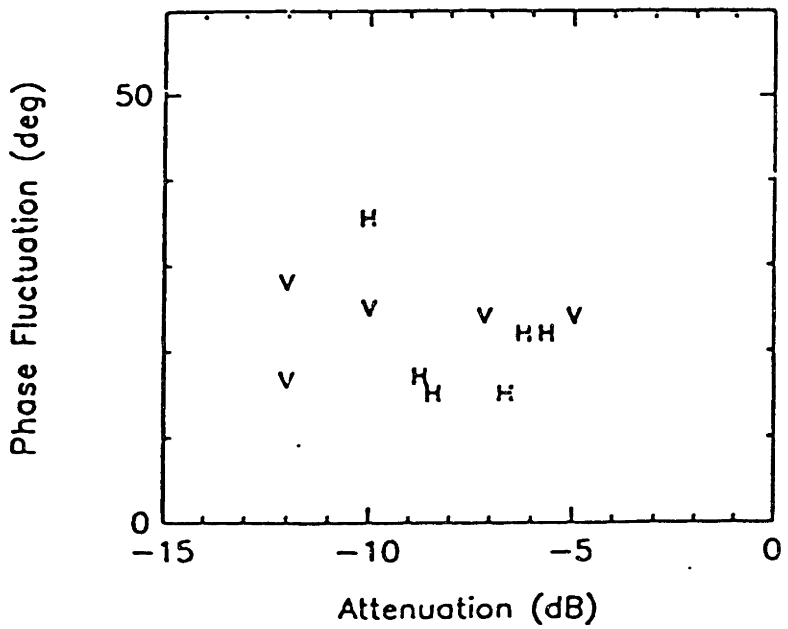

Figure 8 (b) Simulated One-way Phase Fluctuation at L band

Chapter 5.

Polarimetric Passive Remote Sensing of Vegetation

ABSTRACT – The polarimetric brightness temperature is calculated with radiative transfer (RT) formulation, either solved directly from the RT equation with source term included or calculated with Kirchhoff's law from the bistatic scattering coefficients. The theoretical model is used to interpret the measured emissions from alfalfa field for different growth stages at 10 GHz. Polarimetric emission from non azimuthally symmetrical media with tilted scatterers is investigated theoretically.

5.1 INTRODUCTION

The passive remote sensing has long history. Astrophysicist use radiometers to measure the radiation from the extraterrestrial stars. The microwave radiometers have been used in the remote sensing of atmosphere as well as applied to the detection of sea ice coverage, soil moisture and sea state (wind speed). Compared with the radar images, brightness temperature maps do not have the problem of speckle and the passive equipments are usually very sensitive and stable. Although usually the passive remote sensing has low resolution, recently, the Synthetic Aperture technology has been used in the development of Electronically Scanned Thinned Array Radiometer

(ESTAR) to achieve higher resolution. [Le Vine et al., 1994] With higher resolution, the non-azimuthal symmetry property of the earth terrain would be more important.

It is commonly known that all four Stokes parameters emission from non azimuthally symmetrical medium is generally non-zero. However, the earth medium is commonly assumed to have azimuthal symmetry property. It was first suggested by Tsang [1991] that all four Stokes parameters emission from earth terrain with non-azimuthal symmetric property would be significantly different from zero. Emission from periodic soil surface has been studied experimentally [Nghiem, et al., 1991] and theoretically [Veysoglu, et al., 1991]. The numerical results indicated that the plowed field would has the third Stokes parameter (U) as high as $40K$. There are also studies looking into the application to the ocean surface which relates the U to the wind speed. Several studies with periodic water surfaces [Johnson, et al., 1994, Yueh, et al., 1994] have prompted an experiment on thermal emission from ocean surface [Yueh, et al., 1995]. It's been shown that the third Stokes parameter U can reveal wind direction caused by the azimuthal asymmetry of ocean surface. Although some works have been done regarding the applications of polarimetric emission from surface, very few studies investigated the effect of azimuthal non-symmetry on volume scattering and its applications on the parameter retrieval.

In the application of the radiative transfer theory to the remote sensing of earth terrain, the medium properties are considered in the phase matrix, the extinction matrix, and the absorption vector in the RT equation. In this study, the continuous random medium model as well as the discrete scatterer model are used to characterize the vegetation layer and to account for the volume scattering effects. For the continuous random medium model, the random medium is realized with a correlation function involving variance and correlation lengths. The correlation function

of the randomly fluctuating permittivity function is assumed to be exponential and has different correlation lengths in the lateral and vertical directions. The effective permittivities of the vegetation layer and the extinction and scattering properties of the random medium are obtained under strong fluctuation theory and the continuous random medium approach. [Yueh, et al., 1990] The rough surface scattering effect is incorporated by modifying the boundary conditions of RT equation using the Kirchhoff's approximation. The first order iterative solution to the RT equation is then used to calculate the emission and backscattering from the vegetation canopy.

In this work, we will study the polarimetric emission from the volume scattering using RT formulation. Section 5.2 describes the two methods used to calculate the brightness temperature from a layer random medium. The comparison of theoretical simulation with measurement data is shown in Section 5.3. The third and fourth Stokes parameters from a non azimuthally symmetrical medium are investigated in Section 5.4. Part of this work has been published with the cooperation of the Istituto di Ricerca sulle Onde Elettromagnetiche (IROE) and the Centre d'Etude Spatiale BIOsphere (CESBIO) [Hsu, et al., 1994b].

5.2 RADIATIVE TRANSFER MODEL

For passive remote sensing, the measurable quantities are the brightness temperatures which are related to the Stokes parameters as

$$\overline{T}_B = \begin{pmatrix} T_{Bv} \\ T_{Bh} \\ U_B \\ V_B \end{pmatrix} = \frac{\lambda^2}{k_B}\overline{I} = \frac{\lambda^2}{k_B}\begin{pmatrix} I_v \\ I_h \\ U \\ V \end{pmatrix} \tag{1}$$

where T_{Bh} and T_{Bv} are the brightness temperature of the horizontal and vertical polarizations and the U_B and V_B are related to the correlation between two polarizations. k_B is the Boltzmann's constant. λ is free space wavelength. The Stokes vector $\overline{I}$ containing the information of field intensity and the phase relation of the two orthogonal polarizations and is defined as

$$\overline{I} = \begin{pmatrix} I_v \\ I_h \\ U \\ V \end{pmatrix} = \frac{1}{\eta}\begin{pmatrix} \langle |E_v|^2 \rangle \\ \langle |E_h|^2 \rangle \\ 2\,\mathrm{Re}\langle E_v E_h^* \rangle \\ 2\,\mathrm{Im}\langle E_v E_h^* \rangle \end{pmatrix}$$

where the subscript h represents the horizontal polarization and v the vertical polarization. $\eta = \sqrt{\mu_0/\epsilon_0}$ is the free-space impedance. The angular bracket $\langle\rangle$ denotes ensemble average over configuration.

The third and fourth terms of the Stokes parameters U and V can be obtained by measuring the 45° linear polarized and right-hand circularly polarized brightness temperatures. The 45° linear polarized intensity can be expressed in terms of field of horizontal and vertical polarizations as

$$2\,I_{45} = [\langle (E_h - E_v)\cdot(E_h^* - E_v^*)\rangle]/\eta$$

$$= \langle |E_v|^2 \rangle/\eta + \langle |E_h|^2 \rangle/\eta - 2Re\langle E_v E_h^* \rangle/\eta$$

$$= I_v + I_h - U \tag{2a}$$

The third Stokes parameter can then be expressed as

$$U = I_v + I_h - 2\, I_{45} \tag{2b}$$

The fourth Stokes parameter can be obtained with the same way from the right-hand circular polarized intensity as

$$2\, I_{RC} = [\langle (E_h + iE_v) \cdot (E_h^* - iE_v^*) \rangle]/\eta$$

$$= \langle |E_v|^2 \rangle/\eta + \langle |E_h|^2 \rangle/\eta - 2Im\langle E_v E_h^* \rangle/\eta$$

$$= I_v + I_h - V \tag{3a}$$

$$V = I_v + I_h - 2\, I_{RC} \tag{3b}$$

where I_{45} and I_{RC} are the intensities of 45° linear polarization and right-hand circular polarization, respectively.

Based on the incoherent addition property of the specific intensity, the vector radiative transfer equation for the specific intensity $\overline{I}$ inside the random medium is of the form

$$\begin{aligned} \cos\theta \frac{d\overline{I}(\theta,\phi,z)}{dz} = & -\overline{\overline{\kappa}}_e(\theta,\phi,z) \cdot \overline{I}(\theta,\phi,z) + \overline{F}(\theta,\phi,z)CT \\ & + \int_{4\pi} d\Omega' \overline{\overline{P}}(\theta,\phi;\theta',\phi') \cdot \overline{I}(\theta',\phi',z) \end{aligned} \tag{4}$$

where $\overline{\overline{\kappa}}_e$ is the extinction matrix which describes the attenuation of Stokes vectors in the random medium, $\overline{F}$ is the emission vector, T is physical temperature of the medium, constant $C = k_B/\lambda^2$, k_B is Boltzmann's constant, λ is free space wavelength. The phase matrix $\overline{\overline{P}}$ characterizes the scattering of the Stokes vector from the (θ', ϕ') direction into the (θ, ϕ) direction.

The phase matrix $\overline{\overline{P}}$ is calculated in term of the correlation between scattering function. The extinction matrix $\overline{\overline{\kappa}}_e$ can be calculated from the summation of the absorption loss and scattering loss or be obtained in terms of forward scattering function through the optical theorem as described in Chapter 2.

The emission vector $\overline{F}$ is related to the absorption of the medium and is expressed as

$$\overline{F}(\hat{s}) = \begin{pmatrix} \kappa_{a1}(\hat{s}_b) \\ \kappa_{a2}(\hat{s}_b) \\ -\kappa_{a3}(\hat{s}_b) \\ -\kappa_{a4}(\hat{s}_b) \end{pmatrix} \tag{5}$$

where $\hat{s}$ is in the direction of (θ, ϕ) and $\hat{s}_b = -\hat{s}$ is in the backward direction of $\hat{s}$. The four emission coefficients are calculated from the difference between extinction and total scattering [Tsang 1991] as

$$\kappa_{a1}(\hat{s}_b) = \kappa_{e11}(\hat{s}_b) - \int_{4\pi} d\Omega' [P_{11}(\hat{s}', \hat{s}_b) + P_{21}(\hat{s}', \hat{s}_b)] \tag{6a}$$

$$\kappa_{a2}(\hat{s}_b) = \kappa_{e22}(\hat{s}_b) - \int_{4\pi} d\Omega' [P_{12}(\hat{s}', \hat{s}_b) + P_{22}(\hat{s}', \hat{s}_b)] \tag{6b}$$

$$\kappa_{a3}(\hat{s}_b) = 2\kappa_{e13}(\hat{s}_b) + 2\kappa_{e23}(\hat{s}_b) - 2\int_{4\pi} d\Omega' [P_{13}(\hat{s}', \hat{s}_b) + P_{23}(\hat{s}', \hat{s}_b)] \tag{6c}$$

$$\kappa_{a4}(\hat{s}_b) = -2\kappa_{e14}(\hat{s}_b) - 2\kappa_{e24}(\hat{s}_b) + 2\int_{4\pi} d\Omega' [P_{14}(\hat{s}', \hat{s}_b) + P_{24}(\hat{s}', \hat{s}_b)] \tag{6d}$$

where κ_{eij} is the ij element of the extinction matrix $\overline{\overline{\kappa}}_e$ and P_{ij} is the ij element of the phase matrix $\overline{\overline{P}}$.

The boundary between vegetation and ground is modelled as an irregular interface of Gaussian statistics on both surface height and correlation function. The scattering and emission from the rough surface is evaluated with the Kirchhoff approximation. The boundary between air and vegetation is ignored since the fractional

volume of vegetation is small. With appropriate boundary conditions, the radiative transfer equation is solved to obtain the all four Stoke's parameters. Alternatively, the emission can be calculated from the bistatic scattering coefficients using the Kirchhoff's law. In this study, both methods are used.

5.2.1 Calculation of emission from bistatic scattering coefficients

The emission from passive remote sensing can be related to the bistatic scattering coefficients in active remote sensing with the use of the energy conservation. Considering an electromagnetic wave of polarization α incident on a medium, the medium absorbs some energy and scattered the other portion of the energy into the upper atmosphere. The absorptivity a can be express as the difference between incident power and scattered power

$$a_\alpha(\theta_i,\phi_i) = 1 - \frac{1}{4\pi}\sum_{\beta=v,h}\int_0^{\pi/2} d\theta_s \sin\theta_s \int_0^{2\pi} d\phi_s \gamma_{\beta\alpha}(\theta_s,\phi_s;\theta_i,\phi_i) \qquad (7)$$

where γ is the bistatic scattering coefficient.

With the use of the Kirchhoff's law, the energy absorbed by the medium will be re-radiate with the same amount under the equilibrium condition, the brightness temperature can be expressed as

$$T_{Bv}(\hat{s}_0) = T\,[1 - \frac{1}{4\pi}\sum_{\alpha=v,h}\int_{\hat{s}\cdot\hat{z}>0} d\Omega\ \ \gamma_{\alpha v}(\hat{s},\hat{s}_{0b})] \qquad (7a)$$

$$T_{Bh}(\hat{s}_0) = T\,[1 - \frac{1}{4\pi}\sum_{\alpha=v,h}\int_{\hat{s}\cdot\hat{z}>0} d\Omega\ \ \gamma_{\alpha h}(\hat{s},\hat{s}_{0b})] \qquad (7b)$$

$$U_B(\hat{s}_0) = T_{Bv}(\hat{s}_0) + T_{Bh}(\hat{s}_0) - 2T\,[1 - \frac{1}{4\pi}\sum_{\alpha=v,h}\int_{\hat{s}\cdot\hat{z}>0} d\Omega\ \ \gamma_{\alpha P}(\hat{s},\hat{s}_{0b})] \qquad (7c)$$

$$V_B(\hat{s}_0) = T_{Bv}(\hat{s}_0) + T_{Bh}(\hat{s}_0) - 2T\,[1 - \frac{1}{4\pi}\sum_{\alpha=v,h}\int_{\hat{s}\cdot\hat{z}>0} d\Omega\ \ \gamma_{\alpha R}(\hat{s},\hat{s}_{0b})] \qquad (7d)$$

where $\hat{s}_0$ is the direction of thermal emission.

5.2.2 Direct Calculation of emission from RT equation

The radiative transfer equation as expressed in equation (1) can be solved directly to obtain the emission. Follow the same procedure as in chapter two, first the upgoing and downgoing waves are separated by restricting $0 < \theta < \pi/2$. This leads to the following two coupled equations

$$\cos\theta \frac{d}{dz}\bar{I}_n(\theta,\phi,z) = -\bar{\bar{K}}_e(\theta,\phi)\cdot\bar{I}_n(\theta,\phi,z) + \bar{F}(\theta,\phi)CT(z) + \bar{S}_n(\theta,\phi,z) \tag{8a}$$

$$-\cos\theta \frac{d}{dz}\bar{I}_n(\pi-\theta,\phi,z) = -\bar{\bar{K}}_e(\pi-\theta,\phi)\cdot\bar{I}_n(\pi-\theta,\phi,z) + \bar{F}(\pi-\theta,\phi)CT(z) + \bar{W}_n(\pi-\theta,\phi,z) \tag{8b}$$

where $\bar{I}_n(\theta,\phi,z)$ and $\bar{I}_n(\pi-\theta,\phi,z)$ are the upgoing and the downgoing specific intensities in the n-th layer. The two source terms $\bar{S}_n(\theta,\phi,z)$ and $\bar{W}_n(\pi-\theta,\phi,z)$ account for the scattering effects and hence include the coupling of specific intensities between the upgoing and the downgoing waves.

$$\bar{S}_n(\theta,\phi,z) = \int_0^{2\pi} d\phi' \int_0^{\frac{\pi}{2}} d\theta' sin\theta' \Big[\bar{\bar{P}}_n(\theta,\phi;\theta',\phi')\cdot\bar{I}_n(\theta',\phi',z) + \bar{\bar{P}}_n(\theta,\phi;\pi-\theta',\phi')\cdot\bar{I}_n(\pi-\theta',\phi',z) \Big] \tag{9a}$$

$$\bar{W}_n(\pi-\theta,\phi,z) = \int_0^{2\pi} d\phi' \int_0^{\frac{\pi}{2}} d\theta' sin\theta' \Big[\bar{\bar{P}}_n(\pi-\theta,\phi;\theta',\phi')\cdot\bar{I}_n(\theta',\phi',z) + \bar{\bar{P}}_n(\pi-\theta,\phi;\pi-\theta',\phi')\cdot\bar{I}_n(\pi-\theta',\phi',z) \Big] \tag{9b}$$

Using the diffusive boundary condition at the upper boundary ($z = -d_{n-1}$) of each layer, we let the specific intensity of the downgoing wave to be zero and ignore the reflections at the interface between regions n and $n-1$. This is a good approximation for sparse medium where the effective permittivity is very close to that of background and there is no coupling between upgoing and downgoing intensities at interface between layers. At the bottom boundary ($z = -d_N$), the coupling matrix is evaluated using the Fresnel reflection coefficients for flat ground and the Kirchhoff's

approximation or SPM for the random rough surface. Hence the boundary conditions can be written as

$$\begin{aligned}
\overline{I}_1(\pi-\theta,\phi,z=0) =& 0 \\
\overline{I}_N(\theta,\phi,z=-d) =& \overline{I}_g(\theta,\phi) \\
&+\int_0^{2\pi} d\phi' \int_0^{\frac{\pi}{2}} d\theta' sin\theta' \overline{\overline{R}}_N(\theta,\phi;\theta',\phi') \cdot \overline{I}_N(\pi-\theta',\phi',z=-d_N) \\
\overline{I}_n(\theta,\phi,z=-d_n) =& \overline{I}_{n+1}(\theta,\phi,z=-d_n) \\
\overline{I}_n(\pi-\theta,\phi,z=-d_{n-1}) =& \overline{I}_{n-1}(\pi-\theta,\phi,z=-d_{n-1})
\end{aligned} \tag{10}$$

where $n = 2,3,4.....N-1$. $\overline{I}_g$ is the emission from the ground and is expressed as

$$\overline{I}_g(\theta,\phi) = \int_0^{2\pi} d\phi' \int_0^{2\pi} d\theta' \sin\theta' \overline{\overline{T}}(\theta,\phi;\theta',\phi') \begin{pmatrix} C_g T_g \\ C_g T_g \\ 0 \\ 0 \end{pmatrix}$$

where $C_g = (\frac{\epsilon_g}{\epsilon_0})\frac{k_B}{\lambda^2}$. $\overline{\overline{T}}$ is the transmission matrix of the underline rough surface.

The iterative solution of the RT equation is obtained with the source terms $\overline{S}$ and $\overline{W}$ as the perturbation for each iteration. As the first two terms on the right-hand side of (8) are the dominant terms, we can obtain the zeroth-order solution by ignoring $\overline{S}$ and $\overline{W}$. By substituting the zeroth-order solutions into $\overline{S}$ and $\overline{W}$ of (8) we then obtain the first-order solutions. Higher order solutions can be readily obtained by following this scheme. With the same procedure discussed in Chapter 2, the zeroth order solutions are expressed as

$$\begin{aligned}
\overline{I}_n^{(0)}(\theta,\phi,z) =& \overline{\overline{E}}_n \overline{\overline{D}}_n(-\beta_n(\theta,\phi)\sec\theta(z+d_n))\overline{\overline{E}}_n^{-1} \cdot \overline{I}_{n+1}^{(0)}(\theta,\phi,-d_n) \\
&+\sec\theta \int_{-d_n}^{z} dz' \overline{\overline{E}}_n \overline{\overline{D}}(\beta_n(\theta,\phi)\sec\theta(z'-z))\overline{\overline{E}}_n^{-1} \overline{F}_n(\theta,\phi) \cdot CT(z')
\end{aligned} \tag{11a}$$

$$\begin{aligned}
\overline{I}_n^{(0)}(\pi-\theta,\phi,z) =& \overline{\overline{E}}_n \overline{\overline{D}}_n(\beta_n(\pi-\theta,\phi)\sec\theta(z+d_{n-1}))\overline{\overline{E}}_n^{-1} \overline{I}_{n-1}^{(0)}(\pi-\theta,\phi,-d_{n-1}) \\
+\sec\theta \int_z^{-d_{n-1}} dz' \overline{\overline{E}}_n \overline{\overline{D}}_n(\beta(\pi-\theta,\phi)\sec\theta(z-z'))\overline{\overline{E}}^{-1} \cdot \overline{F}_n(\pi-\theta,\phi) \cdot CT(z')
\end{aligned} \tag{11b}$$

here $\overline{\overline{G}}_n = \overline{\overline{E}}_n \overline{\overline{D}}_n \overline{\overline{E}}_n^{-1}$ is the propagation operator.

Combine with the above equations with boundary conditions in equation (10), the zeroth order solution in the region above the random medium is

$$\begin{aligned}
\overline{I}_1^{(0)}(\theta,\phi,z) = & \prod_{n=1}^{N} \overline{\overline{G}}_n(-\beta_n(\theta,\phi)\sec\theta d_n)\cdot \overline{I}_g(\theta,\phi) \\
& + \prod_{m=1}^{n-1} \overline{\overline{G}}_m(-\beta_m(\theta,\phi)\sec\theta d_m)\cdot \prod_{m=n+1}^{N} \overline{\overline{G}}_m(-\beta_m(\theta,\phi)\sec\theta d_m) \\
& \cdot \sec\theta \int_{-d_n}^{-d_{n-1}} dz' \overline{\overline{G}}_n(\beta_n(\theta,\phi)\sec\theta(z'+d_{n-1}))\cdot \overline{F}_n(\theta,phi)CT(z') \\
& + \prod_{n=1}^{N} \overline{\overline{G}}_n(-\beta_n(\theta,\phi)\sec\theta d_n)\cdot \int d\Omega' \overline{\overline{R}}_N(\theta,\phi;\theta',\phi')\cdot \\
& \sum_{n=1}^{N}\{\prod_{m=1}^{n-1} \overline{\overline{G}}_m(-\beta_n(\theta,\phi)\sec\theta d_m)\cdot \prod_{m=1}^{n-1} \overline{\overline{G}}_m(-\beta_m(\theta,\phi)\sec\theta d_m) \\
& \cdot \sec\theta \int_{-d_n}^{-d_{n-1}} dz' \overline{\overline{G}}_n(\beta_n(\theta,\phi)\sec\theta(-d_n-z'))\overline{F}_n(\pi-\theta,\phi)\cdot CT(z')\}
\end{aligned} \tag{12}$$

The first term of (12) is the emission from the ground, the second term is the emission from the scatterers inside the medium. The third term is the emission from the scatterers and reflected from the ground as shown in Figure 1.

To derive the first-order solution, first we should calculate the source terms $\overline{S}$ and $\overline{W}$ by substituting $\overline{I}_n^{(0)}(\theta,\phi,z)$ and $\overline{I}_n^{(0)}(\pi-\theta,\phi,z)$ into the equation (9) and the two source terms are treated as constant to obtain the first-order solution. The first order solution represents the emission is scattered once before reaching the radiometer. It includes the emission from the ground and scattered from the scatterers and emission from scatterers and scattered from other scatterers and/or reflected from ground as shown in Figure 2.

To check the accuracy of the iterative solution, the emission from a layer of cylindrical scatterers with fractional volume of 0.02% is studied. The physical temperature is 300 K, and the cylinder is 45° tilted toward the x-axis. The height of layer is

$2.5m$ and the radius and length of cylinder are $0.1cm$ and $0.5m$, respectively. The dielectric constant of the cylinder is (24.2,7.3). The frequency of the radiometer is 1.25 GHz. The simulated brightness temperatures of horizontal polarization using the direct method and Kirchhoff's law with the first-order iterative solution are shown in Figure 3(a). The horizontal axis is the azimuthal angle where the elevation angle is fixed at $30°$. $0°$ azimuthal angle corresponds to the direction of x-axis. The vertical axis is the brightness temperature. It shows that the results from two methods for this case are very close. As shown in the Figure, the emission from $90°$ and $270°$ are higher because of the orientation of cylinders at these two azimuthal angles emit more horizontally polarized energy. The vertically polarized brightness temperature is shown in Figure 3(b) where the brightness temperatures are higher at $0°$ and $180°$. Also note that the calculation of horizontal and vertical brightness temperatures from Kirchhoff's law are always higher than those of direct calculation. This is because, by ignoring the higher order terms, the direct calculation underestimates the return while the calculation using bistatic scattering coefficients overestimates the return. The above statement is true for linearly polarized and circularly polarized emissivities but it does not hold for U_B and V_B because these two are derived quantities. The difference of the numerical results from these two formulations is larger for vertical polarization because the albedo (ratio of total scattering and extinction) for vertical polarization is higher for this case. The emitted U_B and V_B are shown in Figure 3(c) and 3(d). It shows that at $45°$ and $135°$ there are higher emission for the third and fourth Stokes parameters emission.

The numerical results for vertically polarized brightness temperature for a layer of cylinders with fractional volume of 0.1% are shown in Figure 4 (a). The difference between the numerical results from these two formulations is larger because the larger optical thickness with the higher fractional volume. The third Stokes parameter brightness temperature is larger for the higher fractional volume as shown in Figure 4 (b). It is shown from Figures 3 and 4 that the first-order iterative solution gives a good estimation of the brightness temperature for these cases.

5.3 COMPARISON WITH EXPERIMENTAL DATA

Thermal emission from alfalfa crop in different development stages was measured by IROE with ground based radiometers at 10 GHz, 36 GHz (horizontal and vertical polarizations) and in the infrared (8-14 μm) band [Paloscia and Pampaloni, 1992]. In this experiment, ground truth data of soil moisture, surface roughness, leaf area index, plant water content, and plant height have been collected simultaneously to remote sensing measurements. The microwave emissivity has been approximated by the ratio between the microwave and infrared brightness temperature.

Table 1 shows the measured ground truth. d is the height of alfalfa, LAI is the leaf area index which is the area of leaves per unit area, m_v is the plant water content in kg/m^3. From the measured moisture content of soil, the dielectric constant of soil at various growth stages are calculated from the soil dielectric model [Hallikaninen, et al., 1985]. The fractional volume of leaves are calculated from the LAI and height of the vegetation. These parameters are shown in Table 2. The leaf dielectric constant is calculated from the the gravimetric moisture content of 80% with a plant dielectric model [Ulaby and El-Rayes, 1987].

The theoretical model with continuous random medium approach is used to interpret the emission from alfalfa. The soil roughness is estimated to have rms height of $3.5mm$ and the correlation length of $1.0cm$. The Kirchhoff's approximation with Gaussian roughness statistics is used to calculate the scattering and emission. A optimization scheme is used to minimize the difference between theoretical simulation and experimental data from 10 to 50 degrees by varying the lateral and vertical correlation lengths of the random medium. Since at 36 GHz the measured emissivity did not change significantly during the growth stage, the correlation lengths have been derived from the data at 10 GHz. To avoid the non physical results with very large or small correlation length, the minimum and maximum values of the correlation lengths are assumed to be $0.2mm$ and $5.0mm$.

From the derived correlation lengths, it is found that the lateral correlation length did not vary much during growth cycle. The vertical correlation length decreases with plant water content as shown in Figure 5. The results obtained from the theoretical model are compared with experimental data from different dates are shown in Figure 6. The symbols H and V represent the measured horizontally and vertically polarized emissivity, respectively. The continuous curves are the simulation results. It shows the simulation agrees well with the experimental results.

5.4 THEORETICAL SIMULATION FOR NON AZIMUTHALLY SYMMETRICAL MEDIA

In this section, the emission from non azimuthally symmetrical media is investigated with the brightness temperatures calculated using the Kirchhoff's law. Since the emphasis of this study is on the effect of volume scattering, in the numerical study, the ground is assumed to be flat and the scatterers have some tilted angles. For the case where the terrain has slope and the vegetation grow straight, the configuration can be transformed to the case where the ground is flat and the vegetation is tilted toward certain angle. The emission from the new configuration can be solved using radiative transfer model and the brightness temperature can be obtained from the coordinate transformation.

The effect of fractional volume is shown in Figures 7. The size of scatterers used is the same as those in Section 3.2. The cylindrical scatterers in this case are tilted at 5°. From Figures 3 and 4, it is found that the third Stokes parameter is usually the largest near 45° azimuthal angles. Therefore in Figure 7, the azimuthal angle is fixed at 45°. The horizontal axis is for the elevation angle in degree. The vertical axis is brightness temperature. The physical temperature is 300 K. It is found that with only a small tilted angle, the third Stokes parameter would be as high as 30 K at high observation angle with the fractional volume of the scatterers being 0.1%. There is also a large fourth Stokes parameter V_B as shown in Figure 7 (b). Since U_B can be expressed as the difference between linearly polarized brightness temperatures, the variation of horizontally and vertically polarizated brightness temperatures indicates how large the U_B will be. The results are shown in Figures 8 (a) and (b).

Figures 9 (a) and (b) show the azimuthal angle variation of the brightness temperatures. The horizontal axis is the azimuthal angle in degree and the vertical axis is the brightness temperatures of U_B and V_B. It is found that the the third Stokes parameter increases with the observation angle because of at larger angles, the volume scattering effect is larger since the ground is flat and thus emits no U_B and

V_B. Figures 10 (a) and (b) show the effect of the tilted angle of scatterers for the brightness temperatures of U_B and V_B. The horizontal axis is the elevation angle in degree. The azimuthal angle is fixed at $45°$. Th vertical axes are the brightness temperature U_B and V_B. It is found that the third Stokes parameters brightness temperatures is very sensitive to the azimuthal asymmetry of the medium while the V_B is also sensitive to the symmetrical property at high incident angles.

5.5 CONCLUSION

In this study, a theoretical model for the polarimetric emission from non azimuthal symmetry medium is developed. For the calculation of the emissivity from the random medium, both the direct method with the fluctuation-dissipation theory and the calculation using Kirchhoff's law are compared. For the calculation of bistatic scattering coefficients and emission, the vector radiative transfer theory (RT) is applied. It is found that in general, the first-order iterative solution gives a good estimation of the polarimetric brightness temperature In addition, the model is used to simulate the emission from alfalfa crop for different growth stage. It is found that the vertical correlation length is inversely proportional to the plant water content. This theoretical model is used to investigate the sensitivity of the medium azimuthal asymmetry to the third and fourth Stokes parameters. It is found that in general, the third and fourth Stokes parameters are significantly different from zero with small preferred orientation angle of scatterers. The third Stokes parameter is found to be very sensitive to the azimuthal asymmetry property of the medium.

Date	d (m)	LAI	m_v (kg / m^3)
7-11	0.30	1.2	0.5
7-13	0.35	2.0	0.8
7-19	0.45	3.0	1.2
7-20 am	0.47	3.5	1.4
7-20 pm	0.50	4.0	1.6
7-21 am	0.51	3.2	1.3
7-21 pm	0.52	2.5	1.0
7-26	0.55	1.5	0.6

Table 1 Table of the ground truth for alfalfa

Date	soil dielectric constant	fractional volume (%)
7-11	(5.8,0.8)	0.6
7-13	(5.8,0.8)	0.85
7-19	(4.2,0.4)	1.0
7-20 am	(4.2,0.4)	1.2
7-20 pm	(4.2,0.4)	1.2
7-21 am	(4.2,0.4)	0.95
7-21 pm	(4.2,0.4)	0.95
7-26	(3.6,0.2)	0.41

Table 2 Table of the derived parameters for alfalfa

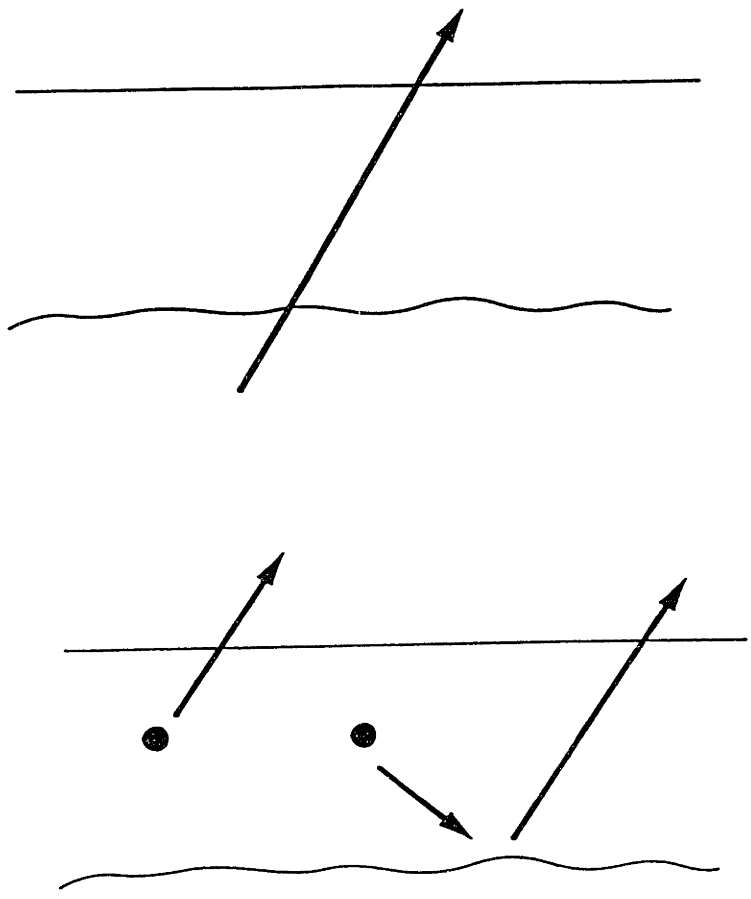

Figure 1 zero-th order mechanisms

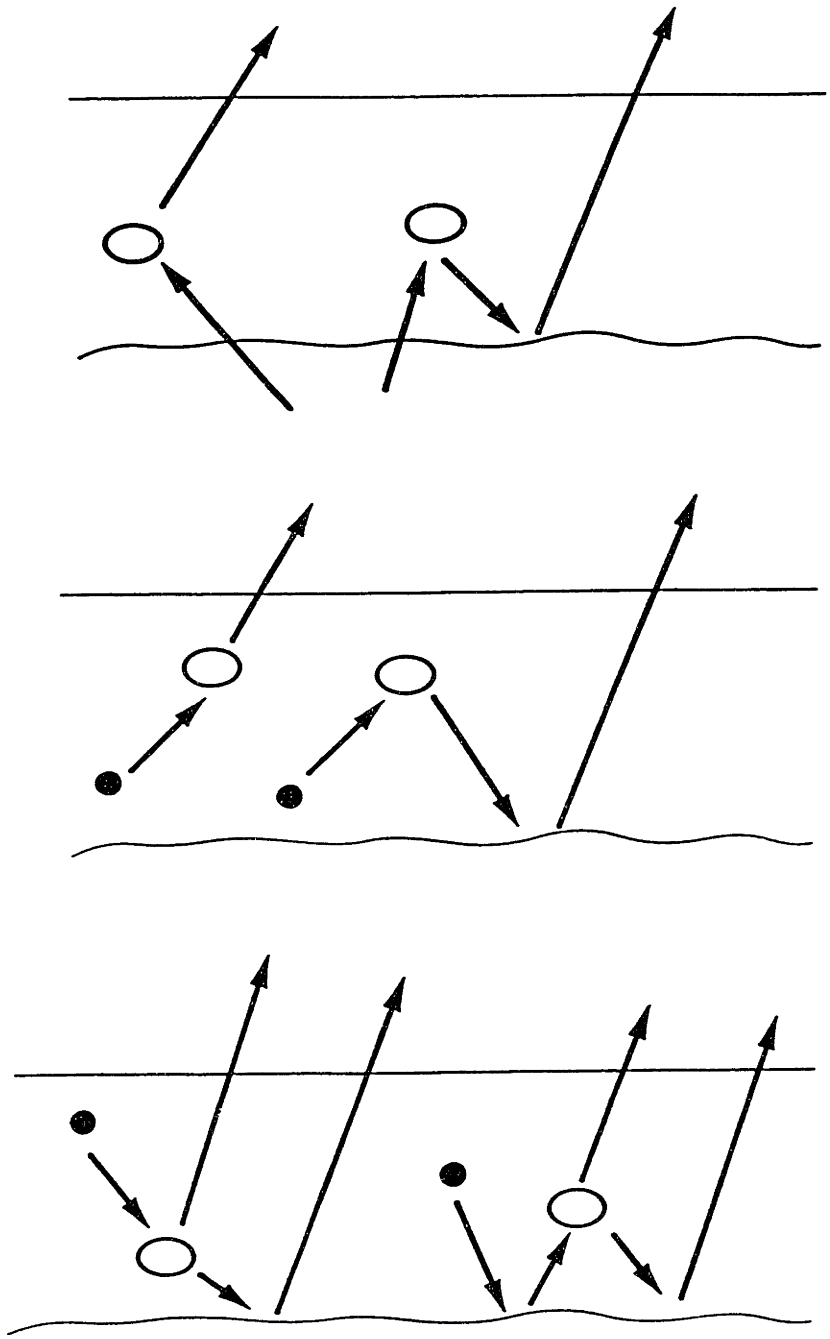

Figure 2 first order mechanisms

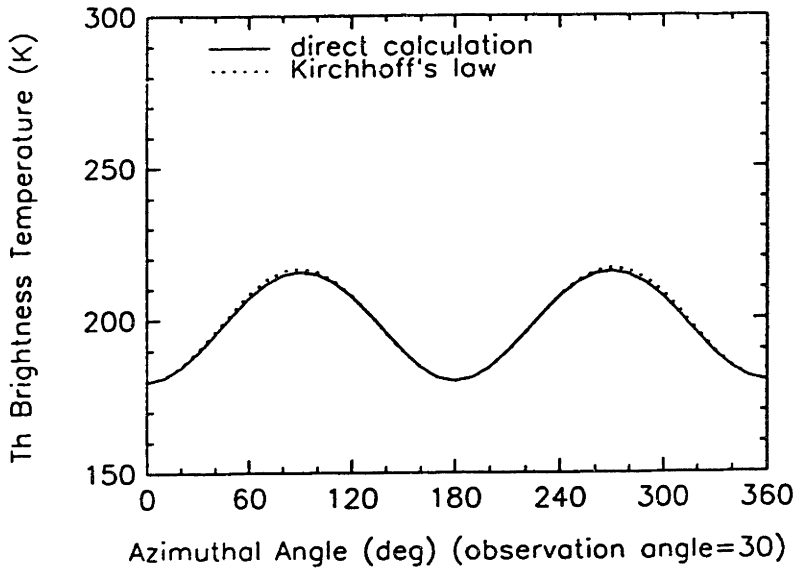

Figure 3 (a) Comparison of two formulation of Th for 0.02% fractional volume

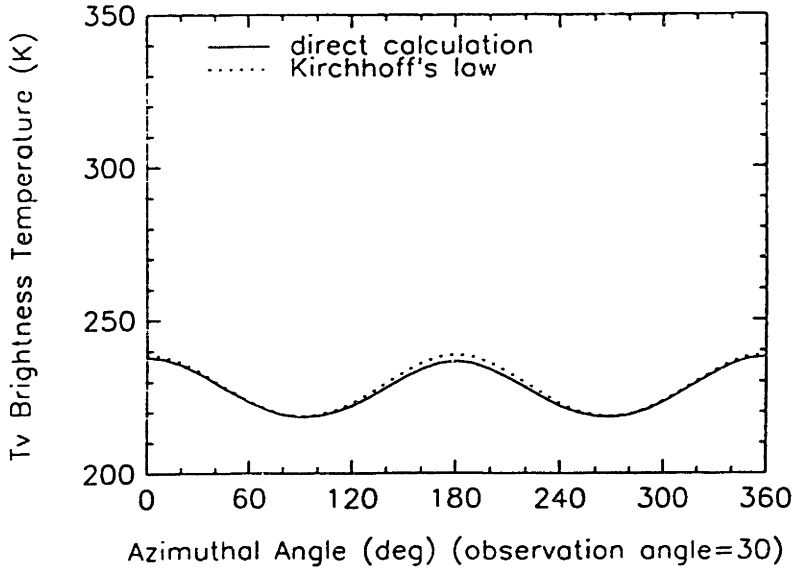

Figure 3 (b) Comparison of two formulation of Tv for 0.02% fractional volume

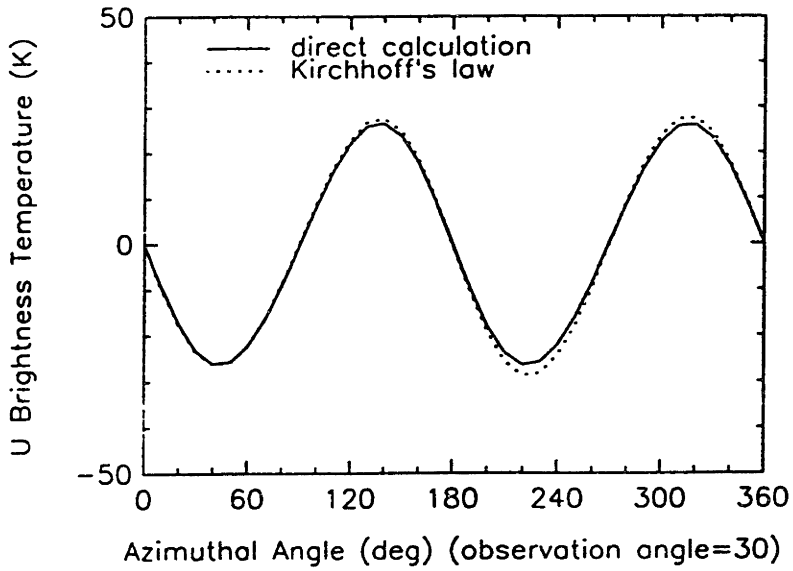

Figure 3 (c) Comparison of two formulation of U for 0.02 % fractional volume

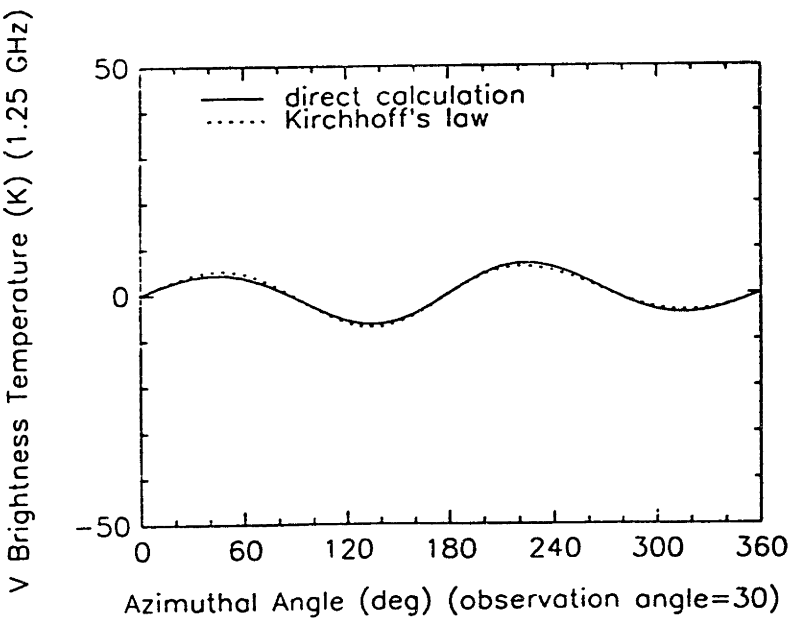

Figure 3 (d) Comparison of two formulation of V for 0.02 % fractional volume

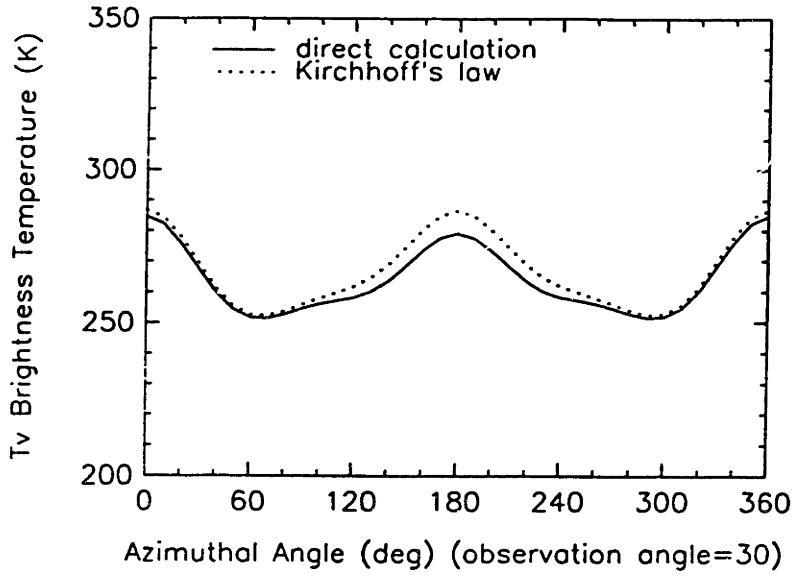

Figure 4 (a) Comparison of two formulation of Tv for 0.1% fractional volume

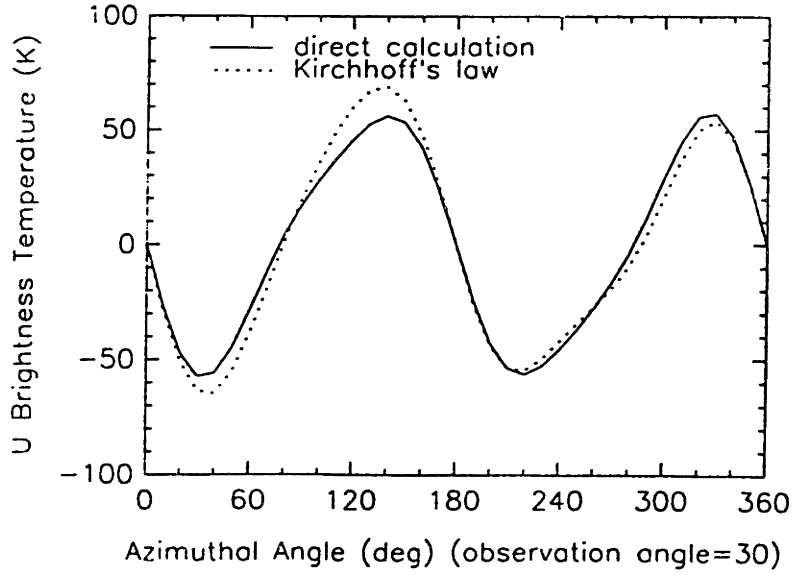

Figure 4 (b) Comparison of two formulation of U for 0.01% fractional volume

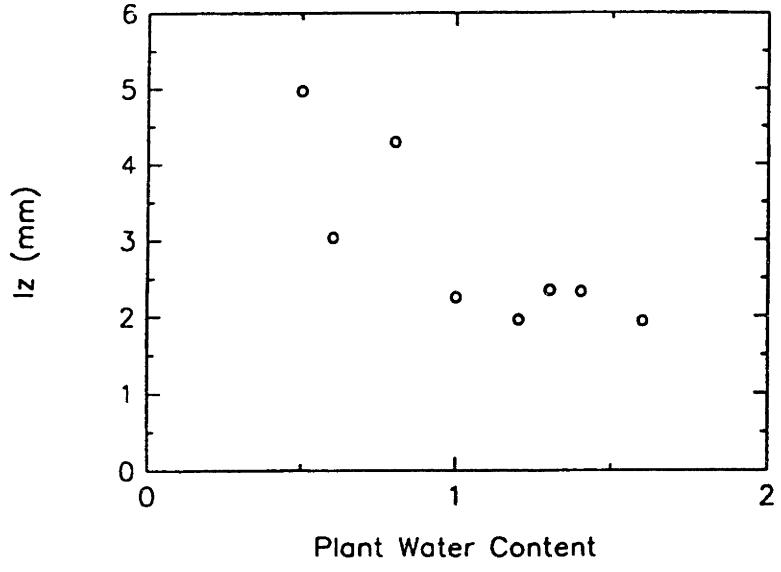

Figure 5 Variation of Correlation Length with Plant Water Content

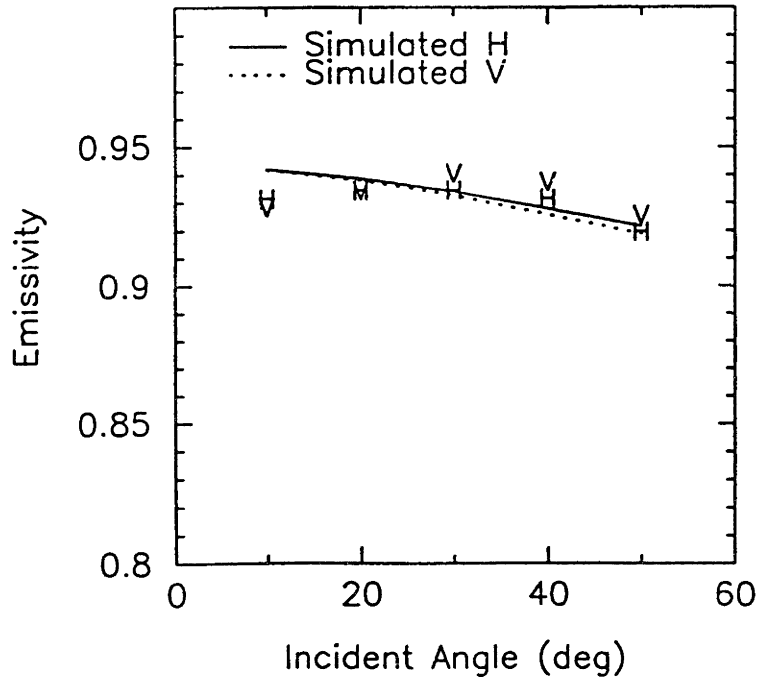

Figure 6 (a) Comparison of measured and simulated emissivity for Date 7-11

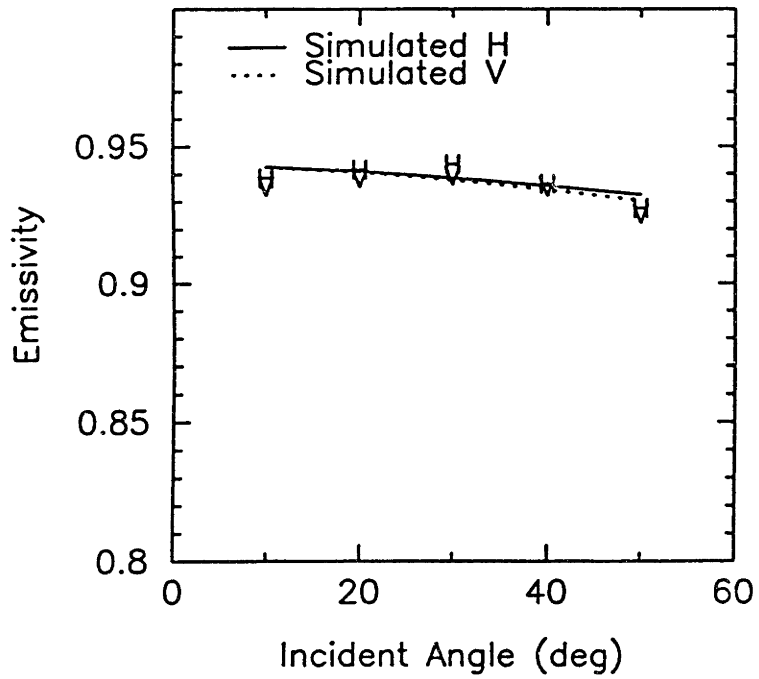

Figure 6 (b) Comparison of measured and simulated emissivity for Date 7-13

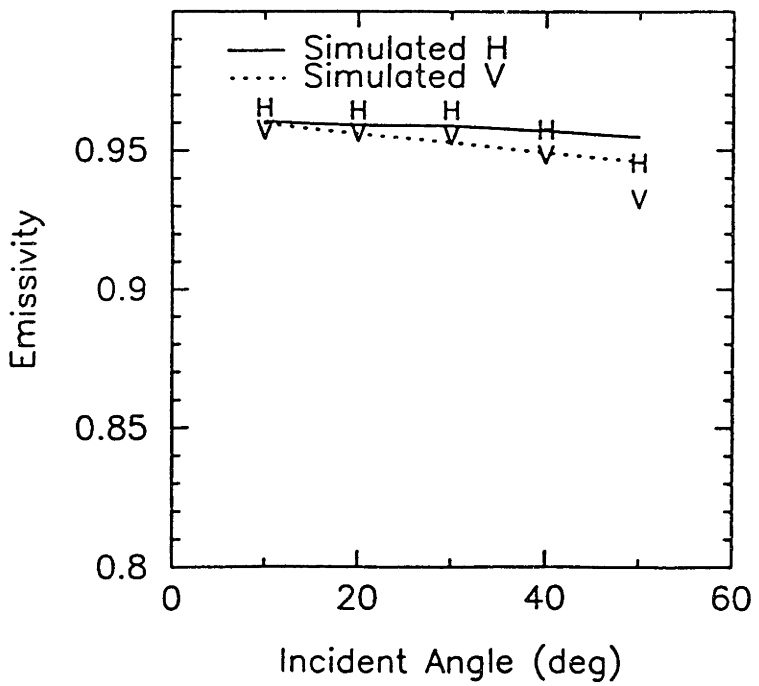

Figure 6 (c) Comparison of measured and simulated emissivity for Date 7-19

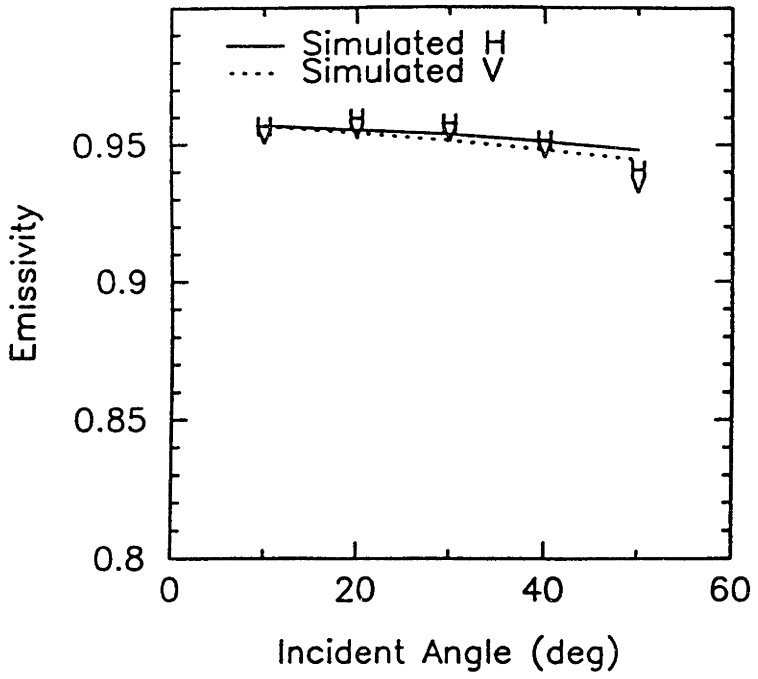

Figure 6 (d) Comparison of measured and simulated emissivity for Date 7-20 am

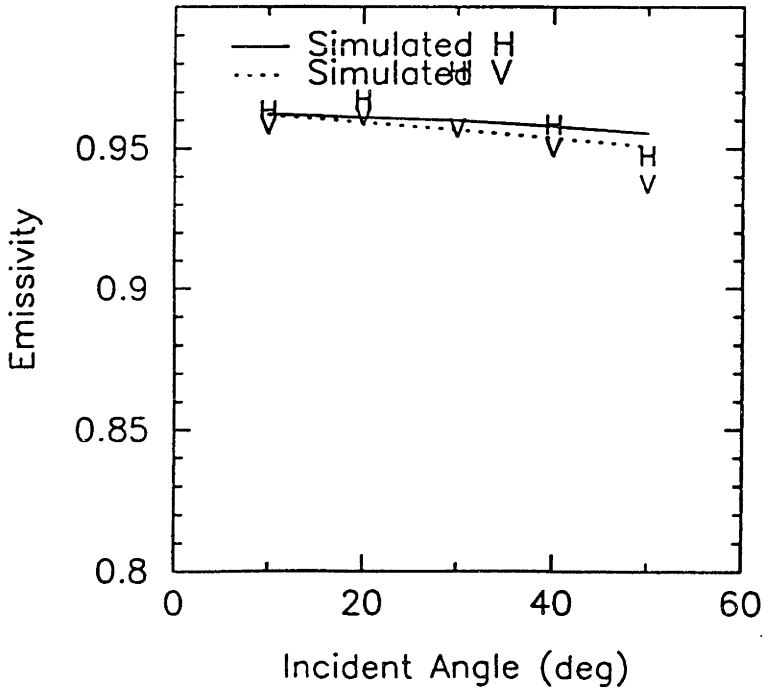

Figure 6 (e) Comparison of measured and simulated emissivity for Date 7-20 pm

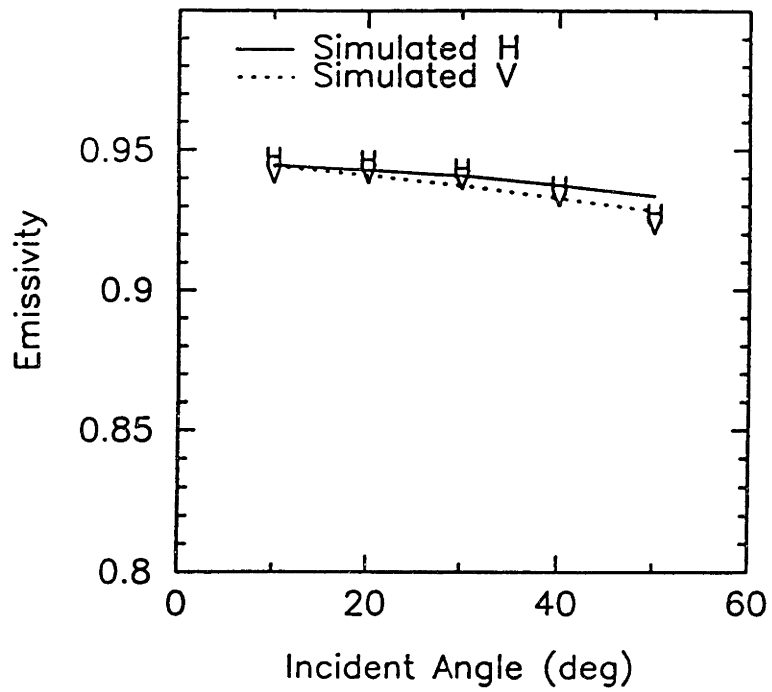

Figure 6 (f) Comparison of measured and simulated emissivity for Date 7-21 am

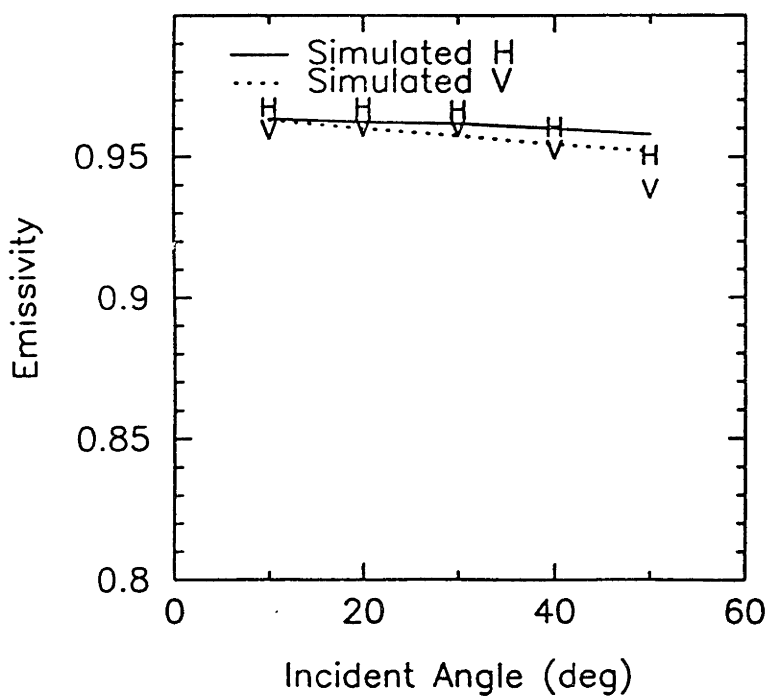

Figure 6 (g) Comparison of measured and simulated emissivity for Date 7-21 pm

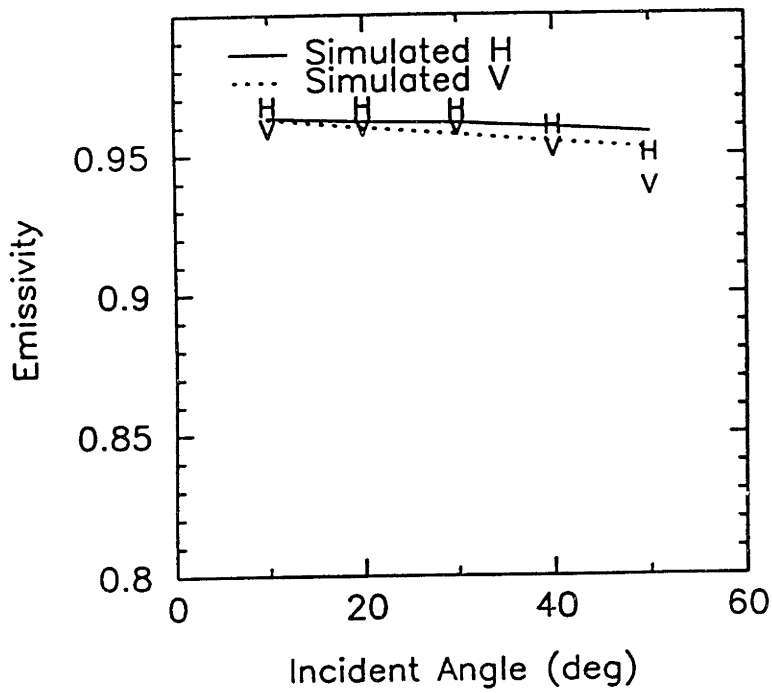

Figure 6 (h) Comparison of measured and simulated emissivity for Date 7-26

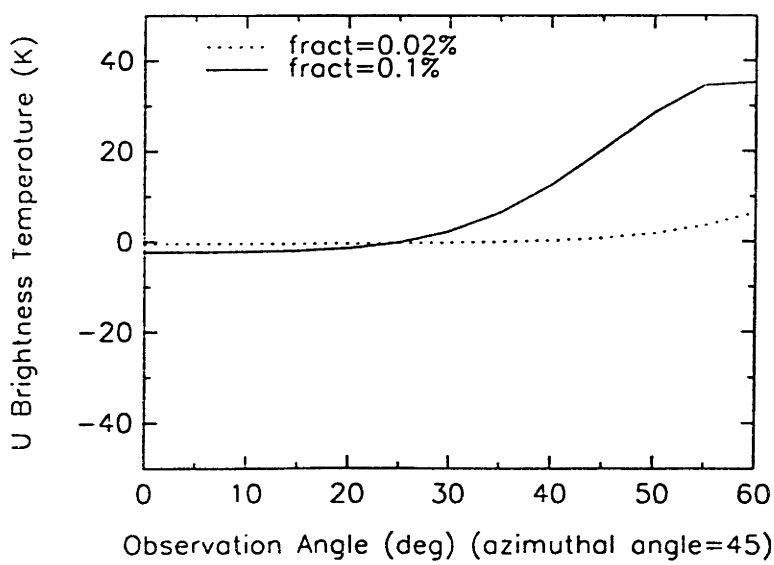

Figure 7 (a) Simulated brightness temperature U_B for a layer of 5° tilted cylinders

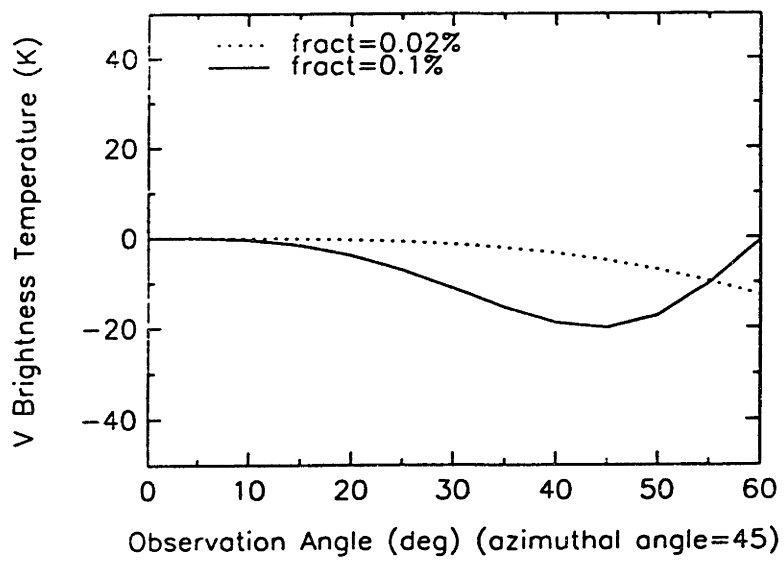

Figure 7 (b) Simulated brightness temperature V_B for a layer of 5° tilted cylinders

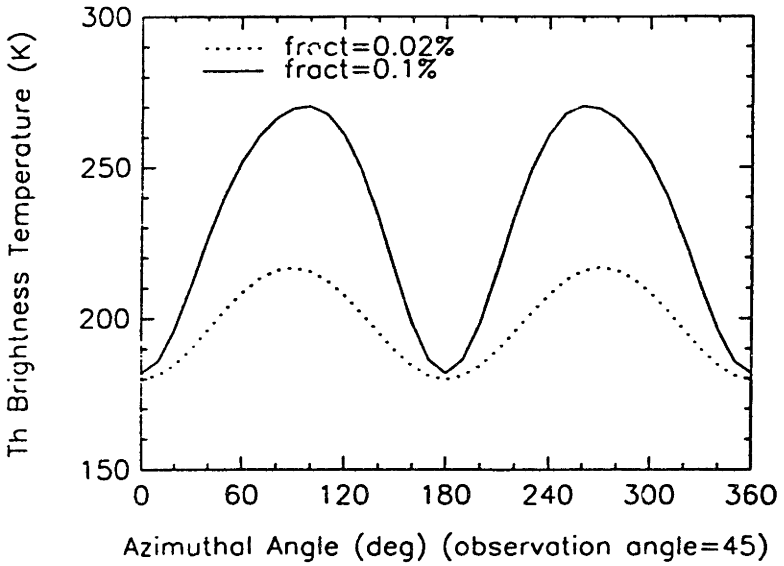

Figure 8 (a) Simulated brightness temperature T_h for a layer of 5° tilted cylinders

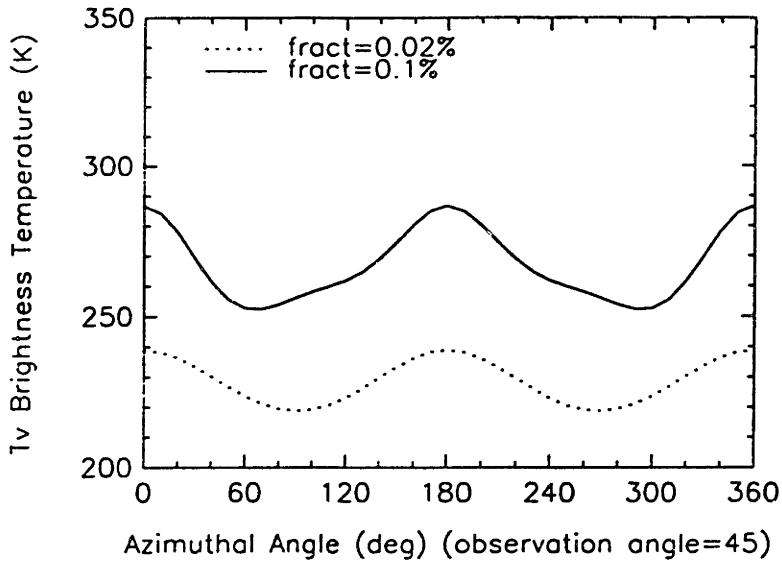

Figure 8 (b) Simulated brightness temperature T_v for a layer of 5° tilted cylinders

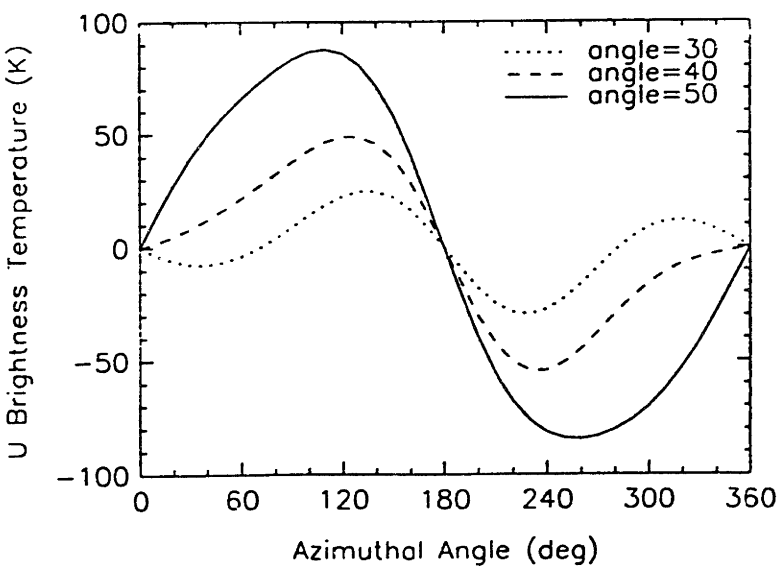

Figure 9 (a) Simulated brightness temperature U_B of 0.1 % cylindrical scatterers with 15° tilted angle

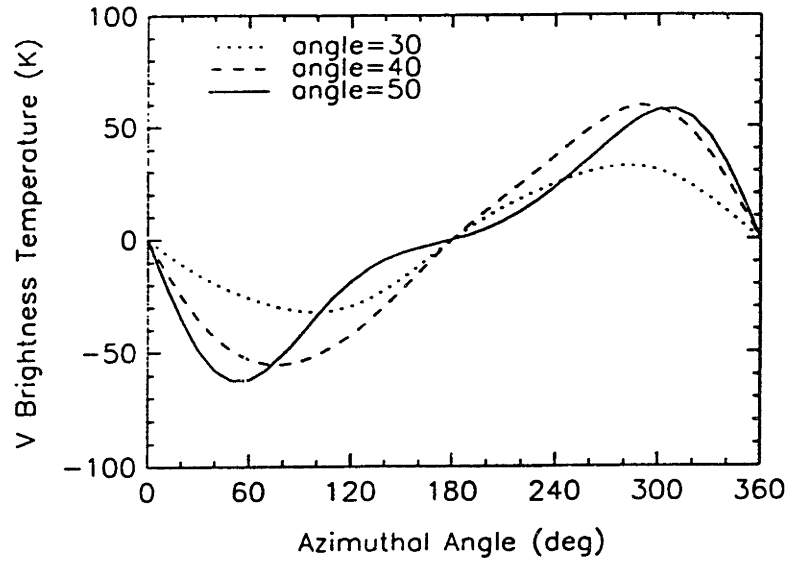

Figure 9 (b) Simulated brightness temperature V_B of 0.1 % cylindrical scatterers with 15° tilted angle

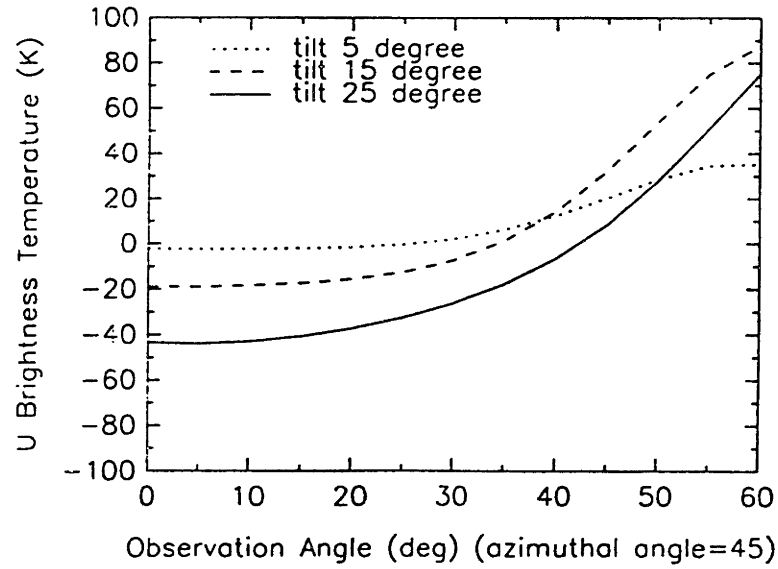

Figure 10 (a) Simulated brightness temperature U_B of 0.1 % cylindrical scatterers with different tilted angle

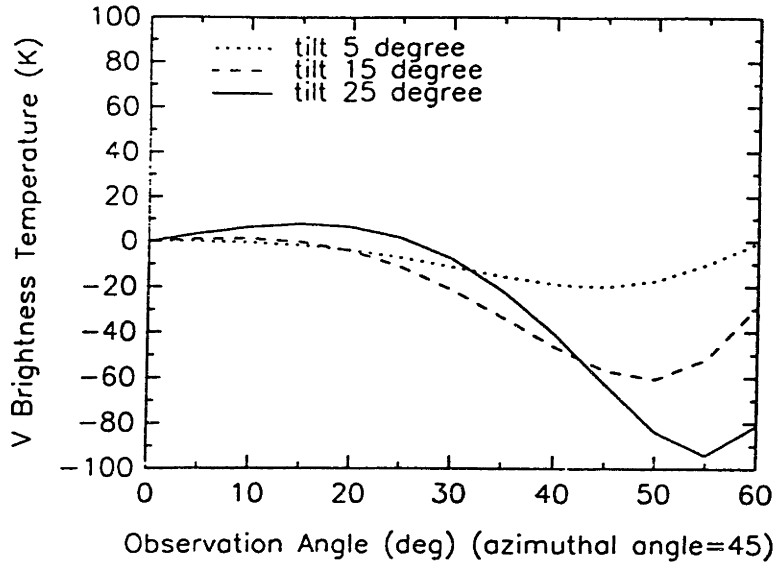

Figure 10 (b) Simulated brightness temperature V_B of 0.1 % cylindrical scatterers with different tilted angle

Chapter 6.

Conclusion

In this thesis, theoretical models are developed to calculate the scattering, attenuation, and emission of electromagnetic wave interaction with the earth terrain. These theoretical models has been applied to interpret the multi-frequencies, as well as polarimetric remote sensing data taken from space, aircrafts and ground experiments.

In Chapter 2, the radiative transfer (RT) theory for clustered vegetation structures is developed and used to interpret polarimetric radar backscattering measurement data from a pine forest. The RT theory has been widely used to calculate radar backscattering coefficients from layered geophysical media and to interpret the measurement data. However, the conventional RT theory ignores the relative phase information associated with structured scatterers, which may play an important role in the overall scattering behavior. To take into account the clustered structures with the radiative transfer theory, the scattering function of each cluster is calculated by incorporating the phase interference of scattered fields from each component. Therefore, the resulting phase matrix and extinction matrix are used in the radiative transfer equations to calculate the polarimetric backscattering coefficients from layered random media embedded with vegetation clusters. A multi-scale structure model of a pine forest, which includes the trunks, the primary and secondary branches, and the

needles is used to interpret and simulate polarimetric radar response at P-band (0.44 GHz), L-band (1.25 GHz), C-band (5.3 GHz), and X-band (9.6 GHz). The effect of the tree branches and the leaves structures on the scattering signature at multiple frequencies is investigated. It is found that the fine structure of leaves is important at higher frequencies such as C-band and X-band. On the other hand, it is necessary to consider the clustering effect at lower frequencies. This phenomenon is demonstrated with the comparison of theoretical simulation and SIR-C/XSAR data collected over the Landes pine forest.

To interpret the Milli-meter Wave (MMW) backscattering range profile, a theoretical model consisted of a random medium and deterministic objects is developed in Chapter 3. Tree is considered as a combination of a crown and trunks, from which the scattering power for each part is calculated separately. The trunks are modelled as circular cylinders with random rough surface and the Kirchhoff approximation is used to calculate the radar return power, with the attenuation caused by the crown properly taken into account. The crown is modeled as a collection of randomly oriented discrete scatterers. The backscattering coefficient of this random medium is calculated using the radiative transfer theory. The branches and the coniferous leaves are modeled as circular cylinders. The deciduous leaves are modelled as elliptical disks. The dimensions of these elements are determined by the measurements of physical samples. Finite cylinder approximation and physical optics approximation are used for the calculation of scattering from cylinders and disks, respectively. The theoretical simulations of range profile from coniferous and deciduous trees are consisted with the measurement using a 94 GHz FMCW radar. Variation of the measurement from the deciduous trees is interpreted as the results of the leaves density variation.

In Chapter 4, the attenuation and phase fluctuations of electromagnetic waves propagating through the foliage is investigated with the development of a radiative transfer model in conjunction with the statistical clutter model. The attenuation of the average received field is obtained from the sum of the absorption loss and the scattering loss. The amplitude fluctuation of electromagnetic wave is calculated from the bistatic scattering coefficients using the radiative transfer theory. The phase fluctuation is obtained from the amplitude fluctuation assuming the phase of the fluctuation field is uniformly distributed between $-\pi$ and π. The average received power is obtained from the sum of the power of the average field and the power of the fluctuation field. The attenuation is then obtained by comparing the radiated power from a source under the foliage to the received power from a source in free space. Theoretical results are compared with experimental data collected by the MIT Lincoln Laboratory during the 1990 Foliage Penetration Experiment. The theoretical model is used to illustrate the frequency, polarization and angular dependencies of the attenuation and phase fluctuations. It is found that the vertical polarized attenuation is higher than the attenuation for the horizontal polarization at P-band because of the contribution from the trunk. The polarization dependence at L- and C-bands is found to be small. The increase of attenuation with frequency and incident angle and the contribution of different scatterers is investigated using the developed theoretical model. It is found from both the theoretical simulation and measurement analysis, the phase fluctuation increases with the attenuation. With this proposed model, it is also possible to examine the attenuation and phase fluctuation for different tree moisture contents, tree types and forest densities.

In chapter 5, the polarimetric emission from the volume scattering is studied. A vegetation medium is modeled as a layer of random medium with either continuous

permittivity fluctuation or random distributed discrete scatterers on top of a flat or rough ground. For the calculation of the emissivity from the random medium, both the direct method with the fluctuation-dissipation theory and the calculation using Kirchhoff's law are compared. For the calculation of bi-static scattering coefficients and emission, the vector radiative transfer theory (RT) is applied. It is found that in general, the first-order iterative solution gives a good estimation of the polarimetric brightness temperature. In addition, experimental data collected over the alfalfa field at various growth stage at 10 GHz are used to validate the theoretical model. The theoretical model is used to investigate the polarimetric emission from the non azimuthal symmetrical medium. It is found that the third and fourth Stokes parameters would be significant for a medium with small azimuthal asymmetry.

Appendix A. Scattering by a Circular Cylinder

For a circular dielectric cylinder with length longer than the wavelength of incident electromagnetic wave and radius much smaller than the wavelength of interest, the finite cylinder approximation[Karam et al., 1988; Yueh, 1991] is a fairly good approach.

The finite cylinder approximation assumes that the internal field inside a finite length cylinder is the same as that inside an infinitely long cylinder upon an incident wave. Subsequently, scattered fields are obtained by evaluating the fields radiated from this approximate induced current sources. The scattered field in the far field limit is expressed in the following form,

$$\begin{pmatrix} E_{hs} \\ E_{vs} \end{pmatrix} = \frac{e^{ikr}}{r} \begin{pmatrix} f_{hh} & f_{hv} \\ f_{vh} & f_{vv} \end{pmatrix} \cdot \begin{pmatrix} E_{hi} \\ E_{vi} \end{pmatrix} \tag{1}$$

where E_{hi} and E_{vi} are the horizontally and vertically polarized components of the incident electric field, respectively, and similarly for the scattered field components, E_{hs} and E_{vs}.

The scattering matrix elements of a finite cylinder with dielectric constant ϵ, free space permeability, radius a and length l are given by

$$
\begin{aligned}
f_{hh} &= \frac{k_0^2(\epsilon-1)U}{2}(-Z_0^+\eta B_{0h} + 2\sum_{n=1}^{\infty}(Z_n^- i\cos\theta_i A_{nh} - Z_n^+\eta B_{nh})\cos[n(\phi_s-\phi_i)]) \\
f_{vv} &= \frac{k_0^2(\epsilon-1)U}{2}((Z_0^+\cos\theta_i\cos\theta_s + Z_0\sin\theta_s)A_{nh} \\
&\quad + 2\sum_{n=1}^{\infty}[(Z_n^+\cos\theta_i A_{nh} + iZ_n^-\eta B_{nh})\cos\theta_s + A_{nh}Z_n\sin\theta_s]\cos[n(\phi_s-\phi_i)]) \\
f_{hv} &= \frac{k_0^2(\epsilon-1)U}{2}2i\sum_{n=1}^{\infty}(Z_n^- i\cos\theta_i A_{nv} - Z_n^+\eta B_{nv})\sin[n(\phi_s-\phi_i)] \\
f_{vh} &= \frac{k_0^2(\epsilon-1)U}{2}2i\sum_{n=1}^{\infty}[(Z_n^+\cos\theta_i A_{nv} + iZ_n^-\eta B_{nv})\cos\theta_s + A_{nh}Z_n\sin\theta_s]\sin[n(\phi_s-\phi_i)]
\end{aligned}
\tag{2}
$$

where

$$
U = \frac{\exp[i(k_{zi}-k_{zs})l]-1}{i(k_{zi}-k_{zs})}
$$

and

$$
\begin{aligned}
Z_n &= \frac{a}{k_{1\rho i}^2 - k_{\rho s}^2}[k_{1\rho i}J_n(k_{\rho s}a)J_{n+1}(k_{1\rho i}a) - k_{\rho s}J_n(k_{1\rho i}a)J_{n+1}(k_{\rho s}a)] \\
Z_n^+ &= \frac{k_0}{2k_{1\rho i}}(Z_{n+1}+Z_{n-1}) \\
Z_n^- &= \frac{k_0}{2k_{1\rho i}}(Z_{n-1}-Z_{n+1})
\end{aligned}
\tag{3}
$$

The coefficients A_{nh}, A_{nv}, B_{nh} and B_{nv} are given by

$$
\begin{aligned}
A_{nh} &= \frac{\Delta_{ah}}{\Delta} \\
A_{nv} &= \frac{\Delta_{av}}{\Delta} \\
\eta B_{nh} &= \frac{\Delta_{bh}}{\Delta} \\
\eta B_{nv} &= \frac{\Delta_{bv}}{\Delta}
\end{aligned}
\tag{4}
$$

where

$$
\begin{aligned}
\Delta &= (\frac{k_{zi}}{k_0})^2(\frac{1}{y^2}-\frac{1}{x^2})^2 n^2 - [\frac{\epsilon J_n'(x)}{xJ_n(x)} - \frac{H_n^{(1)'}(y)}{yH_n^{(1)}(y)}][\frac{J_n'(x)}{xJ_n(x)} - \frac{H_n^{(1)'}(y)}{yH_n^{(1)}(y)}] \\
\Delta_{ah} &= 2(\frac{k_{\rho i}}{k_0})\frac{1}{\pi y^2 J_n(x)H_n^{(1)}(y)}\frac{k_{zi}}{k_0}(\frac{1}{y^2}-\frac{1}{x^2})n \\
\Delta_{bh} &= 2(\frac{k_{\rho i}}{k_0})\frac{1}{\pi y^2 J_n(x)H_n^{(1)}(y)}(-i)[\epsilon\frac{J_n'(x)}{xJ_n(x)} - \frac{H_n^{(1)'}(y)}{yH_n^{(1)}(y)}] \\
\Delta_{av} &= 2(\frac{k_{\rho i}}{k_0})\frac{1}{\pi y^2 J_n(x)H_n^{(1)}(y)}i[\frac{J_n'(x)}{xJ_n(x)} - \frac{H_n^{(1)'}(y)}{yH_n^{(1)}(y)}] \\
\Delta_{bv} &= \Delta_{ah}
\end{aligned}
\tag{5}
$$

In the above equations, x and y are defined as

$$
\begin{aligned}
x &= k_{1\rho i}a \\
y &= k_{\rho i}a
\end{aligned}
$$

where

$$
\begin{aligned}
k_{1\rho i} &= \sqrt{k_0^2\epsilon - k_{zi}^2} \\
k_{\rho i} &= \sqrt{k_0^2 - k_{zi}^2}
\end{aligned}
$$

Appendix B. Scattering by a Circular Disk

For a thin circular disk with dielectric constant ϵ and free space permeability, the physical optics approximation can be used to calculate the scattered field. The scattering matrix is derived and given in this appendix using $\exp(-iwt)$ convention.

The physical optics approximation assumes that the internal field inside a disk is the same as that inside an infinitely extended dielectric layer upon an incident wave. Subsequently, scattered fields are obtained by evaluating the fields radiated from this approximate induced current sources.

The scattering matrix elements are given as

$$
\begin{aligned}
f_{hh}(\theta_s,\phi_s,\theta_i,\phi_i) =& \frac{k_0^2}{4\pi}(\epsilon-1)\cos(\phi_s-\phi_i)(A_{1h}U_a+B_{1h}U_b) \\
f_{hv}(\theta_s,\phi_s,\theta_i,\phi_i) =& \frac{k_0^2}{4\pi}(\epsilon-1)\frac{k_0}{k_1}\frac{k_{1zi}}{k_1}\sin(\phi_s-\phi_i)(-A_{1v}U_a+B_{1v}U_b) \\
f_{vh}(\theta_s,\phi_s,\theta_i,\phi_i) =& \frac{k_0^2}{4\pi}(\epsilon-1)\cos\theta_s\sin(\phi_s-\phi_i)(A_{1h}U_a+B_{1h}U_b) \\
f_{vv}(\theta_s,\phi_s,\theta_i,\phi_i) =& \frac{k_0^2}{4\pi}(\epsilon-1)\frac{k_0}{k_1}[\frac{k_{1zi}}{k_1}\cos\theta_s\cos(\phi_s-\phi_i)(A_{1v}U_a-B_{1v}U_b) \\
&+\frac{k_0}{k_1}\sin\theta_s\sin\theta_i(A_{1v}U_a+B_{1v}U_b)]
\end{aligned}
\tag{1}
$$

where A_{1h} and B_{1h} are the amplitudes of upgoing and downgoing horizontally polarized incident waves in the disk and, similarly, A_{1v} and B_{1v} are for vertically polarized incident waves.

Let

$$
\begin{aligned}
A_1 =& \frac{2\exp(-ik_{zi}d/2)\exp(ik_{1zi}d/2)(\rho_{01}-1)}{(1+\rho_{01})^2\exp(-ik_{1zi}d)-(1-\rho_{01})^2\exp(ik_{1zi}d)} \\
B_1 =& \frac{2\exp(-ik_{zi}d/2)\exp(-ik_{1zi}d/2)(\rho_{01}+1)}{(1+\rho_{01})^2\exp(-ik_{1zi}d)-(1-\rho_{01})^2\exp(ik_{1zi}d)}
\end{aligned} \tag{2}
$$

where

$$
k_{1zi} = \sqrt{k_0^2\epsilon\mu - k_{xi}^2 - k_{yi}^2}
$$

Using $\rho_{01} = k_{1zi}/\mu k_{zi}$ to evaluating A_1 and B_1 gives A_{1h} and B_{1h}, respectively. Likewise, A_{1v} and B_{1v} are obtained by substituting $\rho_{01} = k_{1zi}/\epsilon k_{zi}$ into A_1 and B_1.

The other quantities appearing in the scattering matrix are defined as follows:

$$
\begin{aligned}
U_a =& \frac{\exp[(i(k_{1zi}-k_{zs})d/2] - \exp[-i(k_{1zi}-k_{zs})d/2]}{i(k_{1zi}-k_{zs})}V \\
U_b =& \frac{\exp[(i(k_{1zi}+k_{zs})d/2] - \exp[-i(k_{1zi}+k_{zs})d/2]}{i(k_{1zi}+k_{zs})}V
\end{aligned} \tag{3}
$$

Here V is given by the following integral

$$
V = \int_S d^2\overline{\rho}\exp[i(\overline{k}_{\rho i} - \overline{k}_{\rho s})\cdot\overline{\rho}]
$$

where

$$
\begin{aligned}
\overline{k}_{\rho i} =& \hat{x}k_{xi} + \hat{y}k_{yi} \\
\overline{k}_{\rho s} =& \hat{x}k_{xs} + \hat{y}k_{ys}
\end{aligned}
$$

For a circular disk, the integral for V can be carried out and is given as

$$
V = \pi a^2 \frac{2J_1(|\overline{k}_{\rho i} - \overline{k}_{\rho s}|a)}{|\overline{k}_{\rho i} - \overline{k}_{\rho s}|a}
$$

Appendix C. Kirchhoff's Approximation

In the Kirchhoff's Approximation, the field at a given point of the surface is assumed to be the same as the field for the tangent plane at that point [Kong, 1990]. In this appendix, the surface height and the surface correlation function are assumed to be Gaussian distributed. The surface has rms height σ and correlation length l. It is consisted of an coherent reflection term and an incoherent scattering term and is expressed as

$$\overline{\overline{R}}(\theta,\phi;\theta',\phi') = \overline{\overline{R}}_0(\theta)\delta(\cos\theta - \cos\theta')\delta(\phi-\phi') + \overline{\overline{R}}_f \tag{1}$$

The coherent reflection is expressed as

$$\overline{\overline{R}}_0(\theta) = \overline{\overline{R}}_{00}(\theta)\cdot e^{-4k^2\sigma^2\cos^2\theta} \tag{2}$$

where k is the free space wavenumber. $\overline{\overline{R}}_{00}$ is the reflection from the flat surface and is expressed as

$$\overline{\overline{R}}_{00}(\theta) = \begin{pmatrix} |R_h(\theta)|^2 & 0 & 0 & 0 \\ 0 & |R_v(\theta)|^2 & 0 & 0 \\ 0 & 0 & Re(R_v(\theta)R_h^*(\theta)) & -Im(R_v(\theta)R_h^*(\theta)) \\ 0 & 0 & Im(R_v(\theta)R_h^*(\theta)) & Re(R_v(\theta)R_h^*(\theta)) \end{pmatrix} \tag{3}$$

where $R_h(\theta)$ and $R_v(\theta)$ are the Fresnel reflection coefficients for horizontally and vertically polarized waves, respectively.

The incoherent reflection is expressed as

$$\overline{\overline{R}}_f(\theta,\phi;\theta',\phi') = D_I\cdot\overline{\overline{C}}(\theta,\phi;\theta',\phi')\cdot S(\theta,\phi;\theta',\phi') \tag{4}$$

D_I is expressed in terms of summation as

$$D_I = \sum_{m=1}^{\inf}\frac{(k_{tdz}^2\sigma^2)^m}{m!m}l^2 e^{-(k_{tdx}^2+k_{tdy}^2)l^2/4m}e^{-\sigma^2k_{tdz}^2} \tag{5}$$

where $\overline{k}_{td} = \overline{k}_i - \overline{k}_t = \hat{x}k_{tdx} + \hat{y}k_{tdy} + \hat{z}k_{tdz}$

The matrix $\overline{\overline{C}}$ is given in terms of scattering functions from the surface as

$$\overline{\overline{C}}(\theta,\phi,\theta',\phi') = \begin{pmatrix} <|f_{hh}|^2> & <|f_{hv}|^2> & Re<f_{hv}f_{hh}^*> & -Im<f_{hv}f_{hh}^*> \\ <|f_{vh}|^2> & <|f_{vv}|^2> & Re<f_{vv}f_{vh}^*> & -Im<f_{vv}f_{vh}^*> \\ 2Re<f_{vh}f_{hh}^*> & 2Re<f_{vv}f_{hv}^*> & Re<f_{vv}f_{hh}^*+f_{vh}f_{hv}^*> & -Im<f_{vv}f_{hh}^*-f_{vh}f_{hv}^*> \\ 2Im<f_{vh}f_{hh}^*> & 2Im<f_{vv}f_{hv}^*> & Im<f_{vv}f_{hh}^*+f_{vh}f_{hv}^*> & Re<f_{vv}f_{hh}^*-f_{vh}f_{hv}^*> \end{pmatrix} \tag{6}$$

where

$$\begin{aligned} f_{hh} &= -(\hat{v}\cdot\hat{k}')(\hat{v}'\cdot\hat{k})R_h - (\hat{h}\cdot\hat{k}')(\hat{h}'\cdot\hat{k})R_v \\ f_{vv} &= -(\hat{h}\cdot\hat{k}')(\hat{h}'\cdot\hat{k})R_h - (\hat{v}\cdot\hat{k}')(\hat{v}'\cdot\hat{k})R_v \\ f_{hv} &= (\hat{h}\cdot\hat{k}')(\hat{v}'\cdot\hat{k})R_h - (\hat{v}\cdot\hat{k}')(\hat{h}'\cdot\hat{k})R_v \\ f_{vh} &= (\hat{v}\cdot\hat{k}')(\hat{h}'\cdot\hat{k})R_h - (\hat{h}\cdot\hat{k}')(\hat{v}'\cdot\hat{k})R_v \end{aligned} \tag{7}$$

and the R_h, R_v are the Fresnel reflection coefficients evaluated at the stationary phase points for the horizontal and vertical polarizations, respectively. The angular bracket denotes ensemble average.

The shadowing effects are taken into account by introducing the shadowing function S derived by [Smith, 1967; Sancer, 1969] as

$$S(\theta,\phi,;\theta',\phi') = \begin{cases} 1/(1+\Lambda(\mu)), & for\ \phi = \phi' + \pi, \theta \geq \theta' \\ 1/(1+\Lambda(\mu')), & for\ \phi = \phi' + \pi, \theta' \geq \theta \\ 1/(1+\Lambda(\mu)+\Lambda(\mu')), & \text{otherwise} \end{cases} \tag{8}$$

with $\mu = \cot\theta$, $\mu' = \cot\theta'$, and

$$\Lambda(\mu) = \frac{1}{2}[\sqrt{\frac{2}{\pi}}\frac{s}{\mu}\exp^{-\mu^2/2s^2} - erfc(\frac{\mu}{\sqrt{2}s})] \tag{9}$$

where $erfc$ is the complementary error function.

References

[1] Ayasli, S., T. A. Dickens, and J. G. Fleischman, "Foliage penetration experiment with three-frequency synthetic aperture radar", *Progress In Electromagnetics Research Symposium,* Cambridge, MA, July 1-5, 1991.

[2] Beaudoin, A., T. Le Toan, S. Goze, E. Nezry, A. Lopes, E. Mougin, C.C. Hsu. H.C Han, J.A. Kong and R.T. Shin, "Retrieval of forest biomass from SAR data", Int. J. of Remote Sensing, vol. 15, no. 13, 1994.

[3] Borgeaud, M., R. T. Shin, and J. A. Kong," Theoretical models for polarimetric radar clutter," *J. Electromagnetic Waves and Applications*, Vol. 1, No 1, 67-86, 1987.

[4] Borgeaud, M., S. V. Nghiem, R. T. Shin, and J. A. Kong, " Theoretical models for polarimetric microwave remote sensing of earth terrain," *J. Electromagnetic Waves and Applications*, Vol. 3, No. 1, 61-81, 1989.

[5] Borel, C. C. and R. E. McIntosh, "Millimeter wave backscatter from deciduous trees," *IEEE Trans. Antennas Propagat.*, Vol. AP-38, No. 9, pp. 1391–98, 1990.

[6] Cimino, J. B. "SIR-B – the second shuttle imaging radar experiment," *IEEE Trans. Geo. Remote Sensing*, GRS-24,pp. 445-452, July 1986.

[7] Chu, N. C., J. A. Kong, H. A. Yueh, S. V. Nghiem, J. G. Fleischman, S. Ayasli, and R. T. Shin, "Variance of phase fluctuations of waves in a random media," *J. Electromagnetic Waves Appl.*, Vol. 6, No. 2, 1992.

[8] Ding, K. H., L. M. Zurk, and L. Tsang, "Pair distribution functions and attenuation rates for sticky particles in dense media," *J. Electromagnetic Waves Appl.*, Vol. 8, No. 12, 1994.

[9] Durden, Stephen L., J. J. van Zyl, and H. A. Zebker, "Modeling and observation of the radar polarization signature of forested areas," *IEEE Trans. on Geosci. Remote Sensing*, Vol. GE-27, No. 3, pp. 290-301, May 1989.

[10] Elachi, C. Editor, " Special issue on the Shuttle Imaging Radar (SIR-B)," *IEEE Trans. Geosci. Remote Sensing*, Vol. GE-24, no. 4, 1986.

[11] Evans, D. L.,T. G. Farr, J. J. van Zyl, and H. A. Zebker," Radar polarimetry analysis tools and applications," *IEEE Trans. Geosci. Remote Sensing*, Vol. GE-26, 774-789, 1988.

[12] Fisher, A. D., "A model for microwave intensity propagation in an inhomogeneous medium," *IEEE Trans. Ant. Propag.*, Vol. AP-25, 876-882, 1977.

[13] Fleischman, J. G., M. F. Toups, and S. Ayasli,"Foliage attenuations and backscatter analysis of SAR imagery," *IEEE Trans. Aero. Electr. System*, Vol. 32, No. 1, pp 135-144, 1996.

[14] Foldy, L. L., "The multiple scattering of waves," *Phys. Rev.* 67, 107-119, 1945.

[15] Fung, A. K., and H. S. Fung, "Application of first order renormalization method to scattering from a vegetation-like half-space," *IEEE Trans. Geosci. Electron.*, Vol. GE-15, 189-195, 1977.

[16] Fung, A. K., and F. T. Ulaby, "A scatter model for leafy vegetation," *IEEE Trans. Geosci. Electron.*, Vol. GE-16, 281-285, 1978.

[17] Han, H. C., "Electromagnetic wave phenomena in inhomogeneous and anisotropic media," *Ph.D. Dissertation*, Dept. Electrical Engineering and Computer Science, Massachusetts Institute of Technology, June, 1992.

[18] Giberson, W. E. 'Gene', "Seasat-A : a retrospective," *Int. J. Remote Sensing,* Vol. 12, No. 8, pp. 1611-1612, 1991.

[19] Hallikainen M.T., F.T. Ulaby, M.C. Dobson, M.A. EL-Rayes and L.K. Wu, "Microwave dielectric behaviour of wet soil. Part I : Empirical models and experimental observations", IEEE Transactions on Geoscience and Remote Sensing, Vol. GE-23, no.1, 1985.

[20] Hsu, C.C., Y. E. Yang, R. T. Shin, J.A. Kong, C. Kohler, T. Nguyen, H, Nguyen, J. Ho, "Application of EMSARS background model to MMW vegetation scattering simulation," *Ground Target Modeling and Validation Conference Proceeding*, Houghton, Michigan, August, 1992.

[21] Hsu, C.C., J.A. Kong, M. F. Toups, J. G. Fleischman, S. Ayasli, R.T. Shin, "Electromagnetic modeling of foliage obscured point source response," *SPIE'93 Proceeding*, Orlando, Florida, May, 1993a.

[22] Hsu, C.C., Y. E. Yang, R. T. Shin, J.A. Kong, C. Kohler, T. Nguyen, H, Nguyen, "Discrete scatterer model for deciduous tree MMW vegetation scattering Simulation," *Ground Target Modeling and Validation Conference Proceeding*, Houghton, Michigan, August, 1993b.

[23] Hsu, C.C., H.C. Han, J.A. Kong, R.T. Shin, A. Beaudoin, and T. Le Toan, "Radiative t- asfer theory for polarimetric remote sensing of pine forest at P band," Int. J. of Remote Sensing, vol. 15, no. 14, 1994a.

[24] Hsu, C.C., J.A. Kong, R.T. Shin, T. Le Toan, S. Paloscia, P. Pampaloni, "Microwave emission and backscattering from crops," PIERS'94 Proceeding, Noordwijk, The Netherlands, July 11-15, 1994b.

[25] Jao, J. K., "Amplitude Distribution of Composite Terrain Radar Clutter and the K-distribution," *IEEE Trans. Antennas Propagat.*, Vol. 32, No. 10, pp. 1049-1062, 1984.

[26] Johnson, J. T., J. A. Kong, R. T. Shin, D. H. Staelin, K. O'Neill, and A. Lohanick, "Third Stokes parameter emission from a periodic water surfaces," *IEEE Trans. Geosci. Remote Sensing,* Vol. 31, No. 5, pp. 1066-1080 , 1993.

[27] Johnson, J. T., J. A. Kong, R. T. Shin, S. H. Yueh, S. V. Nghiem, and R. Kwok, "Polarimetric thermal emission from rough ocean surfaces," *J. Electromag. Waves and Applic.,* Vol. 8, No. 1, pp. 43-59 , 1994.

[28] Jordan, R. L. "The seasat-A synthetic aperture radar system," *IEEE J. Oceanic Eng.*, Vol. OE-5, No. 2, Apr, 1980.

[29] Jordan, R. L., B. L. Huneycutt, and M. Werner, "The SIR-C/X-SAR synthetic aperture radar system," *Proceeding IEEE*, Vol. 79, No. 6, 827-838, June 1991.

[30] Karam, Mostafa A., A. K. Fung, and Yahia M. M. Antar, "Electromagnetic wave scattering from some vegetation samples," *IEEE Trans. Geosci. Remote Sensing*, Vol. GE-26, N0. 6, 799-808, Nov. 1988.

[31] Karam, M. A. and A. K. Fung,"Leaf-shape effects in electromagnetic wave scattering from vegetation," *IEEE Trans. Geosci. Remote Sensing*, Vol. 27, No. 6, 1989.

[32] Kong, J. A., Electromagnetic Wave Theory, John Wiley, New York, 1990.

[33] Kong, J. A., Ed., Polarimetric Remote Sensing, Progress In Electromagnetics Research (PIER), Vol. 3, Elsevier, New York, 1990.

[34] Lang, R. H.,"Electromagnetic backscattering from a sparse distribution of lossy dielectric scatterers" *Radio Science*, Vol. 16, No. 1, 15-30, 1981.

[35] Lang, R. H. and H. A. Saleh, "Microwave inversion of leaf area and inclination angle distribution from backscattered data," *IEEE Trans. Geosci. Remote Sensing*, Vol. GE-23, No. 5, p. 685-694, September 1985.

[36] Lang, R. H. and J. S. Sidhu,"Electromagnetic backscattering from a layer of vegetation: a discrete approach," *IEEE Trans. Geosci. Remote Sensing,* Vol. GE-21, No. 1, 1983.

[37] Lax, M., "Multiple scattering of waves," *Rev. Mod. Phys.* 23, 287-310, 1951.

[38] Le Toan, T., A. Beaudoin, J. Riom, and D. Guyon, "Relating forest biomass to SAR data," *IEEE Trans. Geosci. Remote Sensing*, Vol. GE-30, No. 2, 1992.

[39] Le Vein, D. M., A. Schneider, R. H. Lang, and H. G. Carter, "Scattering from thin dielectric disks," *IEEE Trans. Ant. Prop.*, Vol. Ap-33, No. 12, 1420-1413, Dec. 1985.

[40] Le Vein, D. M., A. J. Griffis, C. T. Swift, and T. J. Jackson "ESTAR: A synthetic aperture microwave radiometer for remote sensing applications," *Proceedings IEEE*, Vol. 82, No. 12, 1787-1800, 1994.

[41] Lim, H. H., A. A. Swartz, H. A. Yueh, J. A. Kong, R. T. Shin, and J. J. van Zyl, "Classification of earth terrain using polarimetric synthetic aperture radar images," *J. Geophys. Res.*, Vol. 94, No. B6, 7049-7057, 1989.

[42] McDonald, K. C., M. C. Dobson, and F. T. Ulaby, "Using MIMICS to model L-band multiangle and multitemporal backscatter from a walnut orchard," *IEEE Trans. Geosci. Remote Sensing*, Vol. GE-28, No. 4, 1990.

[43] Massachusetts Institute of Technology/Lincoln Laboratory, *Foliage Penetration Experiment*, Ground Truth Data Collection Report, MTR-90-017/SEC124-46M, 1990.

[44] National Aeronautics and Space Administration *From Pattern to Process : The Strategy of the Earth Observing System*, NASA EOS Science Steering Committee Reprot, Volume II, 1986.

[45] Nemoto, Y., H. Nishino, M. Ono, H. Mizutamari, K. Nishikawa, and K. Tanaka, "Japanese earth resources satellite-1 synthetic aperture radar," *Proceeding IEEE*, Vol. 79, No. 6, 800-809, June 1991.

[46] Nghiem, S. V., M. E. Veysoglu, J. A. Kong, R. T. Shin, K. O'Neill and A. W. Lohanick, "Polarimetric passive remote sensing of a periodic soil surfaces : microwave measurements and analysis," *J. Electromag. Waves and Applic.*, Vol. 5, No. 9, pp. 997-1005, 1991.

[47] Paloscia, S. and P. Pampaloni, "Microwave vegetation indexes for detecting biomass and water conditions of agricultural crops," *Remote Sensing of Environment*, no. 40, 15-26, 1992.

[48] Raney, R. K., A. P¿ Luscombe, E. J. Langham, and S. Ahmed, "RADARSAT," *Proceeding IEEE*, Vol. 79, No. 6, 839-849, June 1991.

[49] Sancer, M. I., "Shadow-corrected electromagnetic scattering from a randomly rough surface," *IEEE Trans. Ant. Propagat.*, Vol. AP-17, 577-585, 1969.

[50] Schwering, F. K., E. J. Violette, and R. H. Espeland, "Millimeter-wave propagation in vegetation: Experiments and theory," *IEEE Trans. Geos. Remote Sensing*, Vol. 26, no. 3, 355-367, 1988.

[51] Shin, R. T., and J. A. Kong, "Radiative transfer theory for active remote sensing of two-layer random medium," Progress in Electromagnetics Research (PIER), J. A. Kong, Ed., Vol. 1, Chapter 4, Elsevier, New York, 1989.

[52] Smith, B. G., "Geometrical shadowing of a random rough surface," *IEEE Trans. Ant. Prop.*, Vol. AP-15, 668-671, 1967.

[53] Stofan, E. R., D. L. Evans, C. Schmullius, B. Holt, J. J. Plaut, J. van Zyl, S. D. Wall, and J. Way, "Overview of results of Spaceborne Imaging Radar-C, X-Band Synthetic Aperture Radar (SIR-C/X-SAR)," *IEEE Trans. Geo. Remote Sensing,* vol. 33, no. 4, 817-828, 1995.

[54] Stogryn, A., "Electromagnetic scattering by random dielectric constant fluctuations in a bounded medium," *Radio Science,* Vol. 9, 509-518, 1974.

[55] Toups, M. F., "An analysis of foliage induced azimuthal synthetic pattern distortions," *SPIE Synthetic Aperture Radar* Vol. 1630, 1992.

[56] Tsang, L. and J. A. Kong, "Wave theory for remote sensing of a half-space random medium with three-dimensional variations," *Radio Science*, Vol. 14, No. 3, 359-369, 1979.

[57] Tsang, L. and J. A. Kong, "Scattering of electromagnetic waves from random media with strong permittivity fluctuations," *Radio Science*, Vol. 16, No. 3, 303-320, 1981.

[58] Tsang, L. and J. A. Kong, "Effective propagation constants for coherent electromagnetic wave propagation in media embedded with dielectric scatters," *J. Appl. Phys.*, Vol. 53, No. 11, 1982.

[59] Tsang, L. and J. A. Kong, "Scattering of electromagnetic waves from a half space of densely distributed dielectric scatterers," *Radio Science*, Vol. 18, 1260-1272, 1983.

[60] Tsang, L., J. A. Kong, and R. T. Shin, "Radiative transfer theory for active remote sensing of a layer of nonspherical particles," *Radio Science*, Vol. 19, 629-642, 1984.

[61] Tsang, L., J. A. Kong, and R. T. Shin, Theory of Microwave Remote Sensing, Wiley-Interscience, New York, 1985.

[62] Tsang, L., "Polarimetric passive microwave remote sensing of random discrete scatterers and rough surface," *J. Electromagnetic Waves and Applications*, Vol. 5, No. 1, 1990.

[63] Tsang, L., and J. A. Kong, "Polarimetric signature of a canopy of dielectric cylinders," *J. Electromagnetic Waves and Applications*, Vol. 6, No. 1, 1992.

[64] Ulaby, F. T., M. A. El-Rayes, "Microwave dielectric spectrum of vegetation – part II: dual - dispersion model," *IEEE Trans. Geosci. Remote Sensing*, Vol. GE-25, No. 5, 550–557, 1987.

[65] Van De Hulst, H. C., Light Scattering by Small Particles, Dover, New York, 1981.

[66] van Zyl, J. J., H. A. Zebker, and C. Elachi, "Imaging radar polarization signature: theory and observation," *Radio Science*, Vol. 22, No. 4, 529-543, 1987.

[67] Veysoglu, M. E., H. A. Yueh, R. T. Shin and J. A. Kong, "Polarimetric passive remote sensing of periodic surfaces," *J. Electromagnetic Waves and Applications,* Vol. 5, No. 3, 267-280, 1990.

[68] Wertheim, M. S., "Exact solution of the Percus-Yervick integral equation for hard sphere," *Phys. Rev. Lett.*, Vol. 20, 321-323, 1963.

[69] Yueh, S. H., J. A. Kong, J. K. Jao, R. T. Shin, and T. Le Toan, "Branching model for vegetation," *IEEE Trans. Geosci. Remote Sensing*, Vol. 30, No. 2, 390-402, March 1992.

[70] Yueh, S. H., J. A. Kong, J. K. Jao, R. T. Shin, and T. Le Toan, "K-Distribution and multi-frequency polarimetric terrain radar Clutter," *J. Electro. Waves Applic.* , Vol. 5, No. 1, pp 1-15, 1991.

[71] Yueh, S. H., "Electromagnetic and statistical models for polarimetric remote sensing of vegetation," *Ph.D. Dissertation*, Dept. Electrical Engineering and Computer Science, Massachusetts Institute of Technology, February, 1991.

[72] Yueh, S. H., R. Kwok, F. K. Li, S. V. Nghiem, W. J. Wilson, and J. A. Kong, "Polarimetric passive remote sensing of ocean wind vectors," *Radio Science,* Vol. 29, No. 4, pp. 799-814, 1994.

[73] Yueh, S. H., W. J. Wilson, F. K. Li, S. V. Nghiem and W. B. Ricketts, "Polarimetric measurement of sea brighness temperatures using an aircraft K-band radiometer," *IEEE Trans. Geosci. Remote Sensing,* Vol. 33, No. 1, pp. 85-92, 1995.

[74] Yueh, S. H., J. A. Kong and R. T. Shin, "Scattering from randomly oriented scatterers with strong permittivity fluctuations," *J. Electromagnetic Waves and Applications*, Vol. 4, No. 10, 983-1004, 1990.

[75] Zebker, H. A., J. J. van Zyl and D. N. Held, "Imaging radar polarimetry from wave synthesis," *J. Geophys. Res.*, Vol. 92, No. B1, 683-701, 1987.

[76] Zuniga, M. A., and J. A. Kong, "Active remote sensing of random media," *J. Appl. Phys.*, Vol. 51, 74-79, 1980.

THESIS PROCESSING SLIP

FIXED FIELD ill _____ name _____

index _____ biblio _____

▶ COPIES (Archives) Aero Dewey (Eng) Hum

Lindgren Music Rotch Science

TITLE VARIES ▶☑ see degree book

NAME VARIES ▶☐ _____

IMPRINT (COPYRIGHT) _____

▶ COLLATION: 191 p

▶ ADD. DEGREE: _____ ▶ DEPT.: _____

SUPERVISORS: _____

NOTES.

cat'r: date:

page: J144

▶ DEPT E.E.

▶ YEAR: 1996 ▶ DEGREE: Ph.D.

▶ NAME: HSU, Chih-Chien